# Advanced Constitutive Models for Offshore Applications on Suction Pile Foundation

Kan Liao

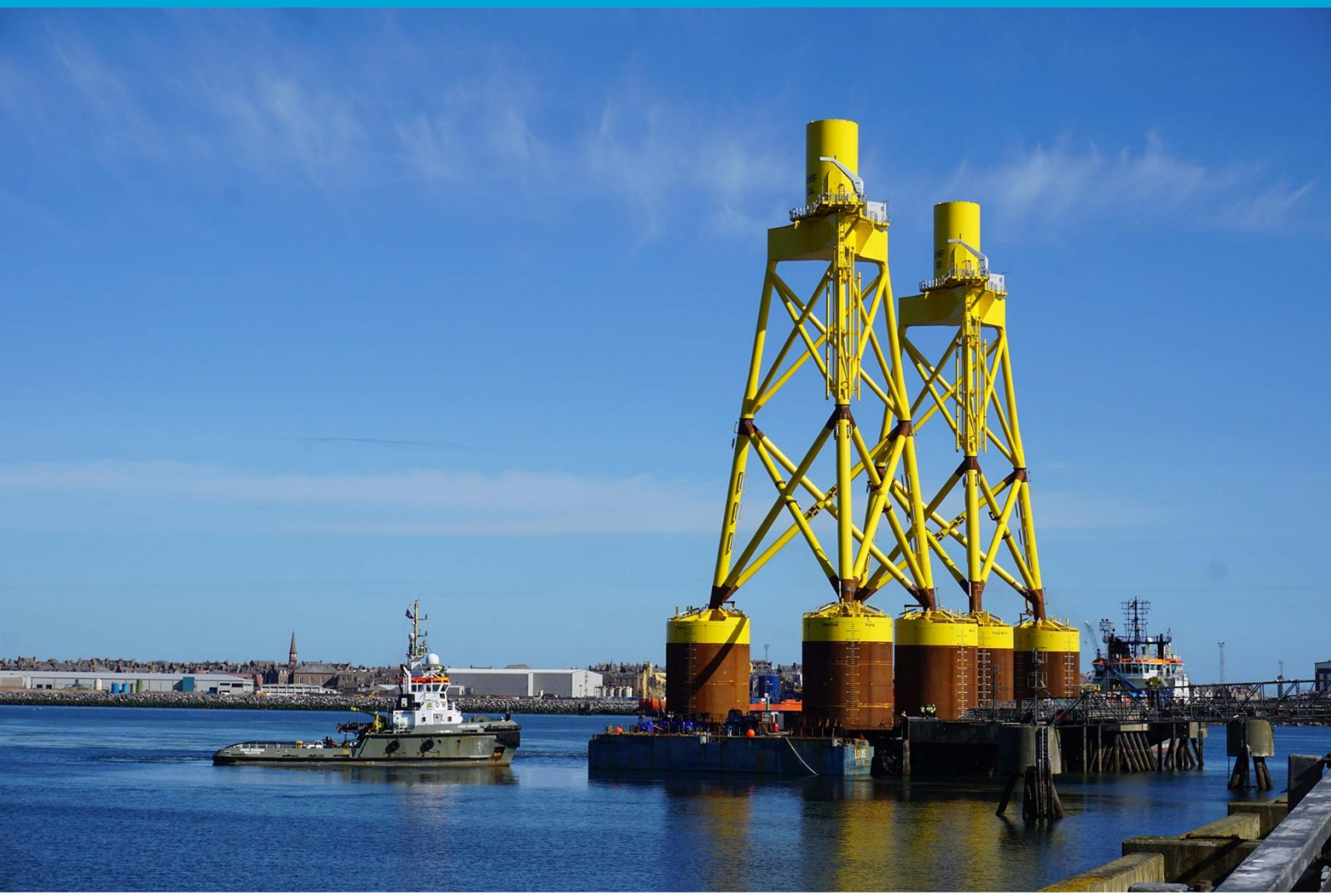

TU Delft

SPT Offshore

# Advanced Constitutive Models for Offshore Applications on Suction Pile Foundation

By

Kan Liao

in a partial fulfilment of the requirements for the degree of

**Master of Science**

in Offshore and Dredging Engineering at the Delft University of Technology,

to be defended publicly on 30th of November 2020.

| | | |
|---|---|---|
| Student number: | 4836995 | |
| Project duration: | December 15,2019 – November 30,2020 | |
| Thesis committee: | Pro. Dr. Ir. A. V. Metrikine | TU Delft – Chairman |
| | Dr. F. Pisanò | TU Delft – daily supervisor |
| | Dr. A. Tsouvalas | TU Delft |
| | Dr. A. Askarinejad | TU Delft |
| | Ir. O.J. Dijkstra | SPT Offshore |
| | Ir. J. Rebollo | SPT Offshore |

An electronic version of this thesis is available at http://repository.tudelft.nl/.

TU Delft

SPT Offshore

# Preface

As part of the Master Programme in Offshore Engineering at the Delft University of Technology, this project marks the ending of the study in The Netherlands. The basis of this thesis stemmed from my interest in offshore geotechnics, which is an essential part of offshore applications. After the achievement of this project, I learn a lot about suction pile technology, soil mechanics and finite element method. This master thesis work was carried out in collaboration with SPT Offshore in The Worden.

I would like to thank the following persons for their great help during the preparation of this master thesis. First, I would like to express my gratitude to my committee members. I would like to thank Federico Pisanò, who is my daily supervisor, for the inspiration of geotechnical engineering as well as his support during this project. Thanks to Juan Rebollo, Thijs Visser, and Oene Jeljer Dijkstra from SPT Offshore. All of your guidance was invaluable to this work. Thank you for our weekly discussions, where your feedback and critical view helped me not to get lost in the details and stick on the plan. Thanks to Apostolos Tsouvalas and Amin Askarinejad for your shape mind and great points during our thesis discussions that inspired me a lot. Thanks Andrei Metrikine for great guiding in structural dynamics.

In addition to the committee members, thanks are given to Weiyuan Zhang and Vlad Vacareanu from SPT Offshore, and Zheng Li that contributed to this thesis by teaching me the fundamental knowledge about geotechnics and finite element method. In addition to the committee members, thanks are given to Weiyuan Zhang

It was a special period for all of us in 2020 due to the COVID-19 that everyone was working from home. Therefore, I would like to thank all my friends who accompany and encourage me. They are Haoran SHI, Yuanxi ZHAO, Wei KONG, Weiwei LIU and Zihan YAN. Finally, I want to thank my family for their financial support and unconditional care during these past months.

*Kan Liao*
*November 2020*

# Abstract

The suction pile foundation is a large steel cylinder with an open end and sealed top. This foundation type is widely used in the oil&gas industry and wind energy. Experimental investigation and numerical investigation are the main two methods to understand the performance of the suction bucket foundation. The experimental studies are important and basal for design, but it is time-consuming and costly compared to numerical studies. However, the accuracy of the finite element method(FEM) in geotechnical problems highly depends on whether the soil constitutive models can correctly predict soil behaviour.

In our study, we investigate four constitutive models: the Mohr-Coulomb model, the hardening soil model, the NGI-ADP model, and the hypoplastic model. To some extent, advanced soil models can better present soil behaviour than traditional ones. However, it needs more laboratory test data to calibrate the advanced model parameters. The Mohr-Coulomb(MC) model is the most common soil model, which is an isotropic model include few parameters. The hardening soil model exceeds MC model by introducing the stress-dependent stiffness and distinguishing between loading and reloading. The NGI-ADP model is mainly used for undrained analysis, and it is an anisotropic model which can exact match with undrained shear strength and stiffness for various failure surfaces. The hypoplastic model has no distinguishing between elastic and plastic strain. It is an inelastic(dissipative) and incrementally nonlinear soil model without the requirement of a yield surface.

A soil investigation report of Block 17 offshore Angola is used to calibrate the aforementioned constitutive models. The cone penetration test(CPT), ball penetration test(BPT) and a series of laboratory tests(i.e. direct simple shear, triaxial, and oedometric tests) are exacted from the soil report and interpreted for calibration. Parameter determination procedures for constitutive models are explained. Subsequently, the consistency of the parameter set is validated by numerical simulation of direct shear and triaxial tests.

The numerical experiments for a suction pile foundation whose out diameter equals four and aspect ratio equals three are carried out. Four loading cases(i.e. horizontal, vertical tension, vertical compression and vertical-horizontal-moment(VHM) combining loadings) are included in the finite element analysis. The suction pile performance(i.e. deformation and capacity) are compared among the using of different constitutive models. Additionally, the compliance matrices of the suction pile for different soil models are obtained for the structural engineer.

The analyses indicated that NGI-ADP model could be the best choice for undrained analysis of suction pile foundation. This model has a robust calibration process, and well simulate the anisotropic strain-stress relationship. Additionally, the finite element results are conservative when modelling by NGI-ADP model. However, this model can not predict the right pore pressure build-up and stress-path, which may be improved by using a well-calibrated hypoplastic model.

# Contents

# List of Figures

# List of Tables

# 1 Introduction

## 1.1. Overview

Suction caissons also referred to as suction anchors, suction piles, or suction buckets, are an offshore foundation type developed in the 1990s for offshore oil and gas applications (Andersen et al., 2015). The suction pile foundation(SPF) is a large steel cylinder with an open end and sealed top. After an initial installation under its own weight, a negative(suction) pressure inside the caisson is created, and the resultant pressure differential push the caisson into the seabed to target depth. Once installed, the value is fixed to maintain passive suctions generated during operational loading conditions. In service, any upward movement of the caisson will generate suction pressure (passive suction) inducing inside the caisson by reverse end-bearing resistance acting on the soil plug. This suction increases the holding capacity of suction caissons remarkably compared with the case where the top lid is vented (Aubeny et al., 2003).

The suction pile is a relatively new form of offshore foundation with a number of advantages compared to conventional offshore foundations. They can be integrated with the jacket/TP(Transition Piece) substructure and installed in a single operation, potentially reducing offshore time and the number of offshore lifts. Since the pile-driving equipment is not used, the cost of the installation spread is reduced. The installations for the suction pile are almost silent, thus the disturbance for the marine life is decreased. Comparing with Gravity Base Structures(GBS), the weight and seabed footprint area of suction pile foundations is usually much less, which increasing the flexibility of installation vessels and deducing the demand of seabed preparation. Additionally, the suction pile can be easily removed from the seabed by reversing the installation process at the end of its service.

Recently, the suction pile foundation is more and more accepted in many applications. (e.g., Mono bucket, mooring anchor and jacket foundations, etc.) The main difference of suction foundations for different applications is the ratio of skirt length L and diameter D (L/D ratio), Table 1.1 and Figure 1.1 illustrate the typical values for different applications. The wall thickness to diameter ratio is generally varying from 0.3% to 0.6%(Budiaman et al., 2015). The suction pile foundations often design to bear long-term loads. Vertical force, horizontal force and bending moment can be transferred to the bucket foundation under the upper structure, which is defined as the combined loading mode (Yin et al., 2020).

Table 1.1: Suction Foundation and their L/D ratios (Tjelta, 2015)

| Application | Typical diameter(m) | Examples |
|---|---|---|
| Moorings:L/D<5 | 4-6 | Suction anchors/suction piles |
| Subsea structures:1<L/D<4 | 5-10 | Suction pile/"suction foundation"<br>- Mono-bucket<br>– Suction caisson<br>– Bucket foundation<br>–Skirt compartments<br>–Skirt foundation<br>(self-weight penetration) |
| Jackets: Typical L/D<1 | 8-15 | Bucket foundation<br>-Skirted foundations |
| Gravity Base Structures: L/D<<1 to 1 | 25-35 | Skirt/skirt-piles |
| Monopod tower | 15-20 | Bucket foundation<br>-Mono bucket |

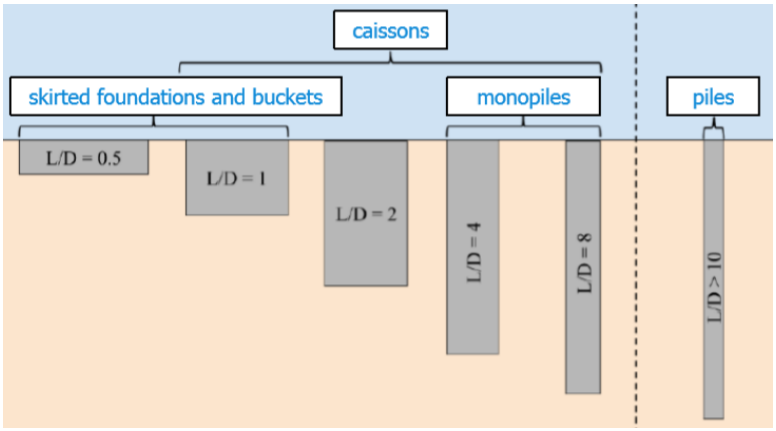


Figure 1.1: Foundation with different L/D ratios (Tjelta, 2015)

In the design process for a suction pile, it is important to understand the performance of the suction pile foundation. In the previous studies, numbers of experimental investigations have focused on the suction pile response under general monotonic/cyclic combined loads (Kim et al., 2014; Barari and Ibsen, 2012, 2011). Comparing with experimental studies, numerical studies are great time savings and economies. There are many studies about a suction pile foundation in clay using finite element models (Gerolymos et al., 2015; Kourkoulis et al., 2014; Muduli et al., 2013; Samui et al., 2011), Various constitutive models are used to research the response of suction pile foundations under combined loads. The accuracy of the numerical analysis depends to a large extent on if the nonlinear response of soil is correctly simulated.

The mechanical behaviour of soils can be modelled at various degrees of accuracy. For example, the linear elastic perfectly plastic model(Mohr-Coulomb) might be considered a first-order approximation of soil behaviour as it follows Hooke's law of linear and isotropic elasticity, which was thought of as the simplest available stress-strain relationship. However, more advanced materials models involving specific features(i.e., stress-dependency of stiffness, strain hardening/softening, critical state, anisotropic) were developed in finite element software(i.e., PLAXIS and ANSYS). Using the advanced models can simulate the behaviour of soils more realistically, therefore obtaining more accurate results from the finite element model calculations(Brinkgreve R.B.J., 2018).

Since the Mohr-Coulomb model was the simplest, it is widely used in the numerical studies of suction pile foundations (Zhang et al., 2019; Zorzi et al., 2019; Jia et al., 2018; Barari and Ibsen, 2012,

2011; Kay and Palix, 2011; Zdravkovic et al., 2001). Thus, this model is used in this study considered as a reference model for the advanced models. The first advanced model is the hardening soil model, which has the same strength parameters as the Mohr-Coulomb model but excessed the MC model by including the stress dependency of soil stiffness and distinguishing between loading and reloading. Another advanced model is the NGI-ADP model, which is an anisotropic model and suitable for undrained analysis. The last advanced model is the hypoplastic(HP) model, which is first proposed by von Wolffersdorff (1996) and developed by Mašín (2019). All the mentioned constitutive models are detailed introduced in section 2.3.

## 1.2. Research objective

The study is carried out by using finite element analysis, and the commercial software PLAXIS 3D is introduced. The rest of the methods are considered reference values, regardless of whether semi-empirical methods are not used in industry practice and are not recommended in important suction anchor applications. The suction foundations are applied to solving various engineering problems (Table1.1). Suction anchors, mono-bucket, and bucket foundation for jackets are relatively common and discussed in this thesis. For this type of foundation, the vertical, horizontal, and moment(VHM) loads and resistance are coupled. For the three applications above, the foundations are designed for different loading combinations. To simplify the FEM analysis, only the loading combinations instead of the whole structure-foundation-soil systems are considered. The main objective of the present study is to investigate the difference between constitutive models, namely Mohr-Coulomb, hardening soil, NGI-ADP, and hypoplastic model, in the suction pile applications. The soil parameters are calibrated base on a soil report, and a suction pile foundation is analyzed using PLAXIS 3D. The following sub-objectives are considered:

- **Comparing the required data and calibration process among different constitutive models.** There are numbers of parameters in constitutive models, and the calibration of different parameters needs different data and processes. A real soil report is included in this thesis; the constitutive models are calibrated to model the soil. The calibration process is detailed discussed for different models.
- **To analyze the soil element behaviour of different constitutive models.** After the calibration, the numerical experiments are carried out for the models and compared with the same real laboratory tests. The distinction is indicated and related to the calibration process.
- **To compare the suction pile performance when using different constitutive models.** Four different finite element models are built using different constitutive models to analyze the same suction pile behaviour. The deformation, capacity, and compliance matrix of the suction pile are discussed. The results obtained from different finite element models are compared and explained.

## 1.3. Thesis overview

This research consisted of roughly three parts: literature review, calibration of constitutive models, and finite element analysis. The outline is structured as followed:

- Chapter 1: The background of the thesis is presented, together with the introduction of the constitutive models to be used. The research objectives and thesis outline are indicated at the end of this chapter.
- Chapter 2: The literature review is given. Initially, the current application and design method of the suction pile foundation are summarized. Then, The previous research relevant for this

study(i.e., finite element analysis for suction pile foundation, soil constitutive models) is reviewed. Last, the study of different constitutive models is presented.

- Chapter 3: A soil report from SPT Offshore is interpreted, and the soil data for the calibration of soil models is preprocessed.
- Chapter 4: Four soil constitutive models are calibrated, and the input parameters for PLAXIS are presented. Afterwards, numerical and real laboratory test results are compared.
- Chapter 5: The 3D finite element models are introduced and analyzed by using different soil models. The results of deformation, capacity, and compliance matrix are compared.
- Chapter 6 The last chapter summarize the research findings and pointed out the limitations and recommendations for future study.

# 2

# Literature review

## 2.1. Suction pile in practise

Apart from the application cases, different soil conditions, foundation loads, and feasibility of installation also influenced the ratio (L/D ratio) for suction foundations. Optimizing the sizes is the final objective for engineers and scientists. In practice, the whole design process is divided into structural engineering and geotechnical engineering part. The consistency of parts is achieved by an iterative design approach, as illustrates in Figure 2.1(Sturm, 2017). The foundation capacity assessment for undrained loading and the foundation stiffness calculation, including corresponding soil reactions, are the most relative stage of this thesis.

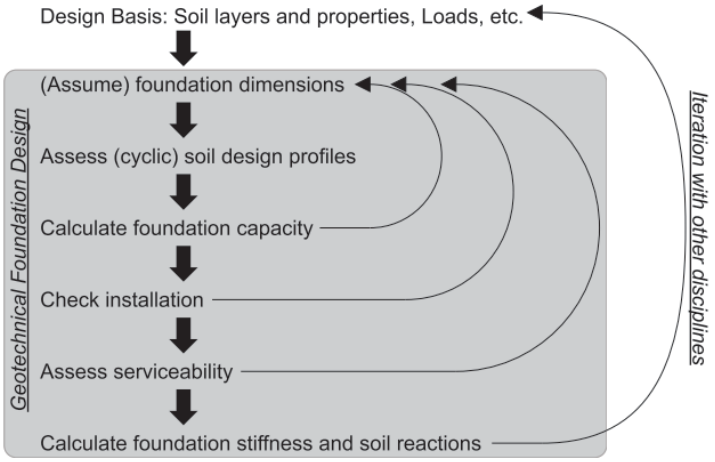


Figure 2.1: Schematic presentation of the iterative and interdependent work- flow of suction caissons design (Sturm, 2017)

To determine the holding capacity of suction caissons, in practice, the analysis tools can be categorized as one of the methods below. These are (in order of detail) semi-empirical methods (highly simplified models of soil resistance including beam column models)(Andersen et al., 2015), limit equilibrium or plastic limit analysis methods(models involving soil failure mechanisms) and the finite element method (advanced numerical analysis).

In current practice geotechnical design(Cathie et al., 2019), the ultimate capacity of a caisson have been estimated using the methods described by Brinch Hansen (1970). The shape and depth factors are applied to improve the standard Terzaghi bearing capacity formula. The Brinch Hansen equations are adopted in ISO 19901-4(2016) and DNVGL-RP-C212(2017). The superstructure is ignored but re-

places by the reaction force applied to the SPF(Figure 2.2). The Load Reference Point is the centre of top plate at mudline level.

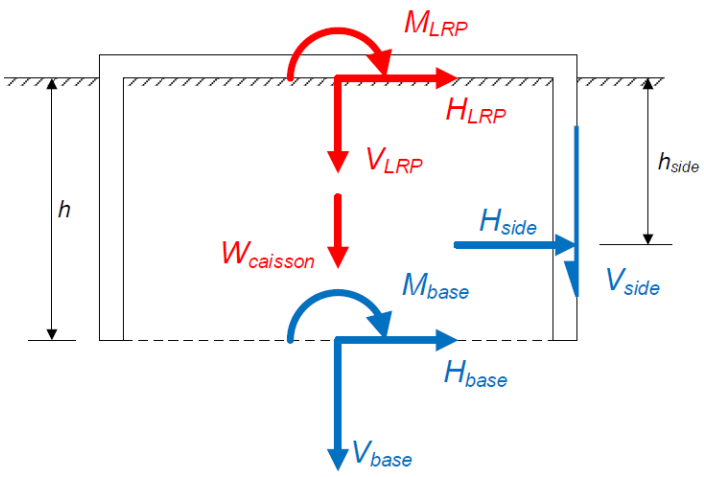


Figure 2.2: Load - capacity conversion (Cathie et al., 2019)

∗Note: Applied forces from structure at Load Reference Point(red), and resulting forces applied to soil from side and base of caisson(blue).

Figure 2.2 illustrates the reaction forces apply at the LRP, the weight of the caisson, and trapped soil and the consequent forces on the skirt and bottom of the caisson. The Equation 2.1 explains the relationship of these forces. The term $W_{caisson}$ should include the (buoyant) weight of the soil trapped in the caisson $\frac{\pi D_i^2 h\gamma'}{4}$, also the weight of any part of the caisson structure not yet accounted for in $V_{LRP}$. Due to the limit equilibrium methods are used to find the resistance force(blue), it is rarely possible getting a single solution for the allowable loads.

$$V_{LRP} + W_{caisson} = V_{base} + V_{side} \tag{2.1a}$$

$$H_{LRP} = H_{base} + H_{side} \tag{2.1b}$$

$$M_{LRP} = M_{base} - h_{side}H_{side} - hH_{base} \tag{2.1c}$$

Another approach is to define the ultimate resistance of a SPF directly in the form of VHM failure envelopes. Conceptual VHM envelopes for shallow skirted foundations under drained and undrained loading, a rotated parabolic ellipsoid represents the locus of VHM loads at failure. In the MH plane this manifests as a rotated ellipse, whilst a parabola is applicable to planes along the V axis at ratios of constant $M/H$.

There are more numerical studies for undrained loading, Bransby and Randolph have investigated the failure mechanisms, and V-H-M envelopes for shirt foundation by using 2D finite-element models in 1998. They found the yield locus was eccentric in H-M space and concluded that the shallow foundation's behavior was expected to be mechanistically similar to the simple strip footing in their study. In 2000 and 2005, Taiebat and Carter did numerical studies for caisson foundations embedded in a uniform soil domain under undrained load. They investigated a representative suction pile's performance under isolated axial, torsional, lateral loads, and the combination by using FEM. In a non-dimensional form, a unique failure envelope could be suggested for caisson neglect the pad eye's location.

The closed-form expression of the V-H-M envelop, proposed by Gourvenec and Barnett (2011), gave a prediction of undrained bearing capacity of caisson foundation for variant embedment ratios

and soil strength profile. A series of studies by Palix et al. (2011) and Kay and Palix (2011) investigated the V-H-M envelopes for $L/D$ ratios from 1.5 to 6 and broad soil strength profile. They made a collation of the results from different analysis software(PLAXIS, CANCAP2, and HARMONY). Although the V-H-M envelopes were similar, the FEM analysis(PLAXIS and HARMONY) educed more reliable results than the limit equilibrium method(CANCAP2). Some more advanced results could also be found in Vulpe (2015), in this research, the changing roughness of the soil-skirt interface was included. Vulpe also illustrated the relationship between loading combination and failure mechanism.

An advanced method name macro-element or force-resultant model is in the research stage to analyze SPF. In this method, the whole SPF and the soil domain was generalised as a 2D or 3D force-resultant model (Yin et al., 2020).

## 2.2. Previous study of interests

In Surarak et al. (2012), a comprehensive set of experimental data on Bangkok subsoils from oedometer and triaxial tests were analyzed. The stiffness and strength parameters for the Hardening soil model were calibrated using the data. The numerical laboratory tests were carried out in PLAXIS. The hardening soil model with the best fit input parameters well predicted the stress-strain relationship, pore pressure, and stress path for the soft clay layer. However, the hardening soil model could not predict the drop in the deviatoric stress or the excess pore pressure for the stiff clay layer, even with the adjusted parameters.

A study by Stapelfeldt et al. (2015) investigated the holding capacity of different geometry suction pile foundations in three different load conditions: the maximum vertical load, the maximum horizontal load, and the minimum vertical load. The analysis used finite analysis software ABAQUS in two and three-dimensional with the hypoplastic constitutive soil model. The study concluded that the analytical solutions have drawbacks in different load conditions compare to numerical analysis.The numerical simulation considered a low pore water pressure under vertical tensile loading and found that horizontal loads could be holden even without extensive vertical loading. The analytical solution is too conservative to analyze tensile and horizontal loads.

In Yilmaz and Tasan (2019), numerical simulations of suction bucket foundations under cyclic axial loading are performed in FE program system ANSYS (2016). The hypoplastic constitutive soil model is used to simulate saturated sandy soil. The result shows the bucket response and excess pore pressure development under different loading level and cycle number. The study concluded that bucket response can be classified as shakedown, attenuation, and incremental collapse; The cyclic loads were transferred into the soil predominantly via top plate and the outer skirt for the case of shakedown; In the case of attenuation and incremental collapse, a greater soil movement relative to bucket was determined due to the excess pore pressure accumulation in soil, which caused additional loads on the bucket. The drawback of this study is no experimental tests to verify the proposed model.

## 2.3. Constitutive models

Constitutive models described the response of materials to different mechanical and/or thermal load conditions that provided stress-strain relationships to formulate government equations, as well as conservation laws and kinematic relationships. The mechanical behavior of soils and rocks may be modeled at varying levels of precision. There are four constitutive models considered in this thesis: Mohr-Coulomb model, Hardening soil model, NGI-ADP model, and Hypoplastic model. The selection of soil models depends on the soil profile(sandy or clay), working condition(loading condition and pore pressure consideration), and outcomes of interest(capacity, settlement, and stiffness).

### 2.3.1. Mohr-Coulomb model

The most common constitutive model, the Mohr-Coulomb model, which is linearly elastic and perfectly plastic involves five input parameters:

| | | | |
|---|---|---|---|
| E | : | Young's modulus | $[kN/m^2]$ |
| $\nu$ | : | Poisson's ratio | [-] |
| c | : | Cohesion | $[kN/m^2]$ |
| $\varphi$ | : | Friction angle | [◦] |
| $\psi$ | : | Dilatancy angle | [◦] |
| $\sigma_t$ | : | Tension cut-off and tensile strength | $[kN/m^2]$ |

The stress-strain relationship of linear elastic perfectly-plastic(LEPP) Mohr-Coulomb model can be divide into two parts: The first stage is elasticity follows Hooke's law, the second stage is plasticity follows Mohr-Coulomb failure criterion. The latter is formulated in a "non-associated plasticity framework" (Green and Hill, 1951). MC model is a simple and transparent model, includes a limited number and explicit parameter which are easy to calibrate from soil test data. The failure behaviour is good to represent in drain condition, the undrained behaviour is not always realistic. According to Hooke's law, this model shows isotropic and homogeneous behaviour. There is no stress-dependent stiffness nor distinction between primary loading and unloading or reloading.

Irreversible strains develop in plasticity. To check if plasticity occurs, a yield function (f) of strain and stress is introduced. Plastic yielding occurs when f=0, which can be present as a contour in biaxial stress and a surface in triaxial stress. Six yield functions ($f_i$) create the full MC yield condition, and setting all yield functions equal to 0, a hexagonal cone is created Fig 2.3(Smith et al., 2015). Due to a limited number of features that soil behaviour shows in reality are included in this model, this model only represents a 'first-order' approximation of soil or rock behaviour.

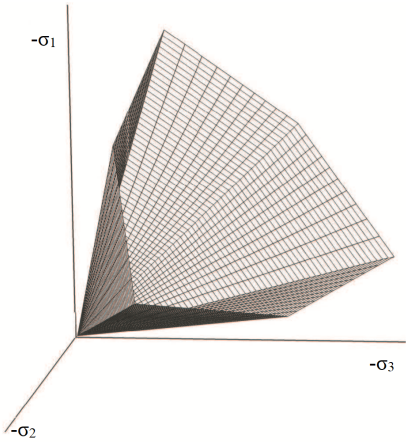


Figure 2.3: The Mohr-Coulomb yield surface in principal stress space (c = 0)

### 2.3.2. Hardening soil model

When subjected to initial deviatoric loading, the soil presents a decreasing of stiffness and developing of irreversible plastic strains. In the typical drained triaxial text, A hyperbola line can well approximate the relationship between the axial strain and the deviatoric stress Fig.2.4. A double-stiffness model for elasticity combined with isotropic strain hardening is used in the hardening soil model to simulate this soil behavior.(Schanz et al., 1999). The Cam-Clay model is the most dominant existing double-stiffness model, which describes the non-linear stress-strain soil behavior. HS exceeds the existing double-stiffness model, the Duncan-Chang model(Hyperbolic model), by distinguishing between loading and unloading and overcoming the restrictions of collapse load computations in the

fully plastic range.

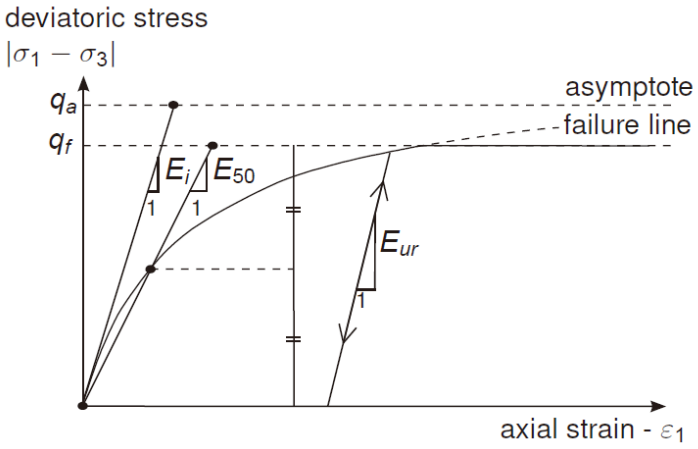


Figure 2.4: Hyperbolic stress-strain relation in primary loading for a standard drained triaxial (Obrzud and Truty, 2018)

Hardening soil model applies the theory of plasticity instead of elasticity, and includes soil dilatancy and introduces a yield cap. Compared to MC(elastic perfectly-plastic) model, the yield surface of HS model is not fixed in principal stress space, but it can expand due to plastic straining. There are two main types of hardening: shear hardening and compression hardening. The shear hardening is used to model irreversible strains due to primary deviatoric loading; additionally, compression hardening is used to model irreversible plastic strains due to primary compression in oedometer loading and isotropic loading(Schanz et al., 1999). The parameters used in HS for PLAXIS 3D are:

Failure parameters as in Mohr-Coulomb model:

| | | | |
|---|---|---|---|
| $c$ | : | (Effective)Cohesion | $[kN/m^2]$ |
| $\varphi$ | : | (Effective) angle of internal friction | [◦] |
| $\psi$ | : | Angle of dilatancy | [◦] |
| $\sigma_t$ | : | Tension cut-off and tensil strength | $[kN/m^2]$ |

Basic parameters for soil stiffness:

| | | | |
|---|---|---|---|
| $E_{50}^{ref}$ | : | Secant stiffness in standard drained triaxial test | $[kN/m^2]$ |
| $E_{oed}^{ref}$ | : | Tangent stiffness for primary oedometer loading | $[kN/m^2]$ |
| $E_{ur}^{ref}$ | : | Unloading / reloading stiffness (default $E_{ur}^{ref} = 3E_{50}^{ref}$ ) | $[kN/m^2]$ |
| m | : | Power for stress-level dependency of stiffness | [-] |

Advanced parameters(it is advised to use the default setting):

| | | | |
|---|---|---|---|
| $\upsilon_{ur}$ | : | Poisson's ratio for unloading-reloading (default $\upsilon_{ur} = 0.2$) | [-] |
| $p^{ref}$ | : | Reference stress for stiffnesses (default $p^{ref} = 100kN/m^2$) | $[kN/m^2]$ |
| $K_0^{nc}$ | : | $K_0$-value for normal consolidation (default $K_0^{nc} = 1 - \sin\varphi$ ) | [-] |
| $R^f$ | : | Failure ratio $q_f$ / $q_a$ (default $R_f = 0.9$) | [-] |
| $\sigma_{tension}$ | : | Tensile strength (default $\sigma_{tension} = 0$ stress units) | $[kN/m^2]$ |
| $c_{inc}$ | : | As in Mohr-Coulomb model (default $c_{inc} = 0$) | $[kN/m^3]$ |

Instead of entering the basic parameters for soil stiffness, alternative parameters can be entered. These parameters are listed below:

| | | | |
|---|---|---|---|
| $C_c$ | : | Compression index | [-] |
| $C_c$ | : | Swelling index or reloading index | [-] |
| $e^{init}$ | : | Initial void ratio | [-] |

The stiffness modulus for real soil depends on the stress level. Hardening soil model calculates stress-dependent stiffness modulus follows Equation 2.2-2.4

$$E_{50} = E_{50}^{ref}\left(\frac{c\cos\varphi - \sigma'_3\sin\varphi}{c\cos\varphi + p^{ref}\sin\varphi}\right)^m \tag{2.2}$$

$$E_{oed} = E_{oed}^{ref}\left(\frac{c\cos\varphi - \frac{\sigma'_3}{K_0^{nc}}\sin\varphi}{c\cos\varphi + p^{ref}\sin\varphi}\right)^m \tag{2.3}$$

$$E_{ur} = E_{ur}^{ref}\left(\frac{c\cos\varphi - \sigma'_3\sin\varphi}{c\cos\varphi + p^{ref}\sin\varphi}\right)^m \tag{2.4}$$

As aforementioned, there are two main types of hardening. The shear hardening yield function follows(Equation 2.5):

$$f = \overline{f} - \gamma^p \tag{2.5}$$

where $\overline{f}$ is a function of stress and $\gamma^p$ is a function of plastic strains(Eq.2.6):

$$\overline{f} = \frac{2}{E_i}\frac{q}{1 - q/q_a} - \frac{2q}{E_{ur}} \qquad \gamma^p = -(2\varepsilon_1^p - \varepsilon_v^p) \approx -2\varepsilon_1^p \tag{2.6}$$

The relationship between $E_i$ and $E_{ur}$ is illustrated in Figure 2.4. Plastic volumetric strains $\varepsilon_v^p$ will never be exactly equal to zero in reality. However, compared with the axial strain plastic volume changes tend to be small in hardening soils, so the approximation in Equation 2.6 for $\gamma^p$ will generally be accurate. For a given constant value of the hardening parameter, $\gamma^p$, the yield condition f=0, can be visualised in p'-q-plane by means of a yields locus. Using Equationss 2.5 and 2.6 as well as Equations 2.2 and 2.4 for $E_{50}$ and $E_{ur}$ respectively, the yield loci plots(for m=0.5, being typical for hard soils):

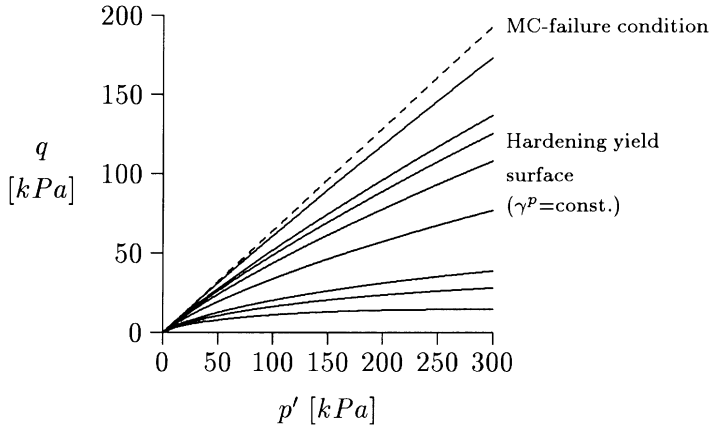


Figure 2.5: Successive yield loci for various constant values of the hardening parameter $\gamma^p$(Schanz et al., 1999)

The compression hardening is mainly detected in softer types of soil. The volumetric yield surface, or the yield cap surface, is formed as an ellipse with the formula Equation.(2.7)(Schanz et al., 1999):

$$f_c = \frac{\widetilde{q}^2}{M^2} + (p')^2 - p_p^2 \tag{2.7}$$

Where M is an auxiliary model parameter that relates to $K_0^{nc}$. The isotropic pre-consolidation stress $p_p$ determines the magnitude of the yield cap, while the intersection with the q-axis is based on $K_0^{nc}$.

With the cap type yield surface, independent input of both $E_{50}^{ref}$ and $E_{oed}^{ref}$ are formulated in HS model. The ellipse is used both as a yield surface and as a plastic potential(associated plasticity).The combination of the shear locus and the yield cap let a simple yield line can be plotted in p-q-plane(Figure 2.6) and a depicts yield surfaces in principal stress space(Figure 2.7). Both the shear locus and the yield cap have the hexagonal shape of the classical Mohr-Coulomb failure criterion. Shear yield locus can expand up to the ultimate Mohr-Coulomb failure surface. The cap yield surface expands as a function of the pre-consolidation stress $P_p$.

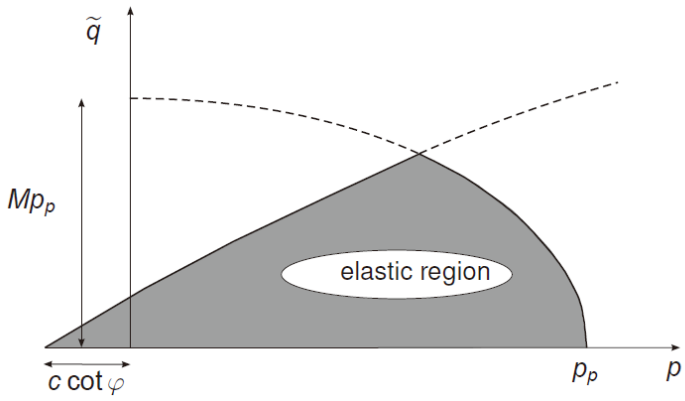


Figure 2.6: Yield surfaces of Hardening Soil model in p -$\tilde{q}$-plane. The elastic region can be further reduced by means of a tension cut-off(Brinkgreve R.B.J., 2018)

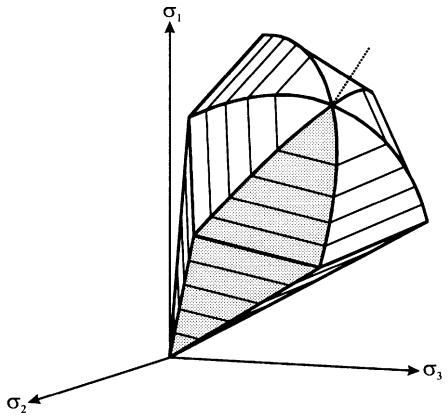


Figure 2.7: Representation of total yield contour of the Hardening Soil model in principal stress space for cohesionless soil(Schanz et al., 1999)

### 2.3.3. NGI-ADP model

Unlike MC and HS, the NGI-ADP model is capable of modeling the anisotropic undrained shear strength behavior(Brinkgreve R.B.J., 2018). In geotechnical engineering, the behavior of clay was generally anisotropic due to complex geological stress history, particle orientation and induced undrained stress path. This anisotropy behavior could be interpreted as the varying stress-strain and strength response due to the different direction of major principal stress to the vertical. Specifically, there was a distinction in the undrained shear strength profiles for triaxial compression(TXC), direct simple shear(DSS), and triaxial extension(TXE) loadings. Taking the foundation under vertical load as an example, Figure 2.8 shows the relevant tests to be used to assess the variation of the undrained shear strength.

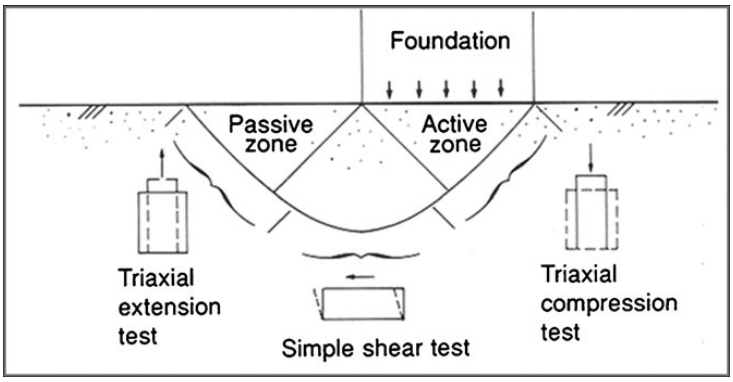


Figure 2.8: Proposed tests for assessment of undrained strength and strain anisotropy along the failure surface under a foundation(Grimstad et al. (2012))

The NGI-ADP model is bases on the undrained shear strength approach with direct input of shear strengths(Grimstad et al., 2012). The input parameter as listed in PLAXIS 3D(Brinkgreve R.B.J., 2018) are:

Stiffness parameters:

| | | | |
|---|---|---|---|
| $G_{ur}/s_u^A$ | : | Ratio unloading/reloading shear modulus over (plane strain) active shear strength | $[kN/m^2]$ |
| $\gamma_f^C$ | : | Shear strain at failure in triaxial compression | [%] |
| $\gamma_f^E$ | : | Shear strain at failure in triaxial extension | [%] |
| $\gamma_f^{DSS}$ | : | Shear strain at failure in direct simple shear | [%] |

Strength parameters:

| | | | |
|---|---|---|---|
| $s_{u,ref}^A$ | : | Reference (plane strain) active shear strength | $[kN/m^2]$ |
| $s_u^{C,TX}/s_u^A$ | : | Ratio triaxial compressive shear strength over (plane strain) active shear strength (default = 0.99) | [-] |
| $y_{ref}$ | : | Reference depth | [m] |
| $s_{u,inc}^A$ | : | Increase of shear strength with depth | $[kN/m^2/m]$ |
| $s_u^P/s_u^A$ | : | Ratio of (plane strain) passive shear strength over (plane strain) active shear strength | [-] |
| $\tau_0/s_u^A$ | : | Initial mobilization (default = 0.7) | [-] |
| $s_u^{DSS}/s_u^A$ | : | Ratio of direct simple shear strength over (plane strain) active shear strength | [-] |

Advanced parameter:

| | | | |
|---|---|---|---|
| $\upsilon'$ | : | Poisson's ratio | [-] |

The yield criterion for the NGI-ADP model in plane strain is defined by Equation.2.8,

$$f = \sqrt{\left(\frac{\sigma_{yy}-\sigma_{xx}}{2} - (1-\kappa)\tau_0 - \kappa\frac{s_u^A - s_u^P}{2}\right)^2 + \left(\tau_{xy}\frac{s_u^A + s_u^P}{2s_u^{DSS}}\right)^2} - \kappa\frac{s_u^A + s_u^P}{2} = 0 \tag{2.8}$$

$\kappa$ was a hardening parameter that depends on the stress path . When $\kappa$ equaled 1.0, the hardening yield curves were indicated by slightly distorted elliptical shapes. The interpolation function used

and values of failure strain control the shape. Elliptical interpolation between failure strain in compression, direct simple shear, and extension is used in NGI-ADP model. The NGI-ADP yield criterion is illustrated for plane strain conditions in Figure 2.9. Contours of constant plastic shear strain and the elliptical failure curve ($\kappa$=1) in the plane strain deviatoric stress are plotted in the figure.

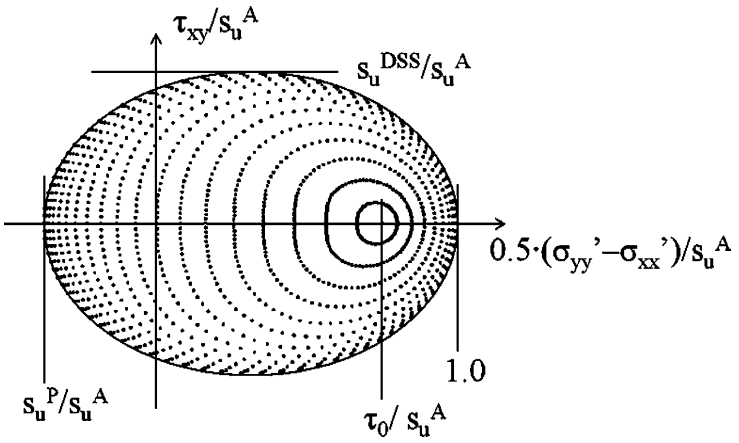


Figure 2.9: 'Typical' deviatoric plane strain plot of equal shear strain contours for the NGI-ADP model.

Using different plastic failure shear strain $\gamma_f^p$ in compression and extension(Figure 2.10) makes the stress path dependent hardening possible(Equation 2.9). $\gamma^p$ and $\gamma_f^p$ are the plastic shear strain and the failure(peak) plastic shear strain, respectively.

$$\kappa = 2\frac{\sqrt{\gamma^p/\gamma_f^p}}{1+\gamma^p/\gamma_f^p} \qquad when \quad \gamma^p < \gamma_f^p \qquad else \quad \kappa = 1 \tag{2.9}$$

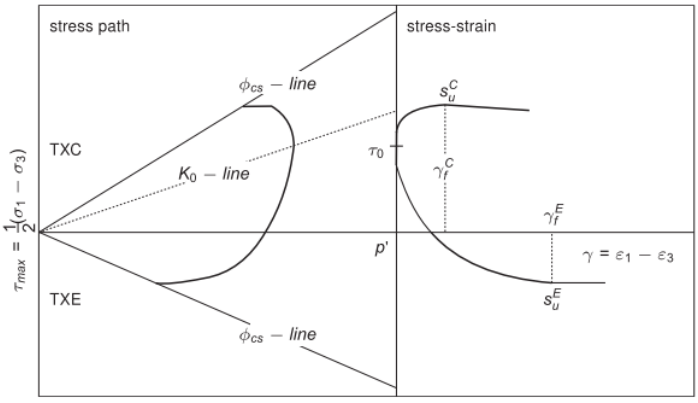


Figure 2.10: Typical stress paths and stress strain curves for triaxial compression and triaxial extension (Grimstad et al., 2012)

A modified deviatoric stress vector is defined for the general stress condition:

$$\begin{bmatrix} \hat{s}_{xx} \\ \hat{s}_{yy} \\ \hat{s}_{zz} \\ \hat{s}_{xy} \\ \hat{s}_{xz} \\ \hat{s}_{yz} \end{bmatrix} = \begin{bmatrix} (\sigma'_{xx} - \sigma'_{xx0} \cdot (1-\kappa)) + \kappa \cdot \frac{1}{3}(s_u^A - s_u^P) - \hat{p} \\ (\sigma'_{yy} - \sigma'_{yy0} \cdot (1-\kappa)) - \kappa \cdot \frac{2}{3}(s_u^A - s_u^P) - \hat{p} \\ (\sigma'_{zz} - \sigma'_{zz0} \cdot (1-\kappa)) + \kappa \cdot \frac{1}{3}(s_u^A - s_u^P) - \hat{p} \\ \tau_{xy} \cdot \frac{s_u^A + s_u^P}{2 \cdot s_u^{DSS}} \\ \tau_{xz} \\ \tau_{yz} \cdot \frac{s_u^A + s_u^P}{2 \cdot s_u^{DSS}} \end{bmatrix} \tag{2.10}$$

where the modified mean stress follows

$$\widehat{p} = \frac{(\sigma'_{xx} - \sigma'_{xx0} \cdot (1-\kappa)) + (\sigma'_{yy} - \sigma'_{yy0} \cdot (1-\kappa)) + (\sigma'_{zz} - \sigma'_{zz0} \cdot (1-\kappa))}{3} = p' - (1-\kappa) \cdot p'_0 \quad (2.11)$$

$\sigma'_{xx,yy,zz0}$ are the initial stresses and p' is the means stress. Modified second and third deviatoric invariants were defined accordingly are defined as:

$$\widehat{J}_2 = -\widehat{s}_{xx}\widehat{s}_{yy} - \widehat{s}_{xx}\widehat{s}_{zz} - \widehat{s}_{yy}\widehat{s}_{zz} + \widehat{s}^2_{xy} + \widehat{s}^2_{xz} + \widehat{s}^2_{yz} \quad (2.12)$$

$$\widehat{J}_3 = -\widehat{s}_{xx}\widehat{s}_{yy}\widehat{s}_{zz} + 2\widehat{s}_{xy}\widehat{s}_{yz}\widehat{s}_{xz} - \widehat{s}_{xx}\widehat{s}^2_{yz} - \widehat{s}_{yy}\widehat{s}^2_{xz} - \widehat{s}_{zz}\widehat{s}^2_{xy} \quad (2.13)$$

In 3D stress space, the yield criterion of the NGI-ADP model is a modified classical Tresca yield criterion, which takes anisotropic undrained shear strength into account Equation. 2.14:

$$f = \sqrt{H(\omega)\widehat{J}_2} - \kappa \frac{s^A_u + s^P_u}{2} = 0 \quad (2.14)$$

where, to approximate the Tresca criterion, the term H($\omega$) is introduced below:

$$H(\omega) = \cos^2(\frac{1}{6}\arccos(1 - 2a_1\omega)) \quad (2.15)$$

Where

$$\omega = \frac{27}{4}\frac{\widehat{J}^2_3}{\widehat{J}^3_2} \quad (2.16)$$

The rounding ratio $a_1$, presented the ratio of $s^C_u/s^A_u$. The ratio generally took a value just beneath 1.0, and the appropriate default is 0.99. Figure. 2.11 illustrated the failure criterion of the NGI-ADP model in the $\pi$-plane (for Cartesian stresses) with the default rounding ratio.

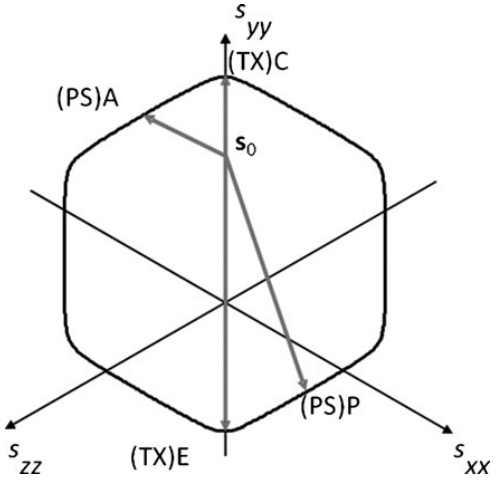


Figure 2.11: Failure criterion of the NGI-ADP model in the $\pi-$plane (Brinkgreve R.B.J., 2018)

The composite strength ratios are constrained by lower limit for combinations of $s^C_u/s^A_u$ and $s^P_u/s^A_u$. The value of $\gamma^p_f$ is derived by elliptical interpolation:

$$\gamma^p_f(\widehat{\theta}) = \frac{\widehat{R}_B\widehat{R}_D\sqrt{\widehat{R}^2_D - \widehat{R}^2_C\cos^2(2\widehat{\theta}) + \widehat{R}^2_C} - \widehat{R}^2_D\widehat{R}_A\cos(2\widehat{\theta})}{\widehat{R}^2_B - (\widehat{R}^2_B - \widehat{R}^2_D)\cos^2(2\widehat{\theta})} \quad (2.17)$$

where

$$\widehat{R}_A = \frac{\gamma^p_{f,E} - \gamma^p_{f,C}}{2} \quad (2.18)$$

$$\widehat{R}_B = \frac{\gamma^p_{f,E} + \gamma^p_{f,C}}{2} \tag{2.19}$$

$$\widehat{R}_C = \sqrt{\gamma^p_{f,E}\gamma^p_{f,C}} \tag{2.20}$$

$$\widehat{R}_D = \frac{\gamma^p_{f,DSS}\widehat{R}_B}{\widehat{R}_C} \tag{2.21}$$

and $\gamma^p_{f,C}$, $\gamma^p_{f,DSS}$, and $\gamma^p_{f,E}$ were the failure plastic maximum shear strain in triaxial compression, direct simple shear, and triaxial extension respectively.

### 2.3.4. Hypoplastic model

The development of the hypoplastic constitutive model could ascend to 1985. The foundation of this model was generalized hypoplasticity combining with traditional critical state soil mechanics. This model is different from elastoplasticity models as there is not distinguishing between elastic and plastic strain. The concepts of the yield surface and plastic potential surface are not explicitly applied in this model (Mašín, 2017). Never the less, these models could predict the substantial parts of the soil behaviour, for example, the critical state, dependency of the peak strength on soil density, nonlinear behaviour in the small and large strain range, dependency of the soil stiffness on the loading direction. The basic hypoplastic equation follows(Equation. 2.22):

$$\overset{\circ}{T} = L : D + N\|D\| \tag{2.22}$$

Thanks to G.Gudehus (1996), the influence of the stress level(barotropy) and the influence of density(pyknotropy) are included in the modified equation(Equation 2.23):

$$\overset{\circ}{T} = f_s L : D + f_s f_d N\|D\| \tag{2.23}$$

Where $f_s$ and $f_d$ are scalar factors indicating the effect of barotropy and pyknotropy. The Matsuoka-Nakai Failure criterion is included in this model by von Wolffersdorff (1996). This model is treated as a standard hypoplastic model for granular material, and this version is also achieved in PLAXIS. As for fine-grained soil, Herle and Kolymbas (2004) modified the model by von Wolffersdorff (1996) to allow for lower friction angles and independent calibration of bulk and shear stiffnesses. Combining this model and the "generalized hypoplasticity" principle by Niemunis (2003), Mašín (2005) developed a model for clays characterized by a simple calibration procedure and capability of correct predicting the very small strain behavior (in combination with the "intergranular strain concept"(Niemunis and Herle, 1997). PLAXIS has the latest clay version.

The aforementioned hypoplastic models generated by Equation. 2.23 provide a good prediction of the soil behavior except for the small strain range. Moreover, they fail to predict the high quasi-elastic soil stiffness in small strain range and upon cyclic loading. Niemunis and Herle (1997) come up with an additional state variable, intergranular strain, to determine the direction of the previous loading. This improvement, often denominated as the "intergranular strain concept, " is utilised in PLAXIS and can be applied with both the model for granular materials and the clays model. The rate formulation of the enhanced model is given by:

$$\overset{\circ}{T} = M : \mathbf{D} \tag{2.24}$$

where M is the fourth-order tangent stiffness tensor of the material, the total strain can be split into two parts: the deformation of interface layers at intergranular contacts, expressed by the intergranular strain tensor $\delta$; the rearrangement of the soil skeleton. For reverse loading circumstances and neutral loading circumstances, the detected total strain is related only to the deformation of the intergranular interface layer, and the soil behavior is hypoelastic. While in continuous loading conditions, the detected total response is also impressed by the particle movement in the soil skeleton, and the soil behavior is hypoplastic (Mašín, 2017).

Hypoplastic model for granular soil

The hypoplastic model for sand is often considered as a reference model for indicating the behaviour of granular materials. There are mainly eight parameters need calibrated in this model-$\phi_c$,$h_s$,$n$,$e_{d0}$, $e_{c0}$,$e_{i0}$,$\alpha$,$\beta$. The parameter calibration procedure has been discussed in different publications (von Wolffersdorff, 1996; Herle and Gudehus, 1999). The methodology mentioned here is mainly based on Herle and Gudehus (1999) and Mašín (2019).

**Critical state parameters $\phi_c$ and $e_{c0}$**: The friction angle of critical state $\phi_c$ is a fundamental parameter governing stress obtained at the critical state (Mašín, 2019). In hypoplasticity, its physical meaning coincides with its meaning within critical state soil mechanics. The most practical approach of calibrating $\phi_c$ is to measure the angle of repose. This principle is based on an ordinary stability analysis of an infinite slope(Figure.2.12). Figure.2.13 shows a simple device for measuring the angle of repose

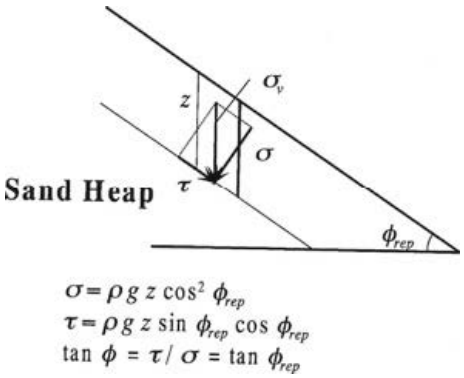


Figure 2.12: Ordinary stability analysis of an infinite slope (Mašín, 2019)

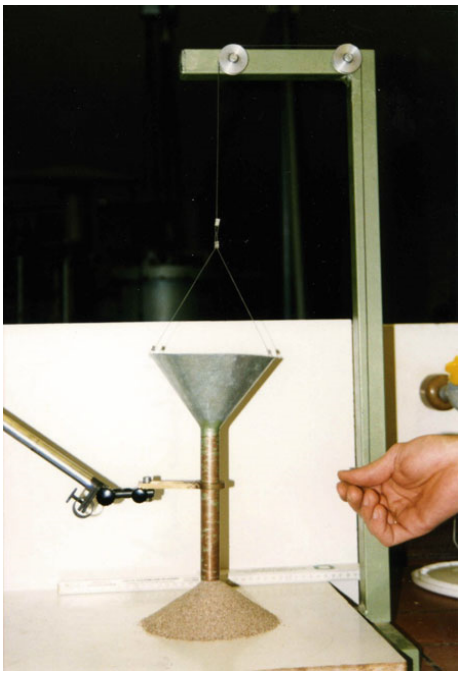

Figure 2.13: Simple funnel device for measuring the angle of repose (Mašín, 2019)

The parameter $e_{c0}$ defines the position of the critical state line in the $p$ versus $e$ plane through Equation 2.25. It is defined as the critical state particle packing at the zero mean stress. The most suitable way to calibrate is based on shear test results; undrained triaxial shear tests are best for the objective, due to the samples are less sensitive to shear banding than in drained tests. The process is demonstrated in Figure 2.14. A simplified way of $e_{c0}$ calibration is taking the initial void ration $e_{max}$ of a loose oedometric specimen as critical state void ratio at zero pressure $e_{c0}$.

$$e_c = e_{c0} \exp[-(\frac{3p}{h_s})^n] \tag{2.25}$$

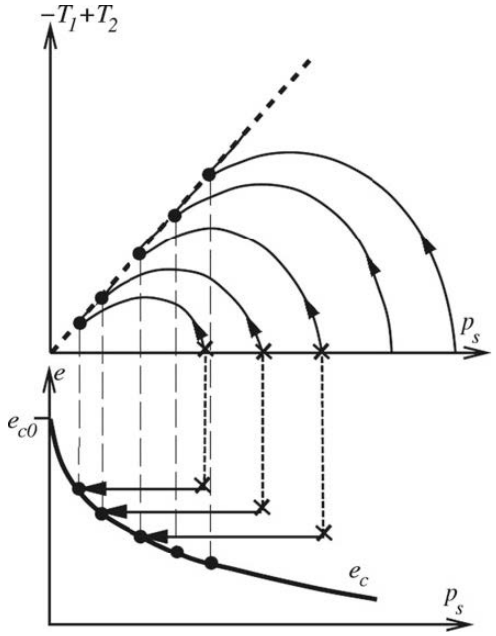


Figure 2.14: $e_{c0}$ calibration using results of undrained triaxial shear tests (Mašín, 2019)

**Limit void ratios $e_{d0}$ and $e_{i0}$**: The reference void ratios $e_{d0}$ and $e_{i0}$ corresponds to the densest and loosest particle packing at the zero mean stress respectively. These two characteristic void ratios are specified as functions of the mean pressure: the minimal void ratio $e_d$ and the void ratio in the loosest state $e_i$. The pressure dependence of there void ratios is supposed in the same form as for the critical state void ratio Eq 2.26:

$$\frac{e_i}{e_{i0}} = \frac{e_d}{e_{d0}} = \exp[-(\frac{3p}{h_s})^n] \tag{2.26}$$

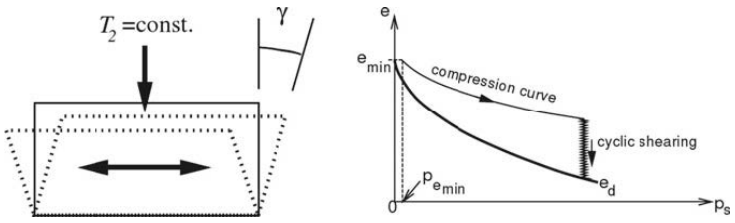


Figure 2.15: Experimental identification of $e_d$ (Mašín, 2019)

The minimum void ratio $e_{d0}$ could be accessed by densification of a granular material by means of cyclic shearing with small amplitude under constant pressure(Fig 2.15). Alternatively, $e_{d0}$ can be obtained by extrapolation using $h_s$ and $n$ calculated from the procedure mentioned in Mašín (2019).The relationship between $e_{d0}$ and $e_{c0}$ has been studied by Herle and Gudehus (1999). In all the cases, the ratio $e_{d0}/e_{c0}$ varied within a comparably limited range of 0.52-0.64. To insure that the soil state does not fall out of the allowed bounds defined by $e_d < e$, a slightly lower ratio(0.5) than the one from the experimentally-determined range 0.52 to 0.64 is chosen(Equation 2.27).

$$e_{d0} = 0.5 e_{c0} \tag{2.27}$$

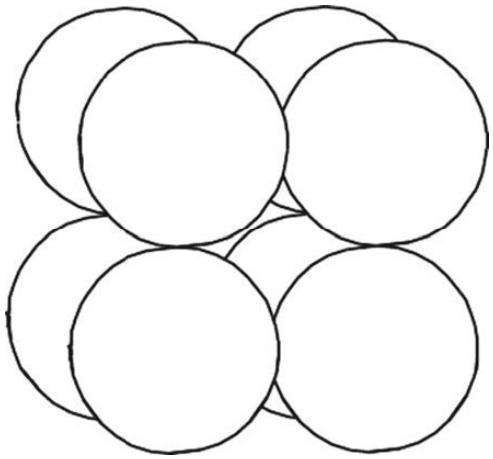

Figure 2.16: Idealised packing of spherical particles at a state of minimum density(Herle and Gudehus, 1999)

Parameter $e_{i0}$ determines the position of the theoretical isotropic normal compression line. An empirical equation for $e_{i0}$ was investigated by Herle and Gudehus (1999), who studied idealised packing of spherical particles at a state of minimum density (Figure 2.16).They proposed the a empirical relationship for $e_{i0}$, which is recommended for $e_{i0}$ calibration (Equation 2.28)

$$e_{i0} = 1.2e_{c0} \tag{2.28}$$

**Stiffness parameters $h_s$ and n**: Parameter $h_s$ and $n$ control the shape of the limiting void ratio curves. The relationships are formulated as Equation 2.25 and 2.26 and plot in 1.1. The parameter $h_s$ denotes the granulate hardness and is used as a reference pressure. The exponent n represent the pressure sensitivity of a grain skeleton (a nun-proportional increase of the incremental stiffness with increasing mean granulate pressure $p_s$).

**Parameter $\alpha$**: Parameter $\alpha$ is an exponent in the definition of density factor $f_d$ that controls the evolution of the soil behaviour toward the critical state. To be specific, this parameter controls the peak friction angle for a given relative void ratio of $r_e$. The drained triaxial test on densely compacted soil samples is used to calibrate this parameter. An increase of the $\alpha$ value increases the predicted peak friction angle. This parameter is generally calibrated by fitting the experimental data using a trial-and-error procedure.

**Parameter $\beta$**: Parameter $\beta$ is an exponent enters the formulation of the barotopy factor $f_s$. This factor scales the whole hypoplastic equation 2.23, it thus controls both the bulk and shear stiffness. The same tests as those used to calculate the parameter $\alpha$ can be used to calibrate this parameter. An increase of the $\beta$ value increases the soil stiffness. The trial-and-error procedure is used to calibrate parameter $\beta$, which is similar to $\alpha$.

### Hypoplastic model for clay

The hypoplastic model for clay is developed predicting anisotropy of very small strain stiffness. It is based on an explicit asymptotic state boundary surface approach. There are five parameters $\varphi_c$, $N$, $\lambda^*$, $\kappa^*$, $\nu$ in its basic form. These are standard critical state soil mechanics parameters, which are equivalent (but not identical) to the parameters of the Modified Cam-clay model (Mašín, 2019). Additionally, three advanced parameters($\alpha_f$,$O_c$ and $a_y$) are introduced to enhance the fitting capabilities of the model and may be promoted by advanced users to reach a better representation of their experimental data. However, it is possible to use standard values instead of calibrating these parameters.

**Critical state friction angle $\phi_c$**: Even though the physical meaning of this parameter of the hypoplastic clay model is the same as that of the sand model (2.3.4), its calibration differs (Mašín (2019)).

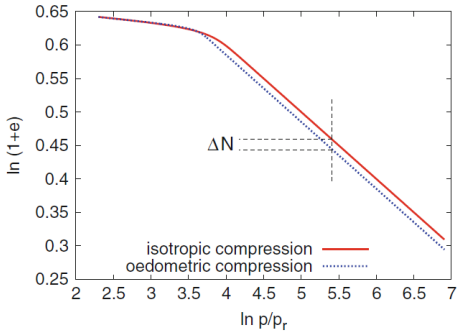


Figure 2.18: Offset of the isotropic and oedometric normal compression lines(Mašín (2019))

$\phi_c$ cannot be calibrated using the simple angle of repose test, but a shear testing is needed in clays. The recommended test is the undrained triaxial shear test(CIUP).

**Parameters $N$ and $\lambda^*$**: Parameter $N$ specifies the position of the isotropic normal compression line, whereas the parameter $\lambda^*$ defines its slope in the $\ln p$ vs $\ln(1+e)$ plane, as shown in Fig 2.17. The isotropic compression test is the best test to calibrate these two parameters, the oedometric compression test may also be used instead.

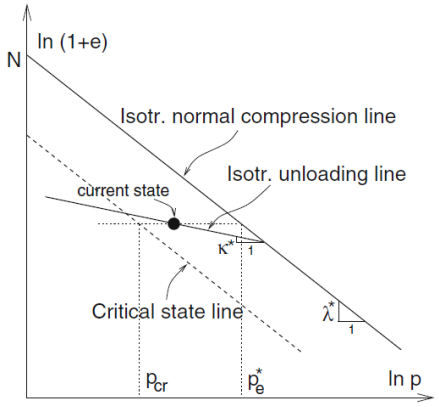


Figure 2.17: Definition of parameters $N$ and $\lambda^*$

$\lambda^*$ also represents a slope of the $K_0$ normal compression line in the $\ln \sigma_a$ vs $\ln(1+e)$ plane (where $\ln \sigma_a$ is vertical stress). The oedometric test can be used to calibrate $\lambda^*$ thanks to the fact that the normal compression line $K_0$ remains constant during loading and Eq 2.29 applies. The parameter N can also be estimated using the oedometric normal compression line in the $\ln \sigma_a$ vs $\ln(1+e)$ plane, but the different positions of oedometric and isotropic normal compression lines need to be consider in calibrating(Fig 2.18).

$$[H] \ln \sigma_a = \ln(\frac{3}{1+2K_0} p) = \ln(\frac{3}{1+2K_0}) + \ln p \tag{2.29}$$

**Parameter $\kappa^*$**: In hypoplastic, the parameter $\kappa^*$ control the slope of the isotropic unloading line which is similar to the Modified Cam-clay model. However, due to the non-linear model formulation the slope of the unloading line is not constant in the $\ln p$ vs $\ln(1+e)$ plane and it varies with the overconsolidation ratio. It is preferable to determine the parameter $\kappa^*$ by direct simulation of the unloading test or by simulation of the compression test starting from the overconsolidated state. Both isotropic(preferable) and oedometric tests can be adopted for this purpose. The parameter $\kappa^*$ also controls the size of the response envelope in the isotropic unloading direction, as shown in Fig 2.19. This figure also shows that, as a side-effect, the parameter $\kappa^*$ influences the undrained stress

paths. It is different from standard elasto-plastic models and should be considered while optimising calibration of the model.

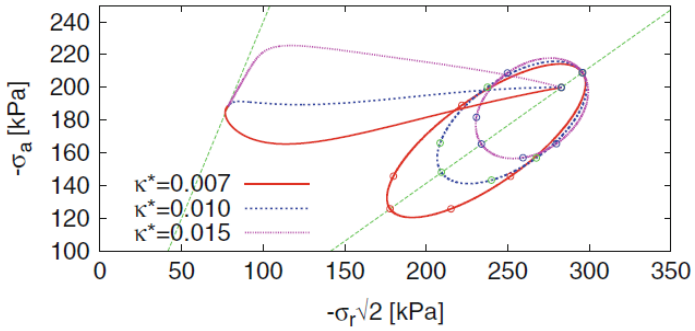


Figure 2.19: The effect of $\kappa^*$ on response envelopes (plotted for normally consolidated state) and its influence on undrained stress paths

**Parameter** $\mu$: Parameter $\mu$ has the classic meaning of the Poisson's ratio within the isotropic elastic tensor $L$. However, in hypoplasticity the non-linear part of the model involving the $N$ tensor also always effects the radial strains, making the influence of $\mu$ on model predictions is different from elasto-plastic models. Similarly to the parameter $\kappa^*$, the triaxial shear tests are used to calibrate $\mu$. This parameter regulates the shear stiffness the same as in the Cam-clay model. An increase of $\mu$ decreases the predicted shear modulus Fig 2.20(a). Other than that, it also affects the evolution of excess pore pressures in the undrained test and thus the undrained effective stress paths 2.20(b). The parameter $\mu$ conducts the aspect ratio of the response envelope, which is the reason why it influences both the shear stiffness and undrained stress path direction (Fig 2.20).

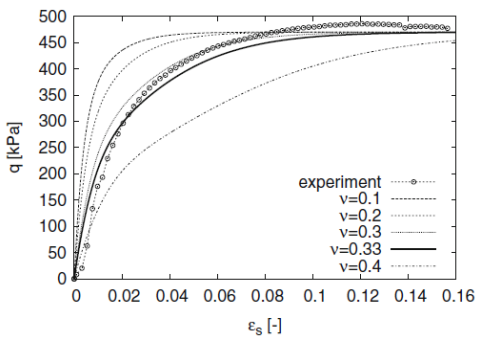


(a) $\mu$'s influence on predicted shear modulus

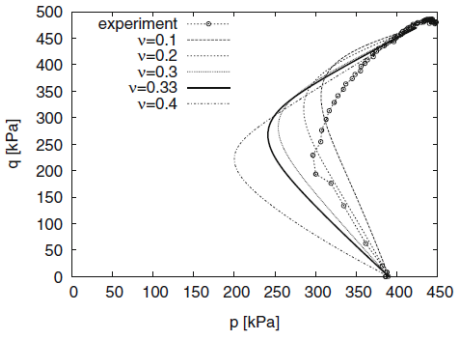


(b) Stress paths for different $\mu$

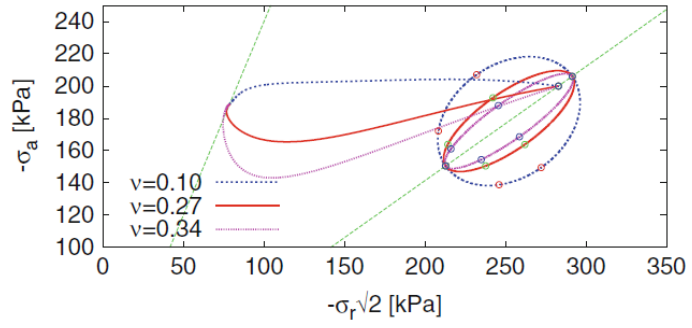


Figure 2.20: The effect of $\mu$ on response envelopes (plotted for normally consolidated state) and its influence on undrained stress paths (Mašín, 2019)

# 3

# Interpretation of Soil Report

In this chapter, a soil report proved by SPT Offshore was introduced. The site investigation and soil laboratory test data were used to calibrate the input parameters for different soil constitutive models. An interpretation of the soil was presented: The section 3.1 gave brief information of the soil profile and an overview of in-site and laboratory tests. The section 3.3 illustrated the strength parameter derivation.

## 3.1. Site information

The site investigation was located in Block 17, offshore West Africa. Different geotechnical offshore activities were carried out:

- 14 × sampling boreholes up to 24m below mudline;
- 14 × Cone Penetration Test (CPT) boreholes up to 60 m below mudline;
- 2 × Combined Sampling and CPT boreholes up to 68 m below mudline;
- 6 × Ball Penetrometer Test (BPT) boreholes up to 10 m below mudline; and
- 4 × seabed sampling exercises using the box corer.

A map showing the borehole and box sampling locations was presented in the Figure 3.1

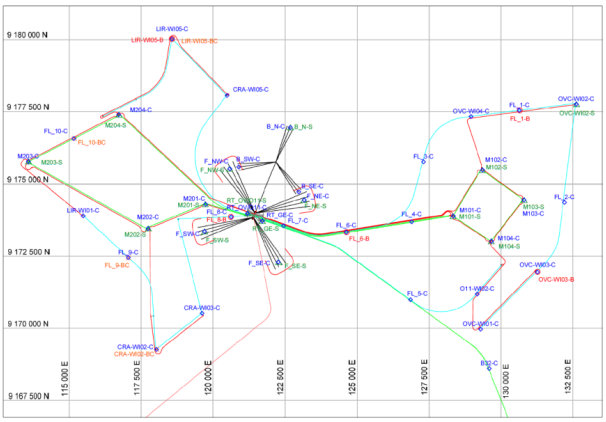


Figure 3.1: Borehole locations map

From Figure 3.1, two key areas have been defined for CLOV field development. Due to the data in more detail in the western area than eastern, the top 24 m (below mudline) soil layer from the western part is modeled. The western areas are the Western Manifolds (M201 to M204) and FPSO/Buoy OLT/Riser Towers, whose water depth is between 1250m and 1400m. The water content and unit weights measured onshore and offshore are given in Figure A.1 and A.2, respectively. A summary of the basic properties of the soil (water content, soil unit weight, and specific gravity) are extracted from the report(Table 3.1).

Table 3.1: Water Content, Submerged Unit Weight, Specific Gravity Design Profiles and Void Ratio

| **Depth(m)** | **Water Content(%)** | **Submerged Unit Weight($kN/m^3$)** | **Specific Gravity (-)** | **Void Ratio(-)** |
|---|---|---|---|---|
| 0.0-1.5 | 180 ↘ 130 | 3.0 ↗ 4.4 | 2.78 | 4.93 ↘ 3.05 |
| 1.5-24.0 | 130 ↘ 110 | 4.4 ↗ 5.5 | | 3.05 ↘ 2.24 |

Note: in all subsequent tables, '↘' = 'reducing to', '↗' = 'increasing to'

According to the Atterberg Limits(Figure A.1), the plasticity index data were presented in Figure 3.2. It could be seen from this plot that a very high plasticity index range(80%-120%) is obtained.

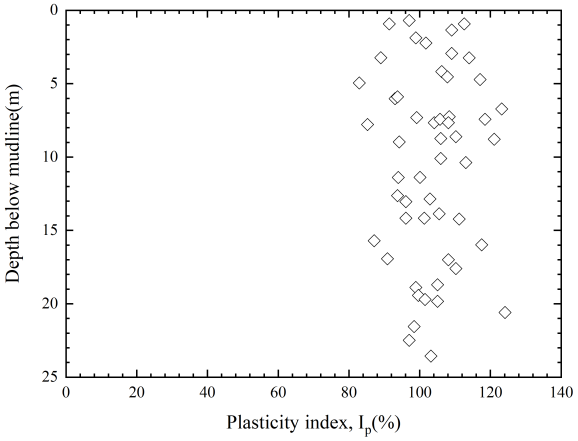


Figure 3.2: Plasticity index profile

Additionally, the over consolidated ratio(OCR) is derived from ILT(incremental loading) and CRS(constant rate of strain) oedometer tests are plotted in Figure 3.3, together with the estimated effective vertical pressure profile $\sigma'_{v0}$ (assuming a submerged unit weight of $3.5kN/m^3$ in the upper 2.5m of the seabed, $4kN/m^3$ from 2.5m to 24m below seabed(Table 3.1). The over-consolidation ratio(OCR) is defined as:

$$OCR = \frac{p'_c}{\sigma_{v0}'} \tag{3.1}$$

Where:

| | | | |
|---|---|---|---|
| $p'_c$ | : | preconsolidation pressure(sometimes referred to as maximum past pressure) | $[kN/m^2]$ |
| $\sigma_{v0}$ | : | initial total vertical stress | $[kN/m^2]$ |

The corresponding OCR profile is plotted in Figure 3.3. The OCR is in the range of 0.6-1.5.

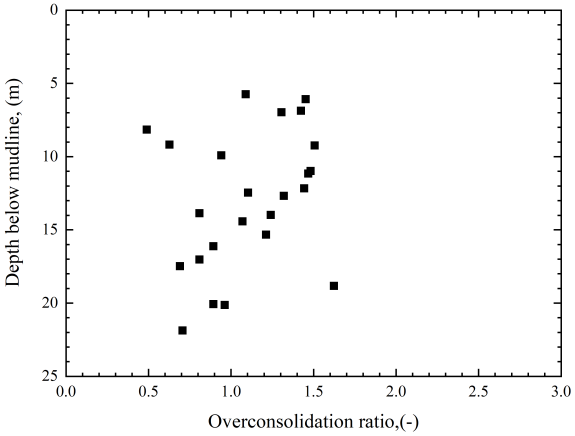


Figure 3.3: OCR profile

The soils encountered within the western part comprise approximately 1 meter of soft CLAY, overlying very soft becoming firm, normally consolidated CLAY, of extremely high plasticity. This thesis is focused on the compression between different constitutive models, so the top 1 meter layer is ignored in further content.

## 3.2. Shear Strength Properties

In the undrained calculation for the clay layer, the shear strength can be defined in terms of their total strength parameter $s_u$. Alternatively, effective parameters cohesion c' and friction angle $\phi'$ are input parameters to calculate undrained shear strength. In this section, the correlations of strength parameters and test data are discussed.

### 3.2.1. CPT data

The CPT raw data (tip resistance, excess pore pressure and sleeve friction) are presented in Figure A.3 to Figure A.8 for western area. The net cone resistance($q_{net}$) is derived from the raw data as follows:

$$q_{net} = q_c + (1-a)u_2 - \sigma_{v0} \tag{3.2}$$

where

| | | | |
|---|---|---|---|
| $q_c$ | : | cone tip resistance | $[kN/m^2]$ |
| $a$ | : | cone area ratio | [-] |
| $u_2$ | : | CPT pore pressure | $[kN/m^2]$ |
| $\sigma_{v0}$ | : | initial total vertical stress | $[kN/m^2]$ |

The net cone resistances are plotted versus depth in Figure A.9 and A.10. The undrained shear strength is deduced from the in-situ CPT and BPT test data via the following equations:

$$s_u = \frac{q_{net}}{N_{kt}} \tag{3.3}$$

$$s_u = \frac{q_b - \sigma_{vo}A_b}{N_b} = \frac{q_b^{corrected}}{N_b} \tag{3.4}$$

where

| | | | |
|---|---|---|---|
| $q_b$ | : | Ball tip resistance | $[kN/m^2]$ |
| $\sigma_{v0}$ | : | initial total vertical stress | $[kN/m^2]$ |
| $N_{kt/b}$ | : | CPT pore pressure | [-] |
| $A_b$ | : | ball area ratio | [-] |

The net CPT tip resistance($q_{net}$) versus mearsured undrained shear strength plot(Figure A.12) indicated the following cone factors($N_{kt}$)(Table 3.2) are best suited to the Western area in the CLOV field, and are recommended for derivation of strength:

Table 3.2: Cone factor $N_{kt}$ by type of test

| Area | $N_{kt}$ value for | | | | | |
|---|---|---|---|---|---|---|
| | CAUc Triaxial test | | DSS test | | CAUe Triaxial test | |
| | Mean | Range | Mean | Range | Mean | Range |
| Western area | 12 | 9.5-14 | 13 | 11-17 | 14 | 14-16 |

### 3.2.2. Laboratory test

From the CPT and BPT result, a normally consolidated strength profile is observed(strength linearly increasing with depth) beyond 1m depth. In order to get more accurate soil behaviour, advanced laboratory element tests were carried out. The undrained shear strength profiles recommended for design are presented in Figure A.13 to A.15 for various test types.

Sixteen strain-controlled Direct Simple Shear(DSS) tests were performed between 6.15m and 23.18m below seabed for the Western area. The DSS test results provided an indication of the strength of the clay under direct shear loading and were therefore applicable for various failure surfaces for different types of seabed structures. The DSS Tests were carried out on undisturbed samples. The samples were consolidated anisotropically ($K_0$ = 0.5). Consolidation was carried out by ramping the cell pressure to the target value and adjusting the deviator stress to obtain the in-site stress level. All the tests were carried out undrained, with the sample maintained at a constant height and constant total vertical stress. The shear stress($\tau_{xy}$) and shear strain ($\gamma$) relationships are given in Figure A.16. $s_u^{CAUc}$ is the maximum shear stress measured during shearing. The design parameter selected from the DSS, CAUc and CAUe tests results is presented in Table 3.3.

Fifteen monotonic triaxial tests(10 compression, 5 extension) were carried out for Western area. All tests were initially consolidated isotropically ($K_0$ = 1.0) to the target confining stress. Then, anisotropic consolidation ($K_0$ = 0.5) was carried out by maintaining the cell pressure and ramping the vertical stress to the target value with the drainage values open. This two-step consolidation procedure was adopted to ensure that shear failure during consolidation did not occur. After consolidation phase completed, the shearing phase of the triaxial test was conducted at a nominal constant rate of vertical displacement of 1% axial strain/hr. The deviator stress(q) versus axial strain($\epsilon_a$), pore pressure ($\Delta u$) versus axial strain($\epsilon_a$) and deviator stress(q) versus mean effective stress($p'$) are presented in Figure A.17 and A.18 for CAUc and CAUe triaxial tests respectively.

Table 3.3: $S_u$ Design Profiles

| Depth(m) | $s_u^{DSS}(kPa)$ | $s_u^{CAUc}(kPa)$ | $s_u^{CAUe}(kPa)$ |
|---|---|---|---|
| 0.0-1.0 | 10.0 | 11.0 | 9.0 |
| 1.0-24.0 | 3.0 $\searrow$ 35.0 | 3.5 $\searrow$ 38.0 | 2.5 $\searrow$ 32.0 |

Undrained shear strength anisotropy is evaluated by comparing results from CAUe triaxial tests to CAUc triaxial tests and comparing results from DSS tests to CAUc triaxial tests. Due to the linear

increase shear strength, the anisotropy ratio is calculated by Eq 3.5.

$$s_u^{DSS}/s_u^{CAUc} = \overline{s_u^{DSS}}/\overline{s_u^{CAUc}} \tag{3.5a}$$

$$s_u^{CAUe}/s_u^{CAUc} = \overline{s_u^{CAUe}}/\overline{s_u^{CAUc}} \tag{3.5b}$$

where

| | | | |
|---|---|---|---|
| $\overline{s_u^{DSS}}$ | : | average shear strength of DSS tests | $[kPa]$ |
| $\overline{s_u^{CAUc}}$ | : | average shear strength of CAUc triaxial tests | $[kPa]$ |
| $\overline{s_u^{CAUe}}$ | : | average shear strength of CAUe triaxial tests | $[kPa]$ |

The anisotropy ratios are presented in Table 3.4.

Table 3.4: Anisotropy ratios

| Ratio | Western area |
|---|---|
| $s_u^{DSS}/s_u^{CAUc}$ | 0.92 |
| $s_u^{CAUe}/s_u^{CAUc}$ | 0.83 |

The other two effective strength parameters c' and $\phi'$ are calibrated by using the aforementioned 10 CAUc triaxial tests. By plotting the failure circle for the ten triaxial tests, the best fit Mohr-Coulomb failure line(c'=3.42kPa and $\phi' = 30°$) are found Figure 3.4. The Mohr-Coulomb failure circle also shows the strength is advanced with the increase of depth(stress-level).

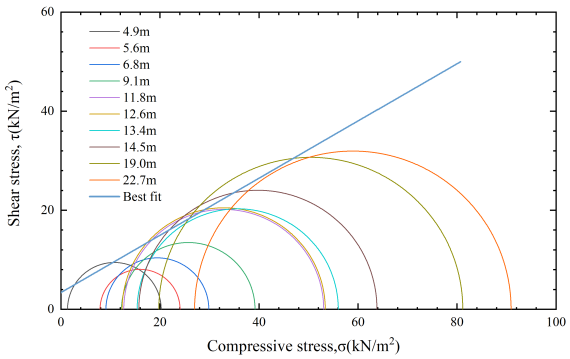


Figure 3.4: Mohr-Coulomb failure circle

## 3.3. Soil Stiffness Properties

For different constitutive models, the input stiffness parameters are distinguishing. An overview of the soil behavior of this site is essential for further calibration. In this section, an interpretation of soil stiffness properties is provided base on the soil report. The three laboratory data( DSS, CAUc, CAUe) are used to illustrate the soil behavior; the determination process for the different tests is provided. Additionally, the correlations of soil stiffness and oedometer/CRS tests, CPT test, OCR, water content are also included to verify.

For the standard determination process, the isotropic drained triaxial test results are used to obtain soil stiffness properties. In section 3.2.2, all the samples are consolidated anisotropically. So

the following paragraph gave the explanation of the numerical definition of stiffness parameter in anisotropic laboratory tests. The numerical laboratory tests are carried out by using SoilTest (Brinkgreve R.B.J., 2018) whose results verified the definition.

The stress and strain relationship of the three laboratory data(DSS, CAUc and CAUe) are plotted Figure A.16, A.17(a) and A.18(a) respectively. For illustration purposed, the laboratory test for soil at depth around -14m were presented and discussed.

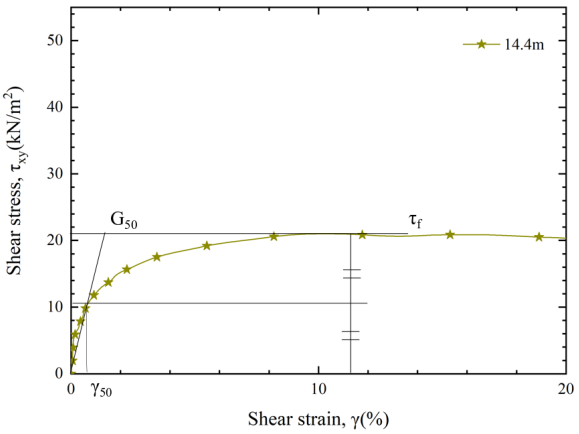


Figure 3.5: Soil stiffness in DSS test

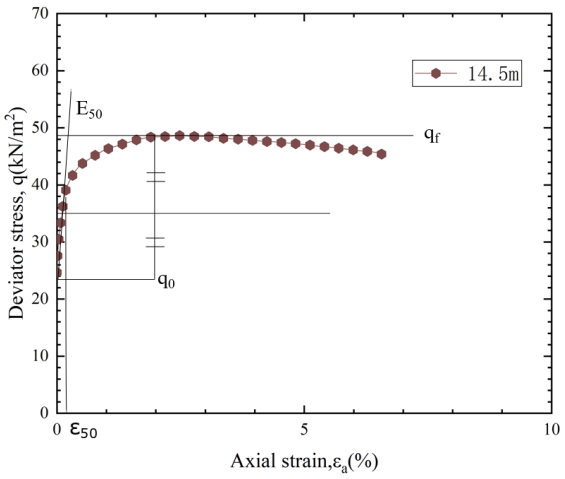


Figure 3.6: Soil stiffness in CAUc test

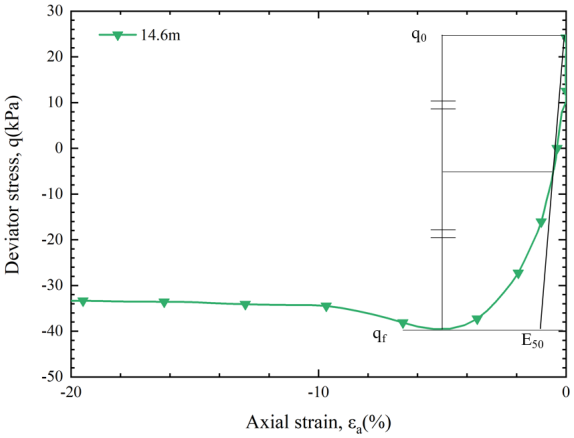


Figure 3.7: Soil stiffness in CAUe test

An assumption for normally consolidation clay is applied here(Eq 3.6) to deriving the scant stiffness $E_{50}$ of direct shear tests:

$$E_u^{50} = 3G_{50} \tag{3.6}$$

The stiffness parameters $E_{50}$ are calculated for all the laboratory tests and plotted in Figure 3.8. The soil behaviour is quite diverse for different laboratory tests.

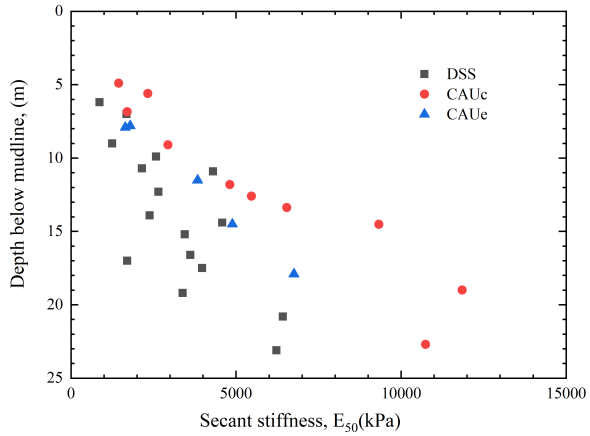


Figure 3.8: $E_{50}$ for different laboratory tests

The undrained Young's modulus, $E_u$, could be estimated by using empirical correlations with undrained shear strength, $c_u$:

$$E_u = nc_u \tag{3.7}$$

Where n is a constant that depends on stress level, overconsolidation ratio, clay sensitivity, and other factors(Ladd and Foott, 1978). Because soil behavior is non-linear, the choice of relevant stress level is very important. Figure 3.9 presents data for normally consolidated soils from Ladd and Foott (1978) that showed the variation of the ratio $E_u/c_u$ with stress level for seven different cohesive soil, (15<PI<75). Figure 3.9 shows the variation of $E_u/c_u$ with overconsolidation ratio(OCR) at two stress levels for the same soil types. Duncan and Buchignani (1976) also proposed a relationship between OCR and PI based on elastic modulus values back-calculated from settlement performance of foun-

dations at various sites. Fig 3.10 illustrates the correlations developed by Duncan and Buchignani (1976).

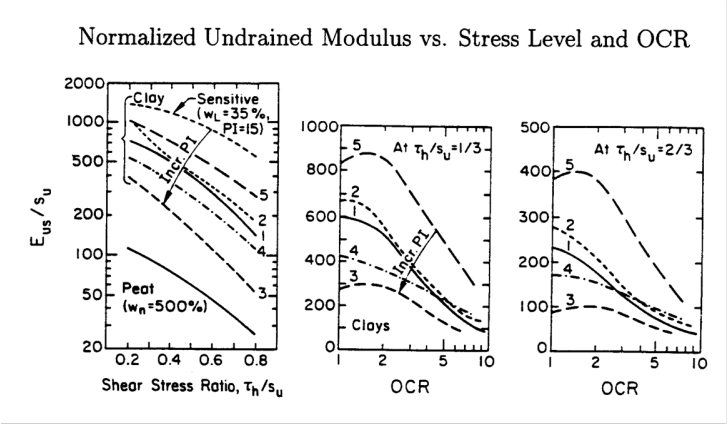


Figure 3.9: Estimation of Undrained Modulus from Ladd and Foott (1978)

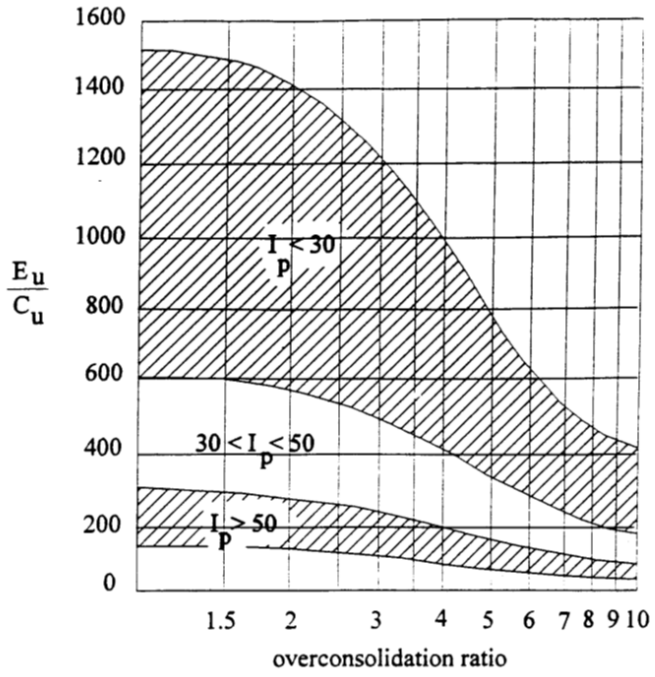


Figure 3.10: Correlation for elastic modulus from Duncan and Buchignani (1976)

The normalized undrained modulus($E_{50}/s_u$) are calculated based on the $E_{50}$(Figure 2.2). The Figure 3.11 showed the $E_{50}/s_u$ Distribute in the range of 100 to 400 which fit the correlation developed by Ladd and Foott (1978) and Duncan and Buchignani (1976)($OCR \sim 1.2$ & $I_p \sim (80\% - 120\%)$). The OCR and $I_p$ profiles are provided in Figure 3.3 and 3.2

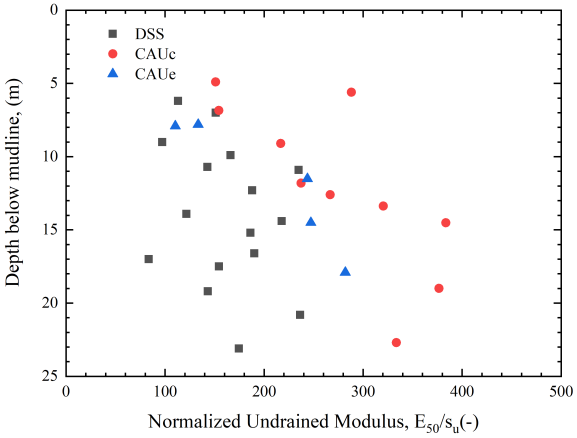


Figure 3.11: Normalized undrained modulus profile

Additionally, A total of eleven 'Constant Rate of Strain'(CRS) consolidation tests were carried out for Western area. The compression index, $C_c$, is obtained from the plots of void ratio and effective stress in a logarithmic scale(3.12). It described the variation of the void ratio $e$ as a function of the change of effective stress $\sigma_{ef}$(Eq 3.8).

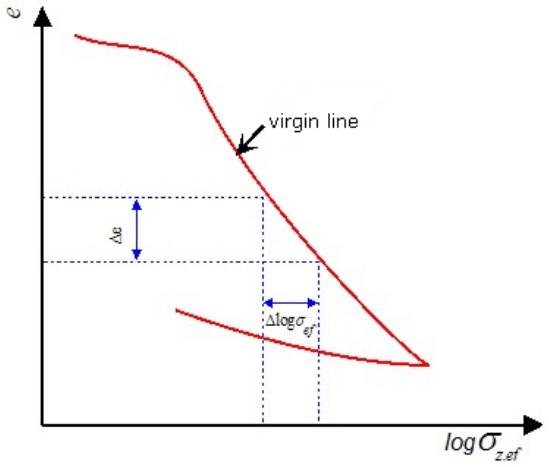


Figure 3.12: Void ratio e versus effective stress $\sigma_{ef}$

$$C_c = \frac{\Delta e}{\Delta \log \sigma_{ef}} \tag{3.8}$$

The CRS consolidation tests were carried out for soil samples from the different depth below the seabed, the compression index profile plots in Fig 3.13. The compression index is in a higher range(1.4-1.8). The oedometer stiffness $E_{oed}$ is derive by Eq 3.9 forward. The reference stress $p_{ref}$ is 100kPa as default. The initial void ratio is the start point of each oedometer test. Figure 3.14 illustrates the oedometer stiffness profile at 100kPa.

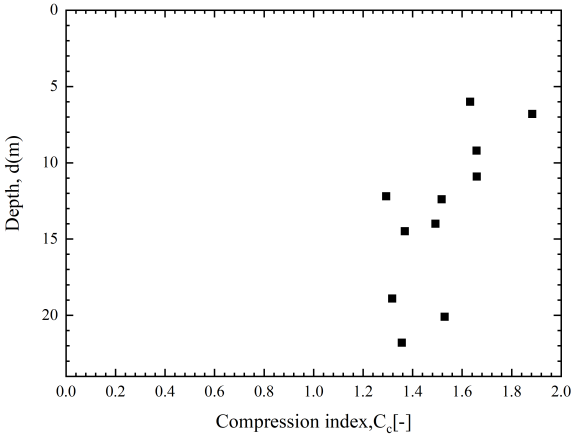


Figure 3.13: Compression index profile

$$E_{oed}^{ref} = \frac{2.3(1+e_{init})p_{ref}}{C_c} \tag{3.9}$$

where

| | | | |
|---|---|---|---|
| $E_{oed}^{ref}$ | : | Oedometer stiffness at reference stress level | $[kN/m^2]$ |
| $e_{init}$ | : | Initial void ratio | [-] |
| $p_{ref}$ | : | Reference stress here | $[kN/m^2]$ |
| $C_c$ | : | Compression index | [-] |

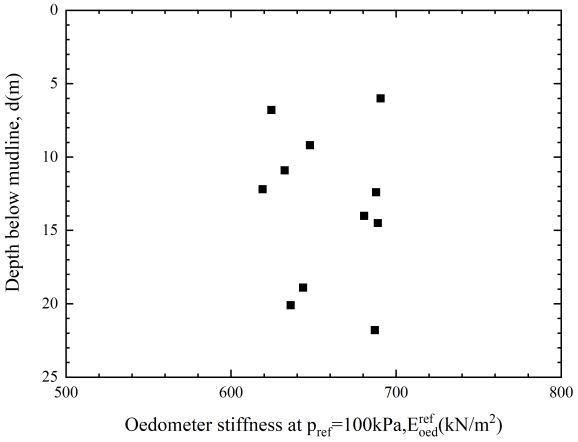


Figure 3.14: Oedometer stiffness profile($p_{ref} = 100kPa$)

The oedometer stiffness $E_{oed}^{ref}$ is derived by the compression index from the oedometer test is significantly lower than the secant stiffness $E_{50}$. The main reason for this phenomenon is that the initial void ratio was very high(Table 3.1). In other laboratory tests(DSS, CAUc, and CAUe), the soil sample was allowed to fully consolidate, and the stiffness was increased due to the pore pressure dissipate.

## 3.4. Summary

In the previous sections, the soil data from the site investigation of Block 17, offshore West Africa are discussed. The in-site data(CPT and BPT) and the laboratory test data(CAUc triaxial, CAUe triaxial, DSS, and oedometer test) are included to describe the soil profile to be modelled. There are mainly two parts for the input parameters in FEM: shear strength properties and soil stiffness properties. The interpretation initially obtains the shear strength profile($s_u$) and the effective strength parameters($c'$ and $\phi'$). The shear strength profile shows anisotropic behaviour, which is a typical property for soil. Then the stiffness parameters are calibrated by using the stress-strain relationship from the laboratory test. The results are used in the next chapter to calibrate the input parameters for different constitutive models.

# 4

# Calibration of constitutive models

## 4.1. Undrained analysis

To create the input parameters for different constitutive models in PLAXIS, the soil data mentioned in Section 3.1 are used for calibration. There are three available methods to perform an undrained analysis in Plaxis 3D (Brinkgreve R.B.J., 2018). Undrained A, B and C. The three methods can be summarised as follows:

- **Undrained A:** Undrained or short-term material behavior uses effective stiffness and strength properties. The soil is considered incompressible by applying a large bulk stiffness for water, and (excess) pore pressures are calculated, even above the phreatic surface. The undrained shear strength is a consequence of the effective stress state and effective strength parameters.
- **Undrained B:** Undrained effective stress analysis uses effective stiffness parameters and undrained strength parameters. The undrained shear strength is independent of the effective stress state.
- **Undrained C:**Undrained or short-term material behavior uses undrained properties. Excess pore pressures are not explicitly calculated but are included in the effective stresses. All parameters are specified in undrained terms.

The first two types of material behaviour settings(Undrained A and Undrained B) allow PLAXIS to specify undrained behaviour by effective model parameters. According to Terzaghi's principle, total stress $\underline{\sigma}$ can be divided into three parts: effective stresses $\underline{\sigma'}$, active pore pressure $p_{active}$ and pore water pressures $p_w$. Considering water is not supposed to sustain any shear stress, therefore effective shear stresses are equal to the total shear stresses.

$$\underline{\sigma} = \underline{\sigma'} + m\, p_{active} \tag{4.1}$$

where

$$m = \begin{bmatrix} 1 & 1 & 1 & 0 & 0 & 0 \end{bmatrix}^T \tag{4.2}$$

$$p_{active} = \alpha_{Biot} S_{eff} p_w \tag{4.3}$$

Where $\alpha_{Biot}$ is Biot's pore pressure and $S_{eff}$ is the effective degree of saturation Brinkgreve R.B.J. (2018). Additionally, the water pressure in Equation 4.3 is composed of steady state pore stress($p_{steady}$) and excess pore stress ($p_{excess}$)(Equation 4.4). Since the first term is independent of time but considered input data, the time derivative of it equals zero. The latter term was generated during the plastic calculations and consolidation analysis(Equation 4.5).

$$p_w = p_{steady} + p_{excess} \tag{4.4}$$

$$\dot{p}_w = \dot{p}_{excess} \tag{4.5}$$

The inverted form of Hooke's law can be written in terms of the total stress rates and the undrained parameters $E_u$ and $\nu_u$:

$$\begin{bmatrix} \dot{\varepsilon}^e_{xx} \\ \dot{\varepsilon}^e_{yy} \\ \dot{\varepsilon}^e_{zz} \\ \dot{\gamma}^e_{xy} \\ \dot{\gamma}^e_{yz} \\ \dot{\gamma}^e_{zx} \end{bmatrix} = \frac{1}{E_u} \begin{bmatrix} 1 & -\nu_u & -\nu_u & 0 & 0 & 0 \\ -\nu_u & 1 & -\nu_u & 0 & 0 & 0 \\ -\nu_u & -\nu_u & 1 & 0 & 0 & 0 \\ 0 & 0 & 0 & 2+2\nu_u & 0 & 0 \\ 0 & 0 & 0 & 0 & 2+2\nu_u & 0 \\ 0 & 0 & 0 & 0 & 0 & 2+2\nu_u \end{bmatrix} \begin{bmatrix} \dot{\sigma}_{xx} \\ \dot{\sigma}_{yy} \\ \dot{\sigma}_{zz} \\ \dot{\sigma}_{xy} \\ \dot{\sigma}_{yz} \\ \dot{\sigma}_{zx} \end{bmatrix} \tag{4.6}$$

where:

$$E_u = 2G(1+\nu_u);\ \nu_u = \frac{3\nu' + \alpha_{Biot}B(1-2\nu')}{3-\alpha_{Biot}B(1-2\nu')};\ B = \frac{\alpha_{Biot}}{\alpha_{Biot} + n(\frac{K'}{K_w} + \alpha_{Biot} - 1)} \tag{4.7}$$

Therefore, the effective parameters G and $\nu'$ are transformed into undrained parameters $E_u$ and $\nu_u$(Equation 4.7) when the undrained behaviour is set as Undrained A or Undrained B in PLAXIS. The determination of Skempton's B-parameter(B) and Biot pore pressure coefficient($\alpha_{Biot}$ are discussed in Brinkgreve R.B.J. (2018)).

The main difference between undrained (A) and undrained (B) is the strength parameters. In Undrained (A), the material's undrained shear strength is not direct input of the undrained shear strength, but results of effective strength parameters and stress states. So it is important using the correct soil properties(i.e. submerged unit weight $\gamma'$and the initial ratio between horizontal effective stress and vertical effective stress $K_0$) in the finite element model. Pore pressure development plays an essential role in deviating the correct effective stress path leading to failure. However, due to most soil models are not capable of providing the correct effective stress path in undrained loading. So the undrained shear strength will be wrongly produced when the analysis is base on the effective strength parameters. Apart from that, the effective strength parameters are usually not available from soil investigation data for undrained materials. In these situations, the Undrained(B) approach, in which a direct input of undrained shear strength is used.

The last option is undrained (C) in which the undrained behavior is simulated by using a conventional total stress analysis with all parameters specified as undrained. The strength is modeled using direct input of undrained shear strength same as undrained (B). The stiffness is modeled using undrained stiffness parameters. The drawback of undrained (C) is that no distinction between effective stresses and pore pressures. As a result, the effective stresses are explicated as total stresses, and all pore pressures are equal to zero.The allowable drainage types are different for different constitutive models.

In the factor of safety analysis in PLAXIS 3D, the strength reduction method which is performed with mobilised strength properties for the friction angle $\phi'$ and cohesion c', followed by an incremental decrease of $tan\phi'$ and c'(for Mohr-Coulomb model effective strength)( Figure 4.1(a)). However, since the shear strength $s_u$ is directly input in total strength analysis, so the strength is directly reduced by the factor of safety (Figure 4.1(b)). Table 4.1 gives an overview of the models included in this thesis and admissible undrained analysis.

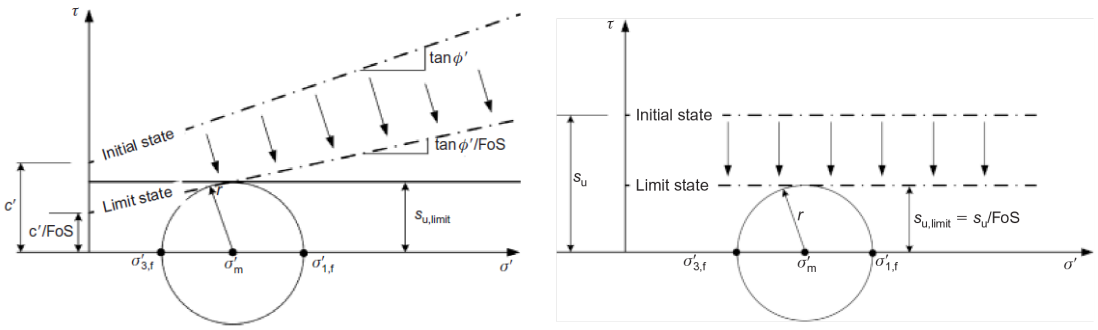


(a) Effective stress analysis (b) Total stress analysis

Figure 4.1: Mohr's circle at failure(Tschuchnigg et al., 2015)

Table 4.1: Overview of models and allowable undrained analysis

| Soil model | Undrained analysis |
|---|---|
| Mohr-Coulomb model | Undrained(A) |
| | Undrained(B) |
| | Undrained(C) |
| Hardening Soil model | Undrained(A) |
| | Undrained(B) |
| NGI-ADP model | Undrained(C) |
| Hypoplastic model (User-defined soil models) | Undrained(A) |

To make sure the behaviour of calibrated soil models capture the laboratory test result data, SoilTest is used to simulate the lab test. SoilTest is provided in the Plaxis 3D. By using SoilTest, different relationship(e.g. stress strain curve) of predefined laboratory tests including DSS, CAUc and CAUe triaxial test can easily generate without setting corresponding finite element modelling (Ukritchon and Boonyatee, 2015). Thus, the estimated input parameter can be optimized and verified to the real laboratory test.

## 4.2. Parameter determination

### 4.2.1. Mohr-Coulomb Model

The Mohr-Coulomb model is calibrated as a reference for the advanced soil models. The drain type for the calculation is undrained for this normally consolidated clay layer. Considering the PLAXIS undrained analysis, for the MC model, there are three types of undrained behaviour which are Undrained(A), Undrained(B) and Undrained(C). The three combination of input in PLAXIS were presented in Table 4.2.

Table 4.2: PLAXIS undrained type input

| Drained type | Input parameter for PLAXIS |
|---|---|
| Undrained A | Effective strength parameters c, $\phi$, $\psi$ |
| | Effective stiffness parameters $E_{50}$, $\nu$ |
| Undrained B | Total strength parameters $c = s_u$ $\phi$=0,$\psi$=0 |
| | Effective stiffness parameters $E_{50}$,$\nu$ |
| Undrained C | Total strength parameters $c = s_u$ $\phi$=0 $\psi$=0 |
| | Undrained stiffness parameters $E_u$, $\nu_u = 0.495$ |

The angle of dilatancy is set to zero, the two reasons are negative dilatancy angle may cause numerical error, and the small-strain behaviour of soil were main part for the simulation. The q-$\epsilon_a$ relationships, shown in Figure A.17(a), is used to calibrate the effective stiffness parameters $E_{50}$ and $\nu$ calibration. The Poisson ratio is assumed as 0.3 for further calculation. The measured stiffness highly depends on the stress level, calibration for the 10 CAUc triaxial test is done to obtain the best fit effective stiffness parameters. However for illustration purposed, only CAUc triaxial tests for 11.8m, 14.5m, and 19.0m are presented and discussed. Numerical CAUc triaxial tests are carried out by using the SoilTest (Brinkgreve R.B.J., 2018). Comparison between the real and numerical CAUc triaxial tests are plotted in Figure 4.2.

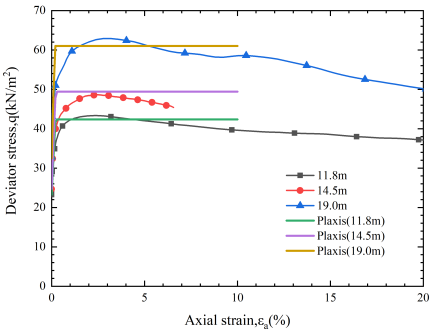


(a) Deviator stress versus axial strain

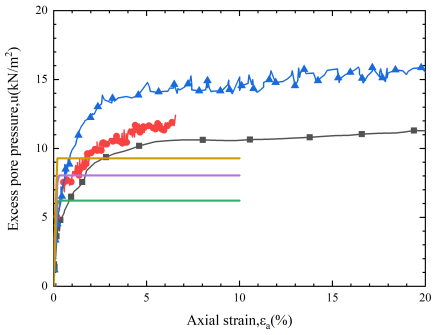


(b) Excess pore pressure versus axial strain

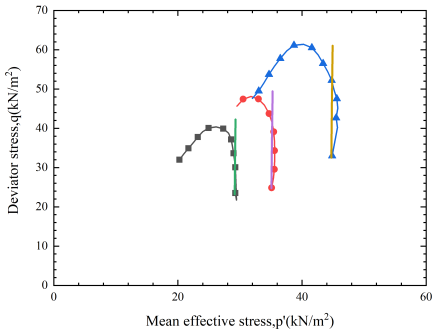


(c) Stress paths $q$ versus $p'$

Figure 4.2: Site A CAUc triaxial testing results and their predictions from the MC(undrain(A)) (Using best fit input parameters)

The results are shown in Figure 4.2(a) revealed good agreements among the stress-strain relationships. Considering the dilatancy angle is not included in the calibration, the stress path (Figure 4.2(c)) also fitted well, which gives a good estimate for the soil strength. However, the MC model fails to model the pore pressure build-up, the condition would be ameliorated by using the Hardening soil model. Although the calibrated MC model well fits the CAUc triaxial tests result, the model gives a higher stiffness value than DSS and CAUe triaxial tests. To deal with the anisotropic behaviour, a best estimate of stiffness profile is obtained(Fig 4.3).

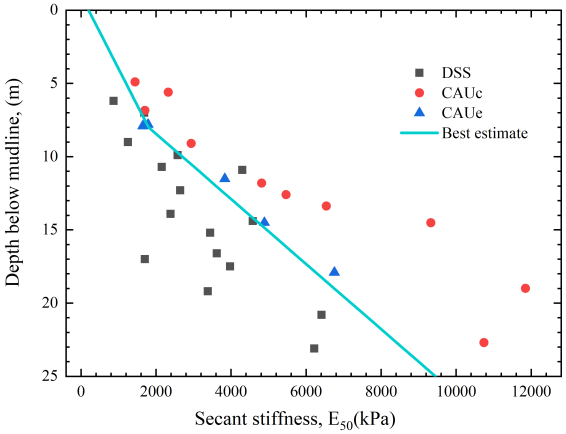


Figure 4.3: $E_{50}$ from different laboratory tests and the best estimate profile

Table 4.3: Calibrated input parameter of Mohr-Coulomb(Undrained(A))

| Layer No[-] | Depth[m]bsf | | Unit Weight $\gamma[kN/m^2]$ | Strength parameters | | | Stiffness Parameters | | |
|---|---|---|---|---|---|---|---|---|---|
| | Top | Base | | $\phi'$ [$\circ$] | $c'$ $[kN/m^2]$ | $\psi$ [$\circ$] | $\nu$ [$-$] | $E_{50}$ $[kN/m^2]$ | $E_{50,inc}$ $[kN/m^2/m]$ |
| 1 | 0 | 9.0 | 13.5 | 30 | 3.42 | 0 | 0.3 | 260 | 260 |
| 2 | 9.0 | 24.0 | | 30 | 3.42 | 0 | 0.3 | 2340 | 585 |

For MC Undrained(B) and Undrained(C), the two strength parameters($\phi'$ and $c'$) are replaced by a total strength parameter $s_u$. In order to take the depth-dependent strength, the shear strength increment $s_{u,inc}$ is included in the input parameters. The similar calibration process is done for Undrained(B) and Undrained(C). The calibrated input parameters are shown in Table 4.4 and 4.5 respectively.

Table 4.4: Calibrated input parameter of Mohr-Coulomb(Undrained(B))

| Layer No[-] | Depth[m]bsf | | Unit Weight $\gamma[kN/m^2]$ | Strength parameters | | Stiffness Parameters | | |
|---|---|---|---|---|---|---|---|---|
| | Top | Base | | $s_u$ $[kN/m^2]$ | $s_{u,inc}$ $[kN/m^2]$ | $\nu$ [$-$] | $E_{50}$ $[kN/m^2]$ | $E_{50,inc}$ $[kN/m^2/m]$ |
| 1 | 0 | 9.0 | 13.5 | 1 | 1.5 | 0.3 | 260 | 260 |
| 2 | 9.0 | 24.0 | | | | 0.3 | 2340 | 585 |

Table 4.5: Calibrated input parameter of Mohr-Coulomb(Undrained(C))

| Layer No[-] | Depth[m]bsf | | Unit Weight $\gamma[kN/m^2]$ | Strength parameters | | Stiffness Parameters | | |
|---|---|---|---|---|---|---|---|---|
| | Top | Base | | $s_u$ $[kN/m^2]$ | $s_{u,inc}$ $[kN/m^2]$ | $\nu$ [$-$] | $E_{50}$ $[kN/m^2]$ | $E_{50,inc}$ $[kN/m^2/m]$ |
| 1 | 0 | 9.0 | 13.5 | 1 | 1.5 | 0.5 | 300 | 300 |
| 2 | 9.0 | 24.0 | | | | | 2700 | 675 |

### 4.2.2. Hardening Soil

The Hardening soil model is the first advance constitutive model to be calibrated. When considering the undrained calculations, there are two types of undrained behavior, which are Undrained(A) and Undrained(B), in this constitutive model. This model have same strength input parameters as Mohr-Coulomb model, so the strength parameter in table 4.3 and 4.4 were applied in this model. The stiffness parameters are discussed in the following sections.

Secant stiffness $E_{50}^{ref}$ and Power law $m$

As introduced in section 2.3.2, the parameter $E_{50}$ is different from MC model, but follows Eq. 2.2. For normal-consolidated soft clay, the power should be taken equals to 1.0(Brinkgreve R.B.J. (2018)), so Eq. 2.2 degenerates to Eq 4.8. To obtain the $E_{50}^{ref}$, the double log scale plot of $E_{50}$(Figure 3.8) and modified confine pressure $\Sigma_3'$(Eq. 4.9) for all the laboratory tests(DSS, CAUc triaxial and CAUe triaxial) is given in Figure 4.4. The reference undrained moduli(at reference pressure of $100kN/m^2$) are $10000kN/m^2$.

$$E_{50} = E_{50}^{ref}\left(\frac{c\cos\varphi - \sigma'_3\sin\varphi}{c\cos\varphi + p^{ref}\sin\varphi}\right) \tag{4.8}$$

$$\Sigma_3' = \frac{c\cos\varphi - \sigma'_3\sin\varphi}{c\cos\varphi + p^{ref}\sin\varphi} \tag{4.9}$$

where

| | | | |
|---|---|---|---|
| $\Sigma_3'$ | : | Modified confine pressure | [-] |
| $c$ | : | Cohesion from MC model(3.42kPa) | $[kN/m^2]$ |
| $\phi$ | : | Friction angle(30°) | [∘] |
| $\sigma_3'$ | : | Confine pressure in laboratory tests | $[kN/m^2]$ |

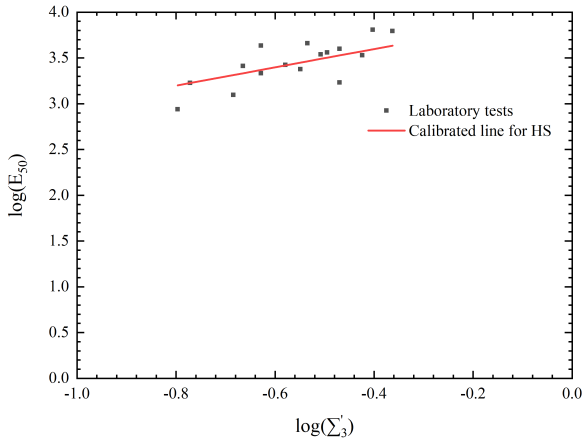


Figure 4.4: Variations of $E_{50}$ with confining pressure

Oedometer stiffness $E_{50}^{ref}$ and Unloading / reloading stiffness $E_{ur}^{ref}$

The Oedometer stiffness obtained from CRS consolidation tests have been illustrated in Fig 3.14. The reference oedometer stiffness(at reference pressure of $100kN/m^2$) are about $600-700kN/m^2$, which was significant lower than the $E_{50}^{ref}$. The default value ($E_{oed}^{ref} = E_{50}^{ref}$) was used as input parameter

for further calculation. The unload/reload tests did not carry out for the soil, so the default value ($E_{ur}^{ref} = 3E_{50}^{ref}$) is used. The summary of calibrated input parameters for Hardening Soil model are shown in Table 4.6.

Table 4.6: Calibrated input parameter of Hardening soil model(Undrained(A))

| Depth[m] | | Strength Parameters | | | Stiffness Parameters | | | |
|---|---|---|---|---|---|---|---|---|
| Top | Base | phi[◦] | c[kPa] | psi[◦] | $E_{50}^{ref}[kPa]$ | $E_{oed}^{ref}[kPa]$ | $E_{ur}^{ref}[kPa]$ | $p^{ref}[kPa]$ |
| 0 | 24 | 30 | 3.42 | 0 | 10000 | 10000 | 30000 | 100 |

### 4.2.3. NGI-ADP model

The description of the NGI-ADP model is given in Section 2.3.3. When considering the undrained calculations, the Undrained(C) is the only setting for this model. Unlike the isotropic constitutive models, NGI-ADP is capable of fitting the different undrained laboratory tests. In this section, the input parameters of the NGI-ADP model are discussed.

Stiffness parameters

The ratio unloading/reloading shear modulus over(plane strain) active shear strength($G_{ur}/s_u^A$) is one of the stiffness parameters. This parameter may be obtained from the slope of unloading and reloading path of stress-strain curve of triaxial compression or direct simple shear tests. The latter test gives direct determination of $G_{ur}$, but the former test gives unloading and reloading Young's modulus $E_{ur}$, where $G_{ur}$ can be calculated as Eq 4.10:

$$G_{ur} = \frac{E_{ur}}{2(1+\nu)} \tag{4.10}$$

However, the reloading/unloading tests are not carried out. When the undrained analysis is applied, the Poisson's ratio is assumed to be 0.5. The $G_{ur}$ is equal to 1/3 of $E_{ur}$ whose value is three times of $E_{50}$ when using default setting(Section 4.2.2). It was reliable to assume that the ratio $G_{ur}/s_u^A$ is equal to normalized undrained modulus($E_{50}/s_u$).Fig 4.5 illustrates the compression of $G_{ur}/s_u^A$ design profile and normalized undrained modulus.

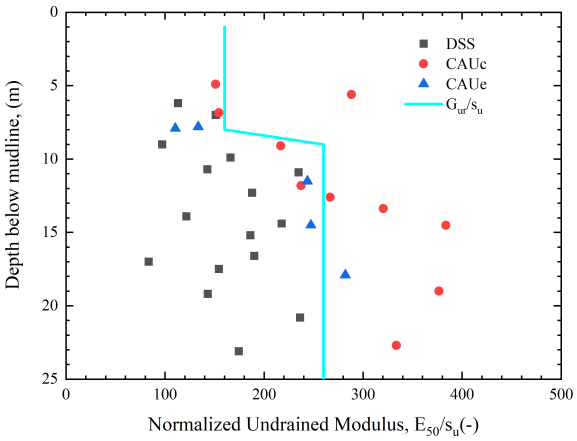


Figure 4.5: $G_{ur}/s_u^A$ and normalized Undrained modulus

The other three stiffness parameters($\gamma_f^C$,$\gamma_f^E$ and $\gamma_f^{DSS}$) are used to independently match failure strains in CAUc, CAUe and DSS respectively. For both tests of CAUc and CAUe triaxial, the failure

shear strain is equal to 3/2 of failure axial strain in CAUc($\epsilon_a^{CAUc}$) and CAUe($\epsilon_a^{CAUe}$), i.e. $\gamma_f^C = 3\epsilon_a^{CAUc}/2$ and $\gamma_f^E = 3\epsilon_a^{CAUe}/2$. The failure shear strain in DSS, CAUc and CAUe tests are presented in Fig 4.6(a) ,4.6(b) and 4.6(c) respectively. The average failure shear strain for each laboratory series is used as the input parameter in PLAXIS.

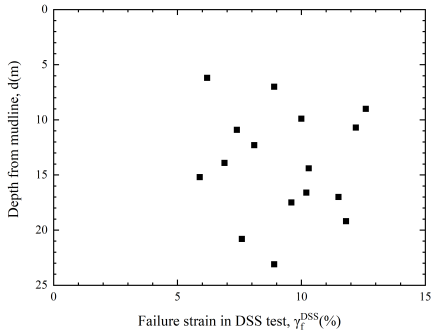


(a) Failure shear strain in DSS tests for different depth soil samples

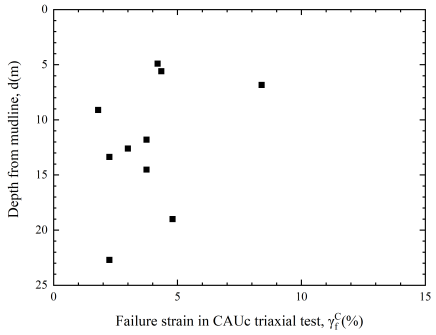


(b) Failure shear strain in CAUc triaxial tests for different depth soil samples

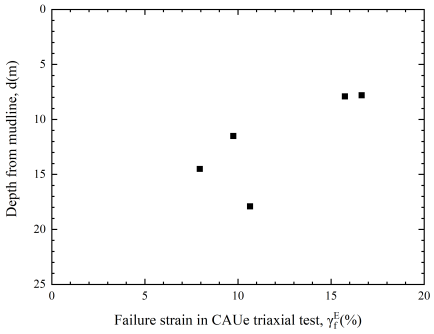


(c) Failure shear strain in CAUe triaxial tests for different depth soil samples

Figure 4.6: Failure shear strain for different laboratory tests

Strength parameters

Basically, there are three parameters for (undrained) shear strength for three different stress path/states, i.e. Active($s_u^A$), Direct Simple Shear($s_u^{DSS}$) and Passive($s_u^P$). The model has the default relationship between undrained shear strength of triaxial compression ($s_u^{CAUc}$) and that of active plane strain condition ($s_u^A$) as:$s_u^{CAUc} = 0.99 s_u^A$. However, the model do not give any relationship between undrained shear strength of triaxial extension($s_u^{CAUe}$) and that of passive plane strain condition($s_u^P$). Here the passive strength ($s_u^P$) is assumed equal to undrained shear strength of triaxial extension($s_u^{CAUe}$). The an-isotropic soil behaviour has been discussed is section 3.2.2.

The summary of the input parameters of NGI-ADP in PLAXIS is given in Table 4.7 and 4.8.

Table 4.7: Stiffness parameters for NGI-ADP model

| Layer No[-] | Depth[m]bsf | | Stiffness parameters | | | |
|---|---|---|---|---|---|---|
| | Top | Base | $G_{ur}/s_u^A$[-] | $\gamma_f^C$[%] | $\gamma_f^E$[%] | $\gamma_f^{DSS}$[%] |
| 1 | 0.0 | 8.0 | 160 | 3.9 | 12.2 | 9.3 |
| 2 | 8.0 | 24.0 | 260 | 3.9 | 12.2 | 9.3 |

Table 4.8: Strength parameters for NGI-ADP model

| Layer No[-] | Depth[m]bsf | | Strength parameters | | | | |
|---|---|---|---|---|---|---|---|
| | Top | Base | $s_{u,ref}^A$ | $z_{ref}$ | $s_{u,inc}^A$ | $s_u^P/s_u^A$ | $s_u^{DSS}/s_u^A$ |
| 1 | 0.0 | 8.0 | 1 | 0 | 1.5 | 0.83 | 0.92 |
| 2 | 8.0 | 24.0 | | | | | |

### 4.2.4. Hypoplastic Model

The Hypoplastic model is a user-defined constitutive model in PLAXIS, the input parameters include aforementioned five parameters of the basic hypoplastic model for clay($\phi_c$, $\lambda^*$, $\kappa^*$, $N$ and $r$)(section 2.3.4). Additionally, There are five intergranular strain concept($m_R$, $m_T$, $R$, $\beta_r$, and $\chi$)(Mašín, 2011). The CAUc triaxial tests are used in the calibration process. The oedometer data is not consistent, so a trial-and-error method is used to calibrate the relative parameters. As shown in Figure 4.7, adjusting the input soil parameters on the left hand and run the same experimental test. Finally, the calibrated parameters are obtained when the strain-stress curve and stress path are fitted to the measured data. The summary of calibrated parameters for the hypoplastic model is in Table 4.9.

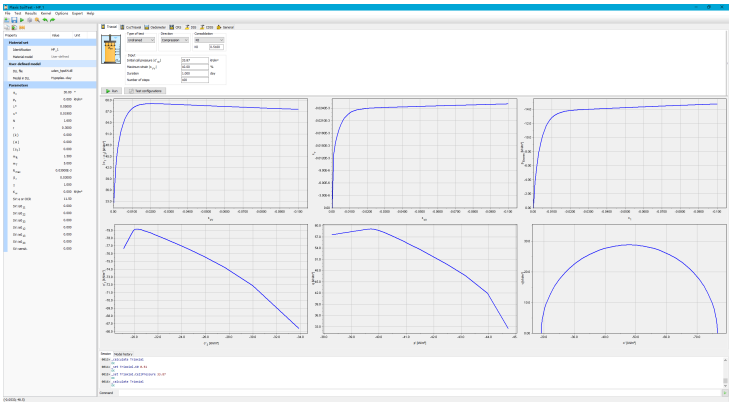

Figure 4.7: Screenshot of SoilTest program

Table 4.9: Soil parameters for hypoplastic model in PLAXIS

| Basic hypoplastic parameters | | Intergranular strain concept parameters | |
|---|---|---|---|
| $\phi_c$ | 30° | $m_R$ | 1.5 |
| $\lambda^*$ | 0.05 | $m_T$ | 5 |
| $\kappa^*$ | 0.019 | $R$ | 0.03E-3 |
| $N$ | 1.6 | $\beta_r$ | 0.03 |
| $r$ | 0.3 | $\chi$ | 1 |

## 4.3. Verification of the calibration

The input model parameters have been calibrated for each models(section 4.2). A series of numerical laboratory tests have been done by using SoilTest to verify the calibration result. There are mainly three shear tests provided from the soil report, which are DSS, CAUc triaxial, and CAUe triaxial tests(section 3.2.2). However, for illustration purpose, only three CAUc triaxial tests and three DSS tests are presented and discussed.

The results shown in Figure 4.8 to 4.10 reveal high agreements of strength among all constitutive models. The advanced soil models(HS, NGI-ADP, and HP) can present the nonlinear behavior of the real soil. The goodness of fit is enhanced with the increasing number of stiffness parameters. There is

no distinction between effective stresses and pore pressures when using undrained(C) in terms of the stress path. Therefore, the effective stress for the NGI-ADP model is interpreted as total stresses. For MC and HS model, a non-zero dilatancy angle $\psi$ may lead to unrealistically high pore pressure and unrealistic liquefaction type of behavior (Brinkgreve R.B.J., 2018). Hence, no dilatancy is included in these models. For HP model, even though it presented a good fit in the stress-strain relationship and the best fit for the stress path, the calibration process is not robust when the lack of reliable test data.

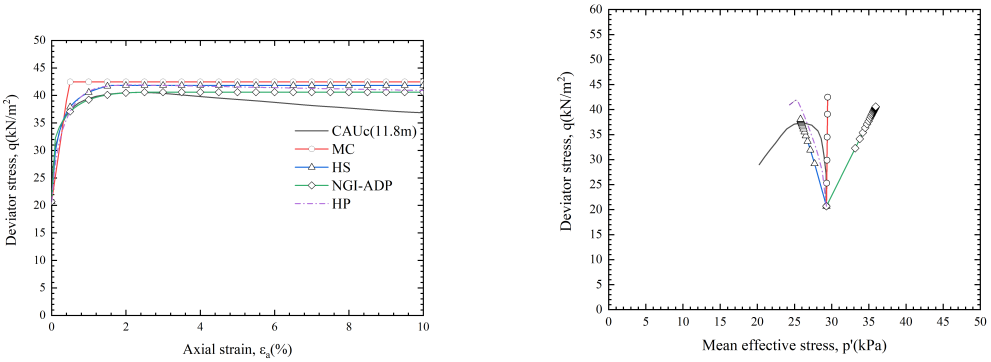


(a) Deviator stress versus axial strain (b) Stress path q versus p'

Figure 4.8: CAUc triaxial test results and their prediction from PLAXIS(11.8m)

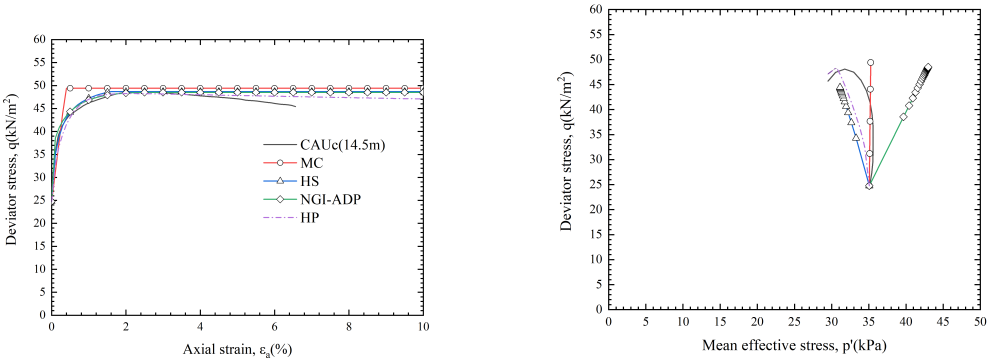


(a) Deviator stress versus axial strain (b) Stress path q versus p'

Figure 4.9: CAUc triaxial test results and their prediction from PLAXIS(14.5m)

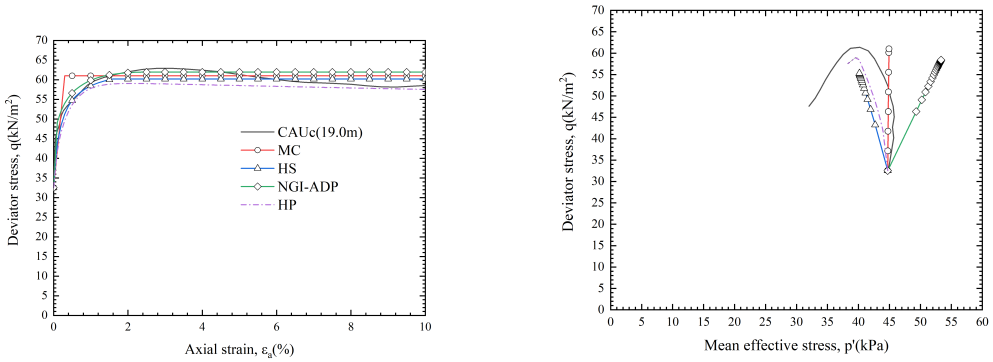


(a) Deviator stress versus axial strain

(b) Stress path q versus p'

Figure 4.10: CAUc triaxial test results and their prediction from PLAXIS(19.0m)

The comparing of DSS tests is plotted in Figure 4.11; all the models presents a good fit for the shear strength level. However, the MC, HS, and HP models overestimate the stiffness of the soil element. MC and HS models are isotropic models that could not fit the CAUc triaxial test and DSS test using the same input parameters. In contrast, the NGI-ADP model considers the different shear strength and stiffness for different laboratory tests; hence, this model can reasonably predict the anisotropic soil behavior.

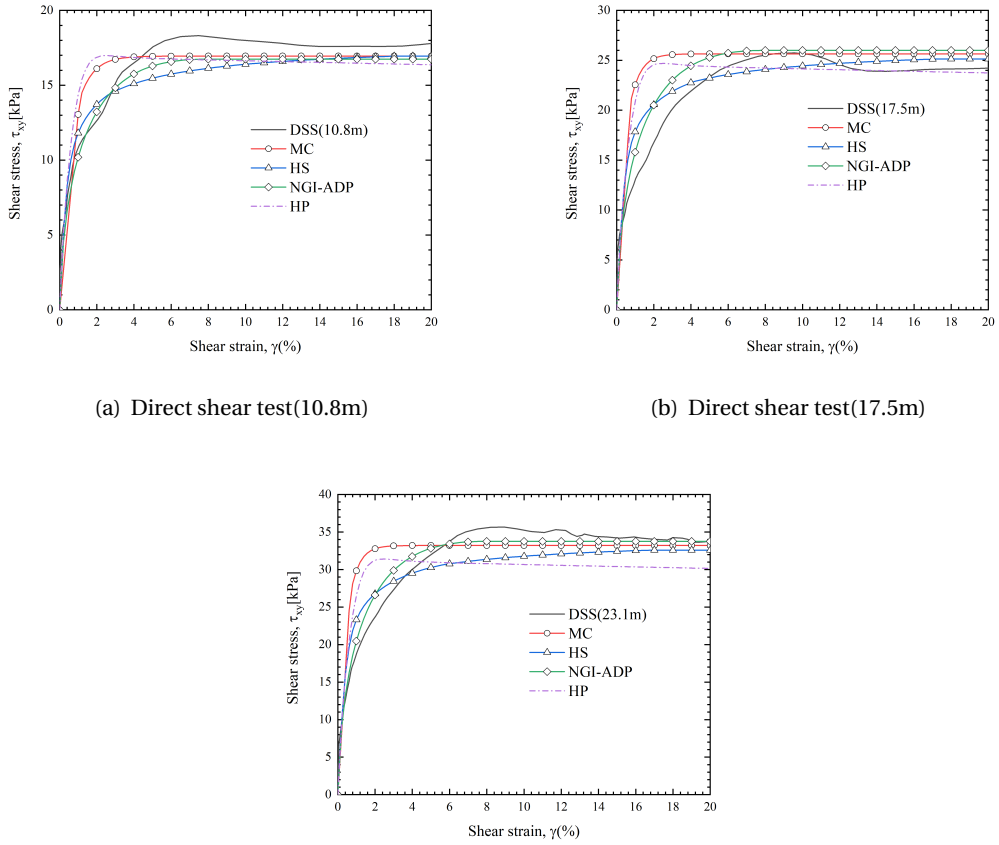


(a) Direct shear test(10.8m)

(b) Direct shear test(17.5m)

(c) Direct shear test(23.1m)

Figure 4.11: DSS test results and their prediction from PLAXIS

## 4.4. Summary

In previous sections, all the input parameters for different constitutive models have been calibrated basic on the soil interpretation(Chapter 3). The calibration process is robust for MC, HS, and NGI-ADP model; however, due to the oedometer data is not consistent, an error-and-trial method is used to calibrate the HP model. All of the models present the same level of soil strength. The advanced models(HS, NGI-ADP, and HP) predict the nonlinear stress-strain relationship of CAUc triaxial tests. In the DSS test, the NGI-ADP model beyonds the MC and HS model by including the anisotropic soil behavior. Thus, this model can present a more accurate stress-strain relationship. The HP model is capable of modeling a reasonable stress path(p-q curve) of the CAUc triaxial tests for this normally to lightly over-consolidated clay.

# 5

# FEM analysis

In this chapter a suction pile finite element model(FEM) is built up in Plaxis 3D (Brinkgreve R.B.J., 2018). The suction pile dimensions and properties are illustrated. Four loading cases are analyzed to make a compression between the use of different constitutive models.

## 5.1. Model Geometry

The aspect ratio(L/D) and the outer diameter of the suction pile are assumed to be 3 and 4m, respectively. The dimension of the suction pile is not really concerned in this project, since the main purpose is to compare the numerical result among different soil models. Table 5.1 gives all the input parameter for the suction pile in Plaxis 3D (Brinkgreve R.B.J., 2018). Making use of the symmetry of the geometry and the coplanar load system, so the half model of the suction pile foundation is represented. For the lateral FE model geometry, the model dimensions are set as possible as boundary effects are minimized. Width across the symmetry plane is ten times the OD(40m), while the height perpendicular to the symmetry plane is equal to the depth of the soil stratigraphy in Chapter 3(Fig 5.1). A zero-deformation normal boundary at -24mbsf. The same boundary is also applied to the rest of the boundaries except the upper z-boundary, which is unconstrained.

Table 5.1: Structural Parameters

| Parameter | Description | Caisson Shell | Top Plate | Units |
|---|---|---|---|---|
| Material type | - | Elastic | Elastic | [-] |
| d | Virtual Thichness | 0.030 | 0.032 | [m] |
| $\gamma$ | Unit Weight | 78.5 | 78.5 | [kN/m3] |
| E | Young's Modulus | 210E+06 | 210E+06 | [kN/m2] |
| $\nu$ | Poisson's Ratio | 0.2 | 0.2 | [-] |
| G | Shear Modulus | 87.5E+06 | 87.5E+06 | [kN/m2] |

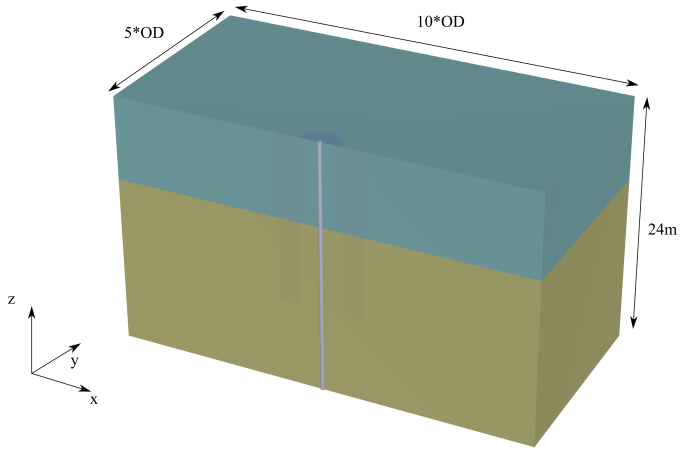


Figure 5.1: Overview of FE model

To model the soil-structure interaction accurately, interface elements have been created for the top plate and along with the shell(Figure 5.2). The interface strength for these elements is assumed in the order of 0.6($R_{inter} = 0.6$) since no detailed information can be obtained. In general, the interface is weaker and more flexible than the surrounding soil for real soil-structure interaction, which means that the value of $R_{inter}$ should be less than 1 as also recommended by Brinkgreve R.B.J. (2018).

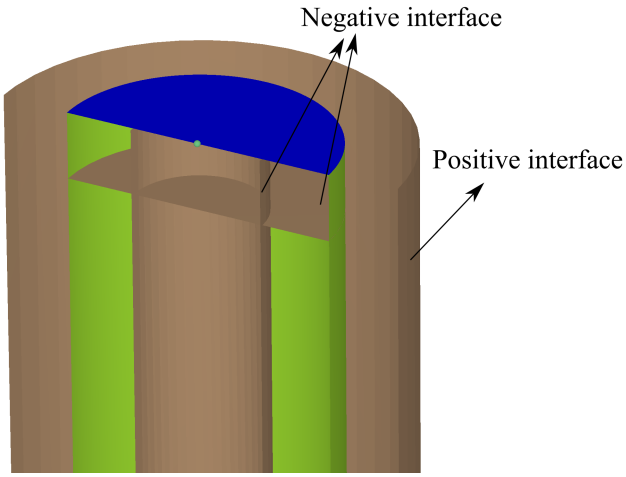


Figure 5.2: Interface element for suction pile

## 5.2. Boundary Check

In this section, the common procedure in FEM is carried out. The whole FEM model are explained in Section 5.1, the first step is checking the boundaries if they are placed far enough to not to alter the stress distribution. The deviatoric stress(q) and the mobilized shear strength $\tau_{mob}$ at the boundaries in the initial phase and the loading apply phase are compared(Table 5.2). It is clear that the deviatoric stress and mobilized shear strength barely alter, so the boundary is far enough for all the models.

Table 5.2: Boundary check

| Soil model | Deviatoric stress(q) | | | Mobilized shear strength($\tau_{mob}$) | | |
|---|---|---|---|---|---|---|
| | Initial phase | Loading phase | Difference | Initial phase | Loading phase | Difference |
| MC | 42kPa | 42.77kPa | 1.83% | 21kPa | 21.31kPa | 1.48% |
| HS | 42kPa | 42.17kPa | 0.40% | 21kPa | 21.11kPa | 0.52% |
| NGI | 42kPa | 42.3kPa | 0.71% | 21kPa | 21.2kPa | 0.95% |
| HP | 42kPa | 42.77kPa | 1.83% | 21kPa | 21.32kPa | 1.52% |

## 5.3. Deformation

Four assumptive loading cases are included to investigate the suction pile behavior when using different constitutive models. A pre-calculation is done by Caisson-VHM to ensure the assumptive loading does not exceed the capacity of the structure. The VH-envelops with different magnitude of the overturning moment are obtained (Figure 5.3). The maximum vertical load is about 3000kN, but the maximum horizontal load is depended on the applied overturning moment. When there is no overturning moment applied, the value of maximum horizontal load equaled to 1320kN.

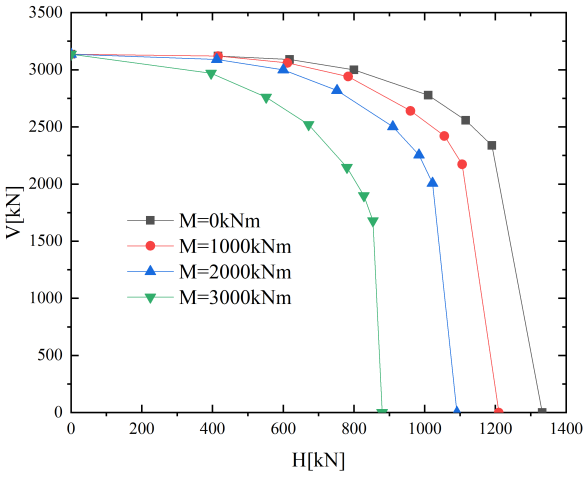


Figure 5.3: VH-envelop for suction pile (OD=4,L/D=3)

Four assumed loading cases were presenting the typical foundation type: Horizontal load presents mooring foundation, tension and compression load presents suction pile for jacket foundation, and V-H-M combing load represented mono bucket. Base on the VH-envelops, the magnitude of the four loading cases were shown in Table 5.3. All the forces and moments were added to the FEM in a straight-forward manner at the rigid body reference point(at mudline centre of the top plate). Due to the use of symmetry requires the applied loads to be halved, as they were applied to only half of the suction pile model. The reference point was also used to measured the displacement of the structure.

Table 5.3: Loading cases

| Loading cases | Vertical load V[kN] | Horizontal load H[kN] | Overturning moment M[kNm] |
|---|---|---|---|
| Case A | 0 | 600 | 0 |
| Case B | 1500 | 0 | 0 |
| Case C | -800 | 0 | 0 |
| Case D | 1500 | 200 | 2000 |

There are three types of undrained analysis types which have been explained in section 4.1in PLAXIS 3D. For deformation analysis, undrained (A) is adopted for Mohr-Coulomb, hardening soil and hypoplastic models. As for NGI-ADP model, undrained (C) is the only option for it.

### 5.3.1. Case A(horizontal load)

As shown in Figure 5.4, when the suction pile subjected to horizontal load, the NGI-ADP model obtained the largest deformation, about 0.060m, followed by a slightly smaller value of 0.052m from the MC model. The deformation of HS and HP model is relatively low, with the value of 0.039m and 0.030m respectively. Even though the NGI-ADP model resulted a highest deformation among all models, this model shows a similar high stiffness as HP and HS models at the small strain stage(Total deformation $|u| < 0.01m$). The stiffness of the suction pile foundation decreases significantly in the NGI-ADP model.

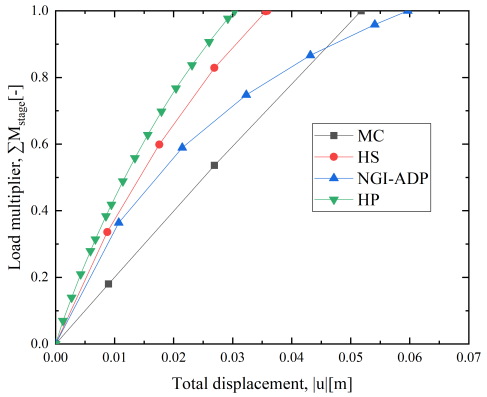


Figure 5.4: Structure behavior under horizontal load when using different constitutive models

Further analysis of the soil behavior for different constitutive models is carried out. Figure 5.5 compared the deviatoric strain $\gamma_s$ development in different constitutive models. From the graphs below, we can see that MC, HS, and NGI-ADP models have a similar deviatoric strain $\gamma_s$ development zone. The NGI-ADP model gives the highest maximum deviatoric strain with 0.11. MC and HS models result in a relatively lower maximum deviatoric strain with 0.07 and 0.04, respectively. However, the hypoplastic model shows a different deviatoric strain development zone and obtains the lowest maximum deviatoric strain of about 0.02. Unlike the other models, the deviatoric strain mainly expands in the passive zone. It can barely find deviatoric stress develop in the active zone and bottom tip of the suction pile.

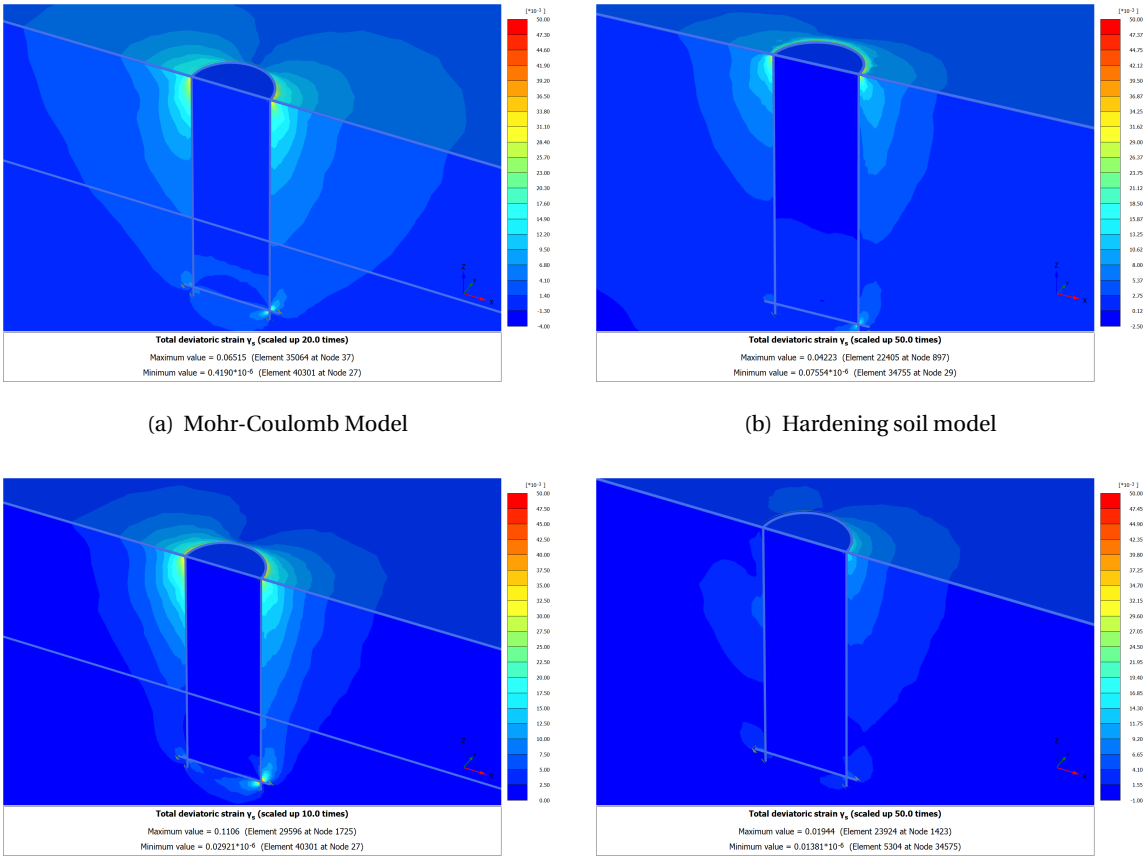


(a) Mohr-Coulomb Model

(b) Hardening soil model

(c) NGI-ADP model

(d) Hypoplastic model

Figure 5.5: Total deviatoric strain under horizontal load

If we are now looking at the horizontal displacement(Figure 5.6), the deformation of soil is more prominent. In MC, HS, and NGI-ADP model, the soil around the upper part of the structure moves together with the suction pile. On the other hand, in the hypoplastic model, the soil in the upper active zone almost remains original. The NGI-ADP model presents the highest horizontal displacement of 0.060m in Case A, followed by the MC model with a slightly smaller value of about 0.056m. The HS model and HP model result in relatively small values of 0.036m and 0.030m, respectively.

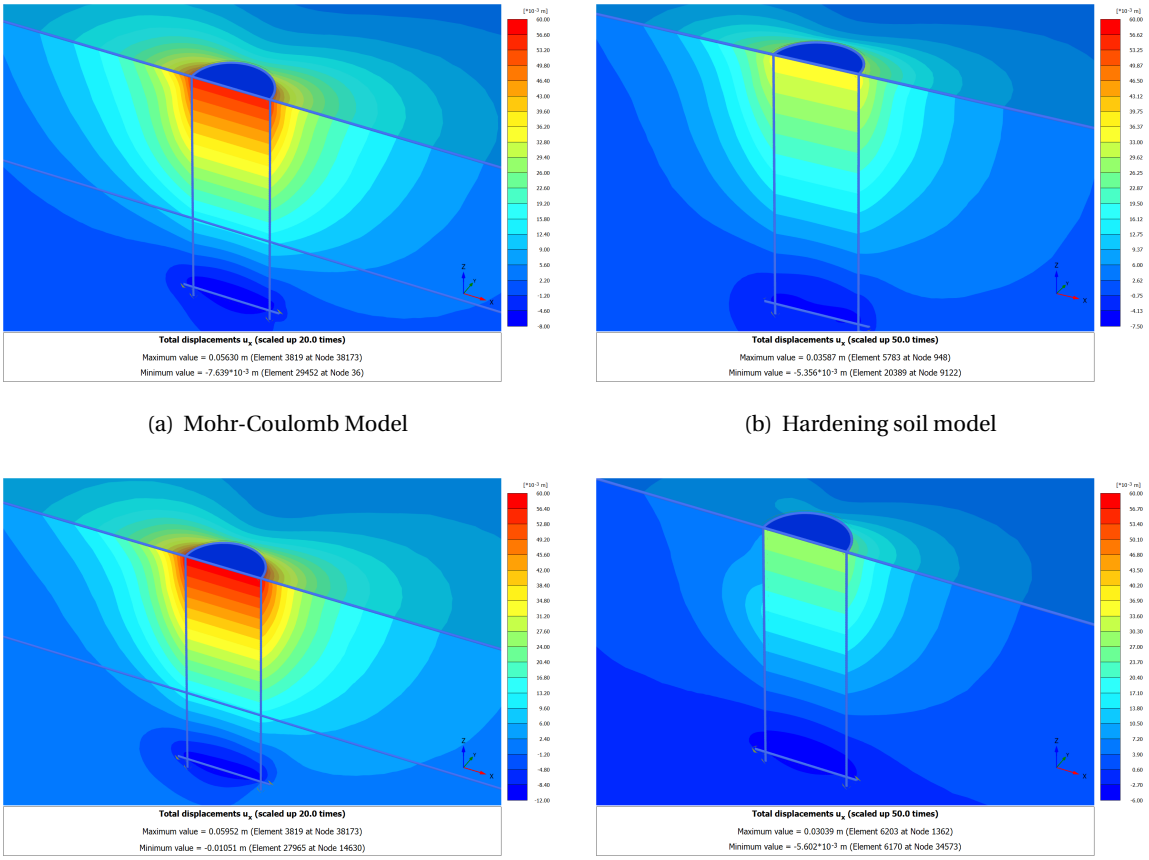


(a) Mohr-Coulomb Model

(b) Hardening soil model

(c) NGI-ADP model

(d) Hypoplastic model

Figure 5.6: Horizontal displacement under horizontal load

### 5.3.2. Case B(Tension)

In this case, the suction pile is subjected to a vertical pull-out force. Figure 5.7 illustrates the relationship of total displacement versus the load multiplier. The MC model obtains the largest total displacement with 0.022m. The NGI-ADP model, on the contract, results in the lowest total displacement with 0.013m. The HS and HP models generate the intermediate values about 0.015m and 0.021m, respectively. For this case, the NIG-ADP model presents the highest stiffness initially even though it drops markedly as the increasing loading.

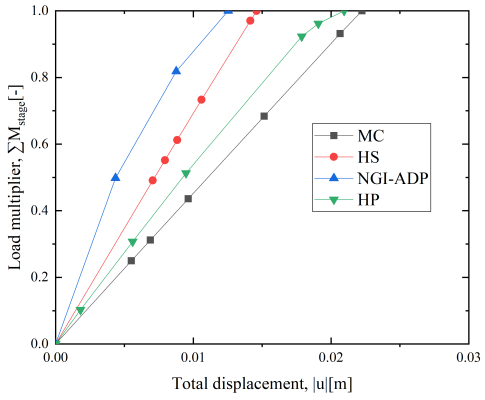


Figure 5.7: Structure behavior under vertical tension load when using different constitutive models

Figure 5.8 presents the comparison of deviatoric strain for different constitutive models subjected to vertical tension force. The maximum values of the deviatoric strain are quite close among all the models; the HP model obtains the highest value of 0.014 at the bottom tips of the suction pile shell. Followed by the HS model in which the maximum deviatoric strains is about 0.012 happened at the top tips of the suction pile shell for the HS. A similar deviatoric strain development zone is presented in the MC and NGI-ADP models: the deviatoric strain reaches the maximum value of about 0.012 at the top and bottom tips of the suction pile shell and decreases along the length and radius.

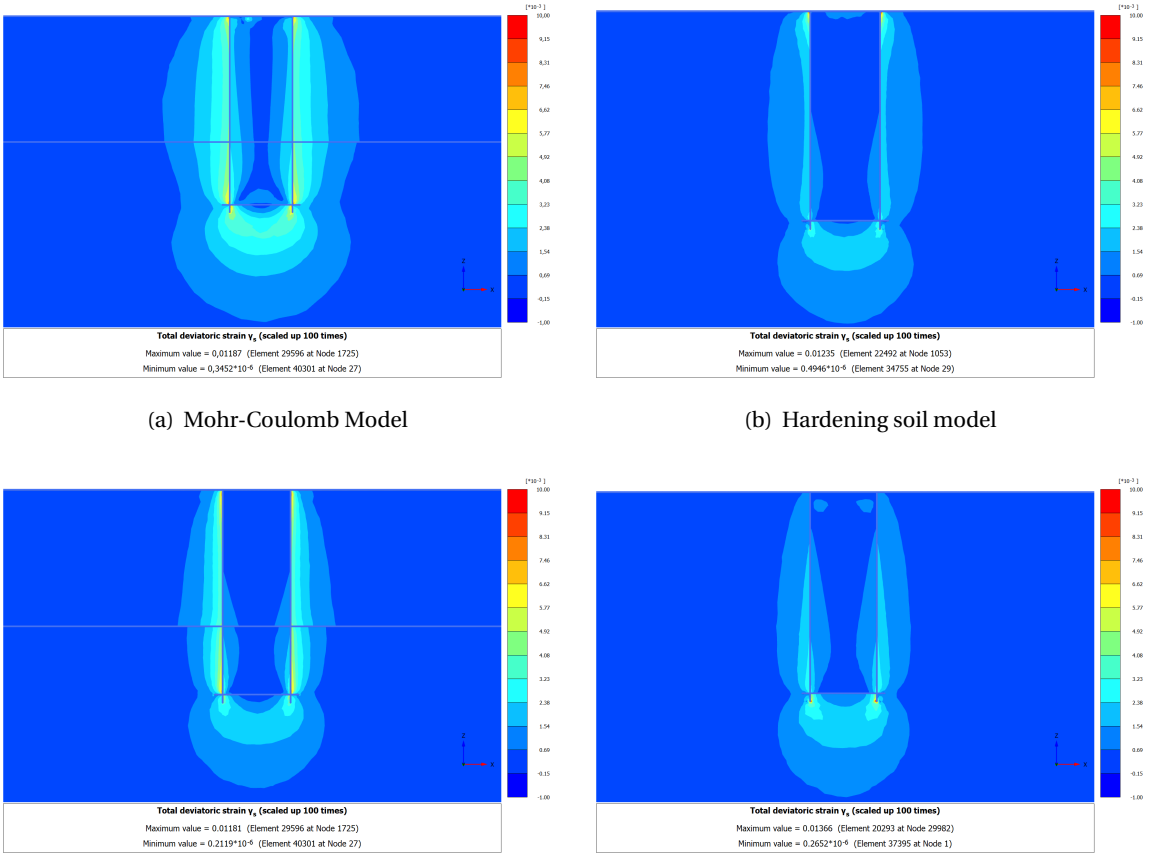


(a) Mohr-Coulomb Model

(b) Hardening soil model

(c) NGI-ADP model

(d) Hypoplastic model

Figure 5.8: Total deviatoric strain under horizontal load

The vertical deformation of the soil domain, as illustrated in Figure 5.9. It is clear that the insider soil moves with the suction pile, and the displacement decreases with the increasing distance between the soil and structure in all models. However, for the HP model, the soil in the vicinity of the top-plate center deforms less than the soil around. The highest vertical total displacement is obtained in the MC model, about 0.021m. The HP model results in a lower value of 0.015m, and a close number of about 0.014m is found in the HS model. The total vertical displacement is lowest in the NGI-ADP model of 0.012m.

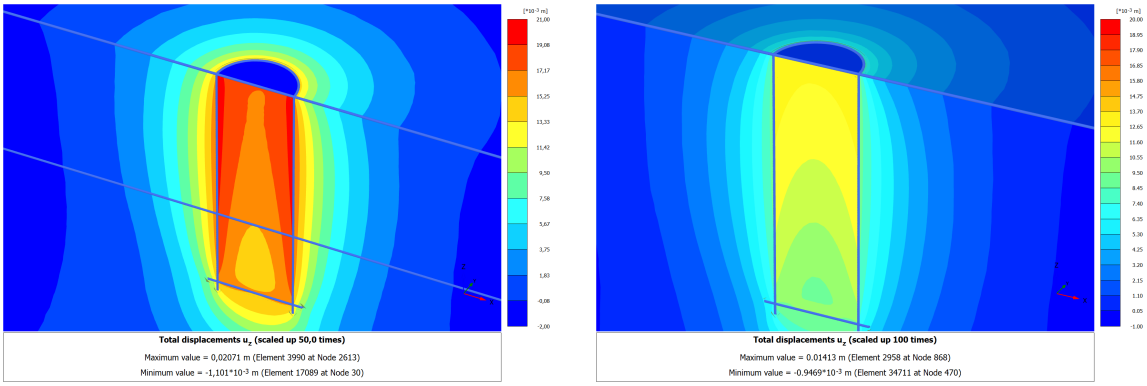


(a) Mohr-Coulomb Model (b) Hardening soil model

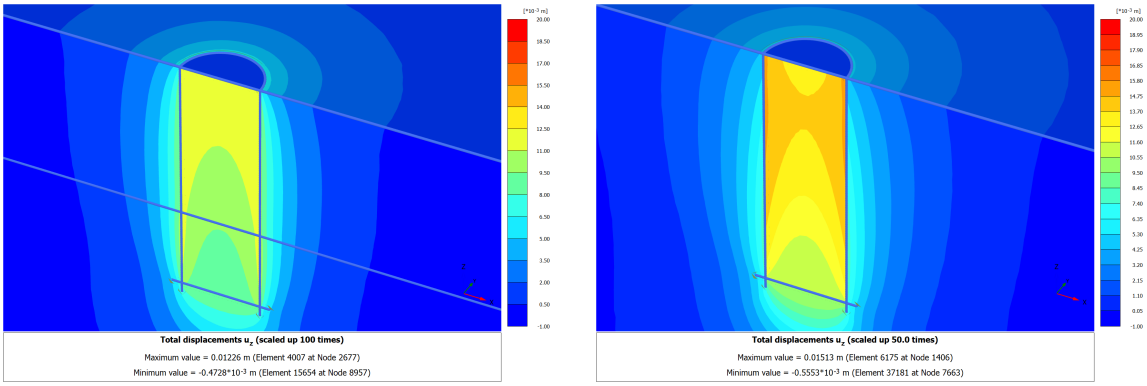


(c) NGI-ADP model (d) Hypoplastic model

Figure 5.9: Vertical displacement under tension load

### 5.3.3. Case C(Compression)

In this case, the suction pile is subjected to a vertical compression load equal to 800kN. The stiffness of the suction pile foundation is close in different constitutive models for low loading range ($|V| < 400kN$). HS model obtains the lowest total displacement of 0.012 among all the models. NGI-ADP model has the highest stiffness at the beginning of the calculation, with a mild reduction in the load's development. For the HP model, the initial stiffness is almost the same as the HS model, and then a sharp drop happens when the load increased, and the structure reachs the highest total displacement, about 0.021m.

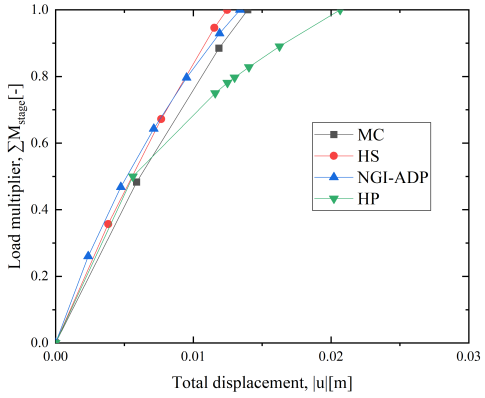


Figure 5.10: Structure behavior under vertical compression load when using different constitutive models

The comparison of the development of deviatoric strains plotted in Figure 5.11. The largest total deviatoric strains are found in the NGI-ADP model with the maximum value of 0.031 around the suction pile's top and bottom. For MC, HS, and NGI-ADP models, the similar deviatoric strains develop zone as the pull-out load was formed. For the HP model, the evolution of deviatoric strains mainly happened at the bottom of the suction pile with a maximum value of 0.024. The MC and HS model had relatively low deviatoric strains of 0.017 and 0.019, respectively.

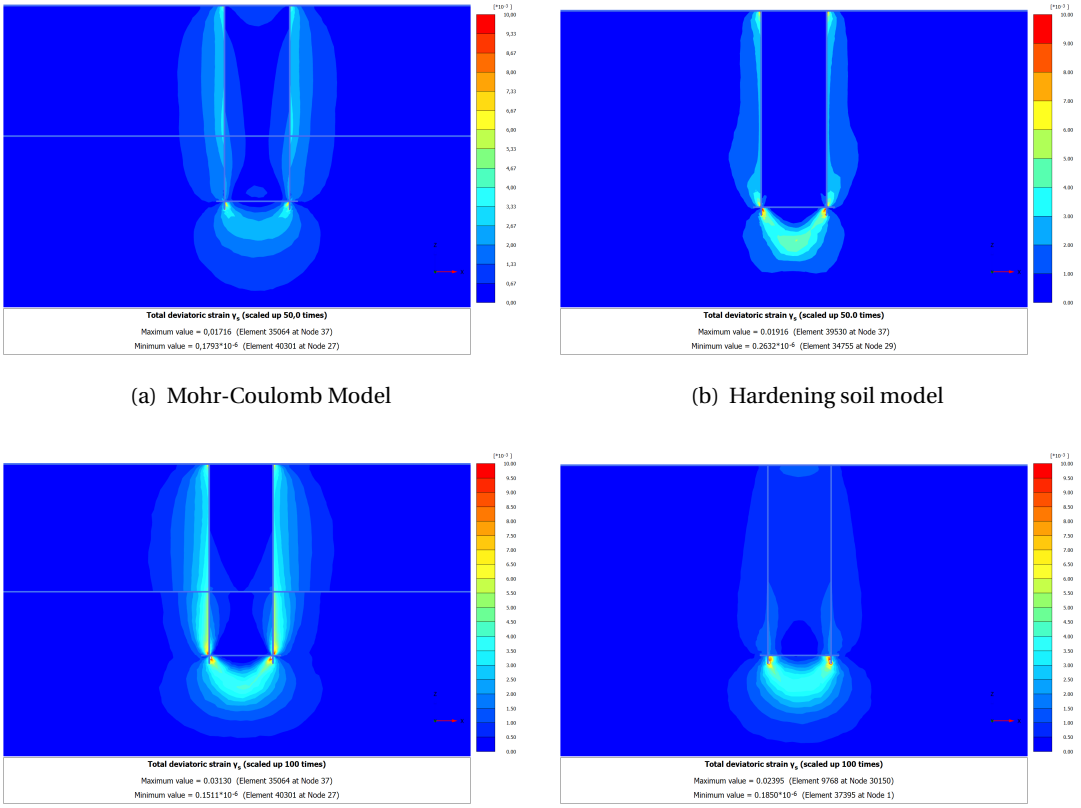


(a) Mohr-Coulomb Model

(b) Hardening soil model

(c) NGI-ADP model

(d) Hypoplastic model

Figure 5.11: Total deviatoric strain under compression load

Turning now to the soil deformations in different constitutive models (Figure 5.12). The insider soil is pushed down by the load, and the displacement decreases along with the depth. The soil out-

side of the suction pile deforms less than the insider domain. In MC, HS, and the NGI-ADP model, the soil outside of the suction pile has a similar deformation zone with the same displacement level. The smallest maximum vertical displacement is found in the HS model, about 0.012m, follows by the MC model and NGI-ADP models with a value of about 0.013m. However, even though the highest maximum vertical displacement is obtained in the HP model, the soil outside of the suction pile hardly moves with the suction pile.

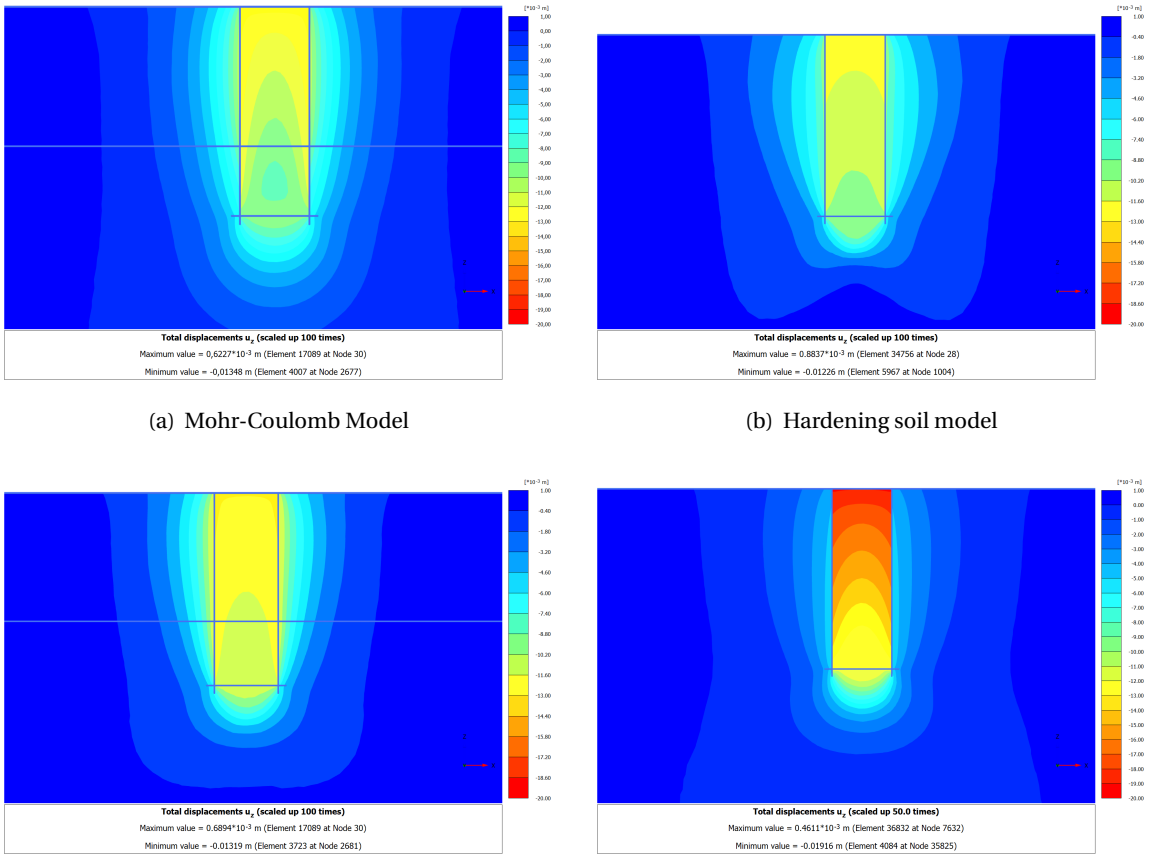


(a) Mohr-Coulomb Model

(b) Hardening soil model

(c) NGI-ADP model

(d) Hypoplastic model

Figure 5.12: Vertical displacement under compression load

### 5.3.4. Case D(VHM-combining)

In the last case, the combined load of vertical, horizontal, and overturning moment is applied to the structure at the reference point. The relationship between total displacement and load multiplier is illustrated in Figure 5.13. The largest total displacement is obtained in the MC model, about 0.043m. A slightly lower value of about 0.041m is found in the NGI-ADP model. The suction pile had the highest stiffness when the external force is less than 50% in the NGI-ADP model, and then a remarkable decrease arose with the increase of the loading. The HP and HS model result in a rather lower value of 0.032m and 0.027m, respectively.

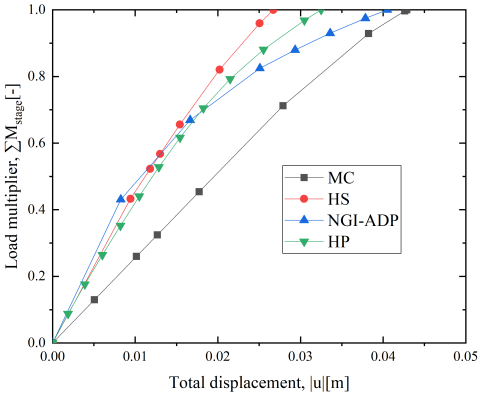


Figure 5.13: Structure behavior under VHM combing load when using different constitutive models

The final deviatoric strains of different FEM models are plotted in Figure 5.14. The highest maximum deviatoric strain of 0.058 is found in the HS model in which the total displacement is the smallest among the models. A little be lower value of about 0.056 is obtained in the NGI-ADP model. The MC model, whose total displacement is the largest, presenting a relatively low value of about 0.038. The HP model develops the lowest deviatoric strain, almost 0.024. A similar phenomenon as Case A is observed that the MC, HS, and NGI-ADP models result in a similar deviatoric strain development zone. On the contrary, the deviatoric strain mainly grows in the passive zone.

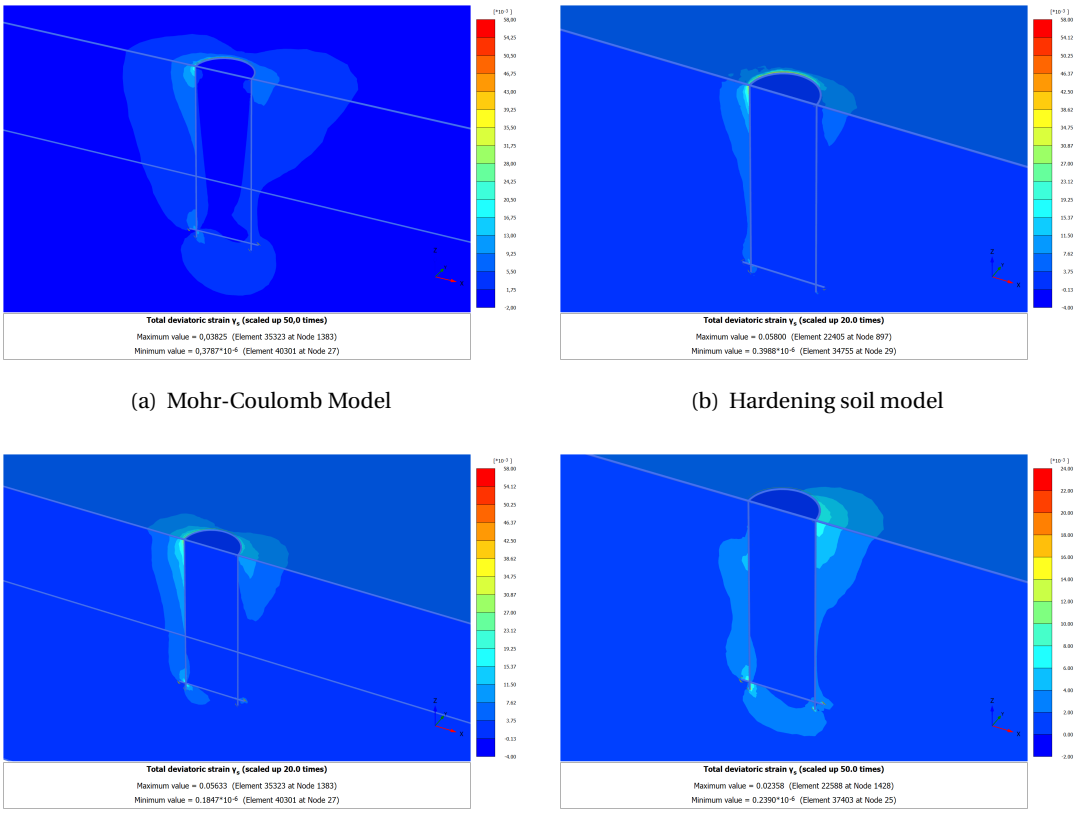


(a) Mohr-Coulomb Model

(b) Hardening soil model

(c) NGI-ADP model

(d) Hypoplastic model

Figure 5.14: Total deviatoric strain under VHM-combining load

If we now turn to the contrast of total displacement between different models (Figure 5.15). The

maximum total displacement of the soil is found at the top tip inside the suction pile for all the models. The soil deformation behaviour is reasonably similar in the MC, HS, and NGI-ADP models. Like the suction pile displacement, the highest maximum total displacement of the soil domain is observed in the MC model, about 0.046m. A little bit smaller value of 0.044m is obtained in the NGI-ADP model. The maximum total displacements for the HP and HS model are 0.032m and 0.029m, respectively.

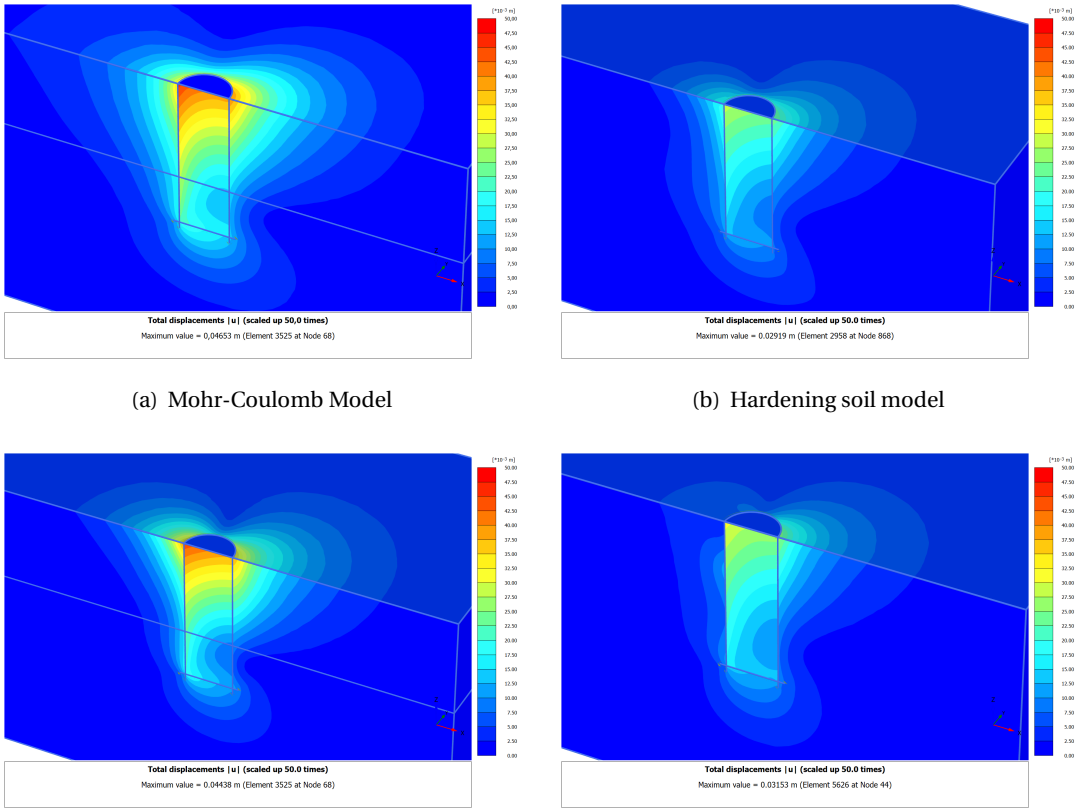


(a) Mohr-Coulomb Model

(b) Hardening soil model

(c) NGI-ADP model

(d) Hypoplastic model

Figure 5.15: Total displacement under VHM-combining load

## 5.4. Capacity

The capacity analysis is performed with the same loading cases for deformation analysis(Table 5.3). The safety calculation is an option available in PLAXIS 3D to compute the global safety factors. In this approach, the structure capacity is generally evaluated by reducing the shear strength parameters $tan\phi$ and $c$ of the soil(MC model), and it is expressed by the so-called factor of safety(FoS). The strength parameters are continuously reduced by increasing FOS until certain steps are reached. If a fully developed failure mechanism has been resulted in the final step, the FOS is given by:

$$FoS = \frac{available strength}{strength at failure} = value of \sum M_{sf} at failure \tag{5.1}$$

In PLAXIS, the strength reduction method, combined with the hypoplastic model, has not yet been developed. In this section, the safety analysis is carried out using the MC, HS, and NGI-ADP model. Before examining the structure capacity, the available shear strength given from the models is inspected and compared with the undrained shear strength give from the available laboratory tests from samples consolidated with in situ stresses. In the output program, the maximum value of shear stress for the whole soil layers is plotted Figure C.1. Considering the soil layer is uniform horizontally,

the $s_u$ profile between different constitutive models and the design is plotted in Figure 5.16. The $S_u$ design profile is from the DSS test results in Table 3.3. The MC and HS models obtain the almost same $s_u$ profile as the design one. However, NGI-ADP and MC(B) models presented a little low value for shallow layers and a slightly high value for deep layers.

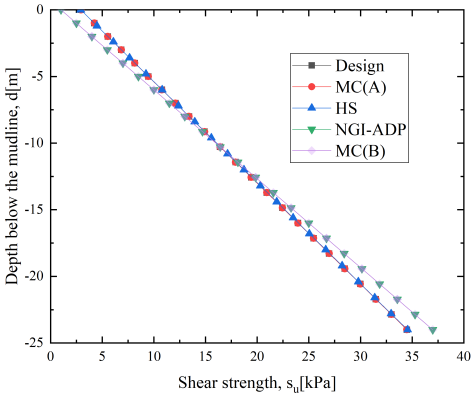


Figure 5.16: $S_u$ profile from soil report and different constitutive models

The capacity analysis results, the factor of safety versus total displacement of reference point, were plotted in Figure 5.17 for all the cases. The fully developed failure mechanism resulted in all suction pile models except for the HS model in case C. The highest values of FoS for different models and cases were summarised in Figure 5.18. It can be seen from the data in the bar chart (Figure 5.18) that the MC(A) model obtains the highest FOS among all the models in every case. The HS model presented a slightly lower value than the MC model except for case C's non-convergent result, in which a considerable decrease was found.On the contrary, the NGI-ADP model achieved the lowest FoS among all models in every case. Since the Undrained(A) analysis was applied in MC and HS models, the MC model with Undrained (B) analysis was also included to investigate the effect of different undrained analysis. Even though the MC(B) model presented the same shear strength profile as the NGI-ADP model, the FoS obtained from MC(B) models still was noticeably higher than the NGI-ADP models.

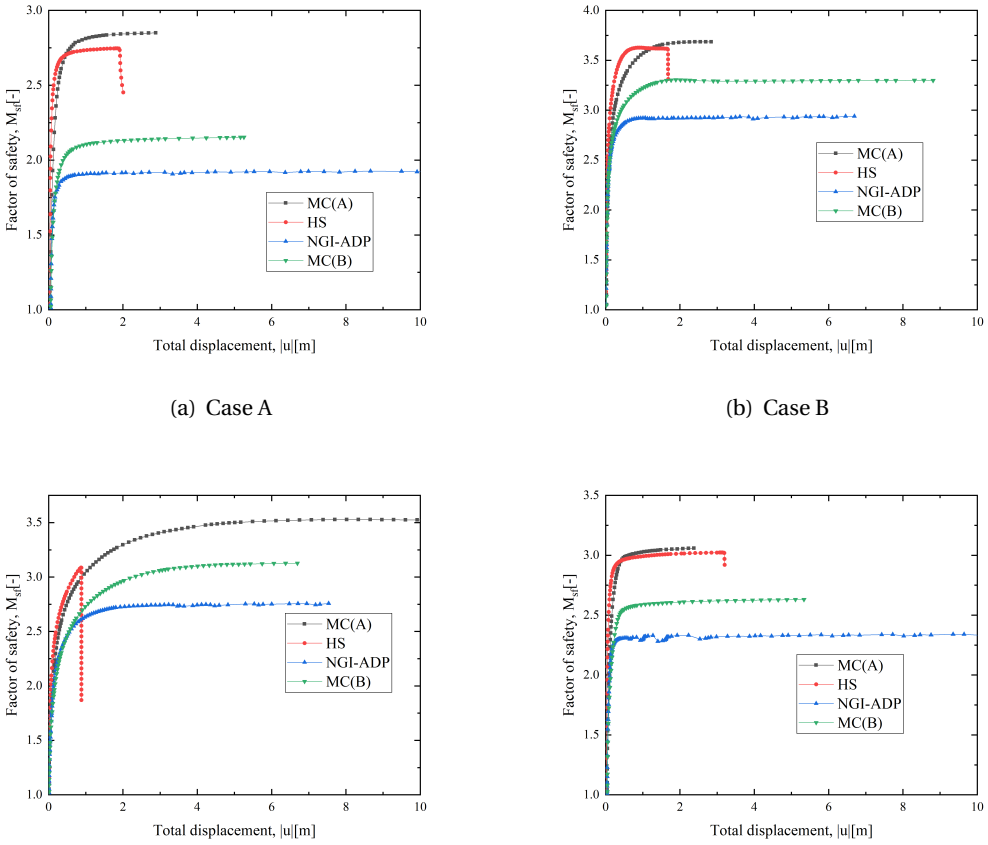


(a) Case A

(b) Case B

(c) Case C

(d) Case D

Figure 5.17: Factor of safety versus total displacement

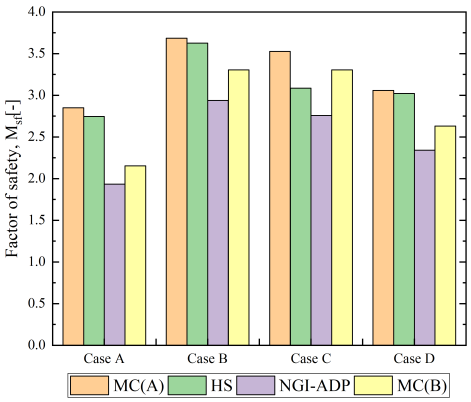


Figure 5.18: Safety analysis results

From the above plots, the first interesting finding is the FoS obtained from Undrained(A) analysis is generally higher than the one from Undrained(C) or Undrained(B) analysis. There are mainly two results: Firstly, there are differences in the shear strength profile for undrained analysis(Figure 5.16). Especially, the shear strength of total strength analysis(undrained(B) and Undrained(C)) is lower than that of effective strength analysis(Undrained(A)) in the upper soil layer where the suction pile is installed. Secondly, in Undrained (A) analysis, the shear strength is not reduced by the same factor

whose value is equal to FoS. Comparing the shear strength profile for different constitutive models when the FoS is equivalent to 2.34 plotted in Figure 5.19. Combining Figure 5.16 and 5.19, the shear strength in total strength analysis is decreased by the FoS of 2.34. However, in the effective strength analysis, the shear strength was decreased by a little lower value than FoS. In other words, the reduction factor of shear strength in Undrained (B) and (C) is higher than that in Undrained (A). Since in total strength analysis, the shear strength is an input parameter, so the shear strength is directly reduced by the FoS follows Equation 5.2. By contrast, the shear strength is the result of effective strength parameter and stress states, as discussed in section 4.1, the effective parameters are reduced follows Equation 5.3.

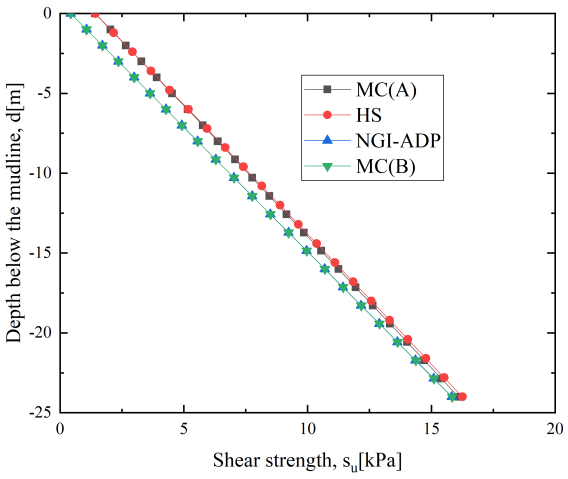


Figure 5.19: Reduced $S_u$ profile from different constitutive models

$$s_{u,reduced} = \frac{s_{u,input}}{FoS(\sum M_{sf})} \tag{5.2}$$

$$\tan\varphi_{reduced} = \frac{\tan\varphi_{input}}{FoS(\sum M_{sf})} \tag{5.3a}$$

$$c_{reduced} = \frac{c_{input}}{FoS(\sum M_{sf})} \tag{5.3b}$$

## 5.5. Compliance Matrix

The main idea of this section is to obtain the Compliance matrix of the suction pile for different constitutive models. Considering the symmetry of the suction pile, the compliance matrix for structure engineers can be derived as Equation 5.4. The elementary loading(i.e. pure transnational forces $F_X$ and $F_Z$ and pure bending moments $M_Y$) is applied to the suction pile to obtain the compliance matrix. The coefficients in the compliance matrix are calculated by Equation 5.5. The effect of vertical force on rotation and horizontal displacement is negligible so $C_{13} = C_{23} = 0$.From the deformation analysis (Section 5.3), the stiffness would be degraded as the loading increases. Especially for the NGI-ADP model subjected to horizontal loading and HP model subjects to vertical loading. The input loads for this section are considered about 20% of the maximum capacity obtained from the section

5.4.

$$\begin{Bmatrix} U_X \\ \theta_Y \\ U_Z \end{Bmatrix} = \begin{bmatrix} C_{11} & C_{12} & C_{13} \\ C_{21} & C_{22} & C_{23} \\ C_{31} & C_{32} & C_{33} \end{bmatrix} \begin{Bmatrix} F_X \\ M_Y \\ F_Z \end{Bmatrix} \tag{5.4}$$

$$For\,(F_X, M_Y, F_Z) = (F_X, 0, 0) \begin{cases} C_{11} = U_X(F_X, 0, 0)/F_X \\ C_{21} = \theta_Y(F_X, 0, 0)/F_X \\ C_{31} = U_Z(F_X, 0, 0)/F_X \end{cases} \tag{5.5a}$$

$$For\,(F_X, M_Y, F_Z) = (0, M_Y, 0) \begin{cases} C_{12} = U_X(0, M_Y, 0)/M_Y \\ C_{22} = \theta_Y(0, M_Y, 0)/M_Y \\ C_{32} = U_Z(0, M_Y, 0)/M_Y \end{cases} \tag{5.5b}$$

$$For\,(F_X, M_Y, F_Z) = (0, 0, F_Z) \begin{cases} C_{13} = U_X(0, 0, F_Z)/F_Z \\ C_{23} = \theta_Y(0, 0, F_Z)/F_Z \\ C_{33} = U_Z(0, 0, F_Z)/F_Z \end{cases} \tag{5.5c}$$

There are 5 unknown coefficient to be calculated. For coefficient $c_{11}$, the horizontal displacement versus horizontal force is plotted in Figure 5.20(a). For coefficient $c_{12}$, the relationship of horizontal displacement and bending moment is plotted in Figure 5.20(b).For coefficient $c_{21}$, the relationship of rotation angle and horizontal force is plotted in Figure 5.20(c). For coefficient $c_{22}$, the rotation-moment curve is plotted in figure 5.20(d). The vertical displacement versus vertical force is plotted for the last coefficient $c_{33}$(Figure 5.20(e)). From the plots below, comparing with MC model, we can see that the advance models (i.e. HS, NGI-ADP and HP model) have close suction pile stiffness for small loading stage.

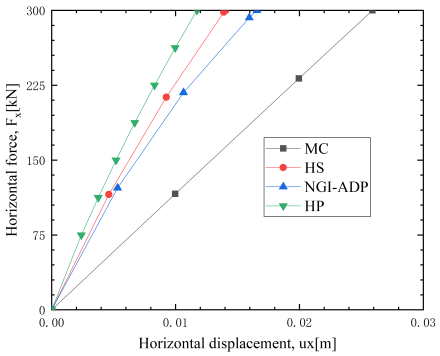


(a) Horizontal force versus horizontal displacement

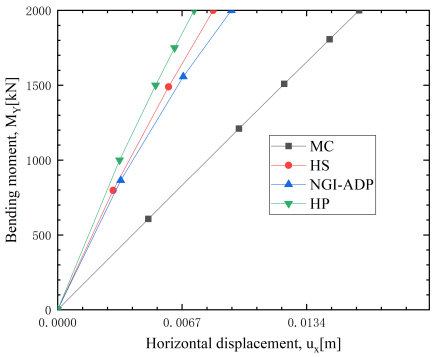


(b) Bending moment versus horizontal displacement

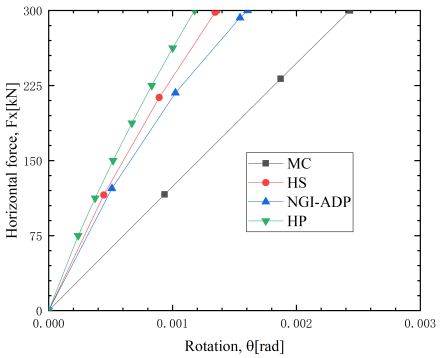


(c) Horizontal force versus rotation angle

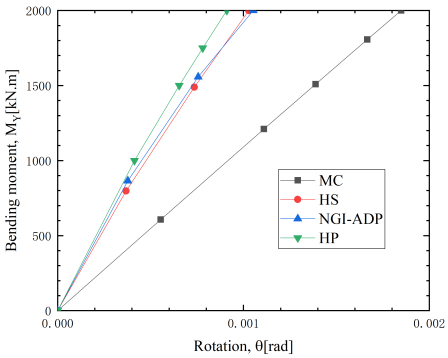


(d) Bending moment versus rotation angle

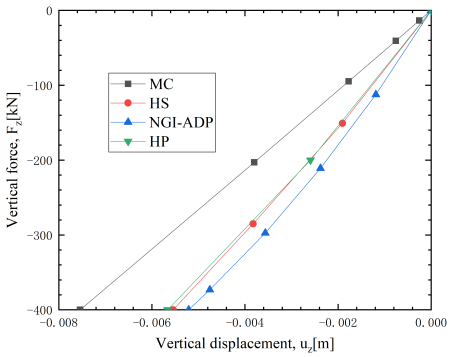


(e) Vertical force versus vertical displacement

Figure 5.20: External force versus Generalized displacement

Following equation 5.5 and combining the Figure 5.20, the compliance matrices for different constitutive models are derived. The compliance matrix for MC model is symmetrical due to it is a linear model. However, the asymmetry matrices are derived for the rest of the models.

The compliance matrix for MC model:

$$\begin{Bmatrix} U_X \\ \theta_Y \\ U_Z \end{Bmatrix} = \begin{bmatrix} 8.63E-05 & 8.11E-06 & 0 \\ 8.11E-06 & 9.25E-07 & 0 \\ 0 & 0 & 1.89E-05 \end{bmatrix} \begin{Bmatrix} F_X \\ M_Y \\ F_Z \end{Bmatrix} \tag{5.6}$$

The compliance matrix for HS model:

$$\begin{Bmatrix} U_X \\ \theta_Y \\ U_Z \end{Bmatrix} = \begin{bmatrix} 4.69E-05 & 4.19E-06 & 0 \\ 4.53E-06 & 5.14E-07 & 0 \\ 0 & 0 & 1.39E-05 \end{bmatrix} \begin{Bmatrix} F_X \\ M_Y \\ F_Z \end{Bmatrix} \tag{5.7}$$

The compliance matrix for NGI-ADP model:

$$\begin{Bmatrix} U_X \\ \theta_Y \\ U_Z \end{Bmatrix} = \begin{bmatrix} 5.53E-05 & 4.68E-06 & 0 \\ 5.35E-06 & 5.26E-07 & 0 \\ 0 & 0 & 1.3E-05 \end{bmatrix} \begin{Bmatrix} F_X \\ M_Y \\ F_Z \end{Bmatrix} \tag{5.8}$$

The compliance matrix for HP model:

$$\begin{Bmatrix} U_X \\ \theta_Y \\ U_Z \end{Bmatrix} = \begin{bmatrix} 3.91E-05 & 3.67E-06 & 0 \\ 3.93E-06 & 4.55E-07 & 0 \\ 0 & 0 & 1.42E-05 \end{bmatrix} \begin{Bmatrix} F_X \\ M_Y \\ F_Z \end{Bmatrix} \tag{5.9}$$

## 5.6. Summary

In this chapter, the performance of the suction pile is analysis by using PLAXIS 3D with different constitutive models. Beginning with deformation analysis of four loading cases in this section 5.3, and all the constitutive models are used in the analysis. The additional output results $\tau_{rel}$ from the output program of PLAXIS 3D are discuss in appendix B. Regardless of the constitutive model, the stiffness of the suction pile foundation decreases with the increase of the loading. However, comparing with advanced constitutive models(i.e. NGI-ADP and HP models), the degradation of the foundation stiffness is minute in MC and HS models. It could be concluded from the analysis, stiffness of the suction pile would significantly decrease when subjected to horizontal or VHM combine load in the NGI-ADP model. There is a noticeable reduction in the stiffness when the vertical compression load was applied on the suction pile for the hypoplastic model. However, the rest of the models show similar behaviour for vertical compression case.

In section 5.4, the capacity analysis is carried out for all the constitutive models except for hypoplastic model. The factor of safety is obtained for different models. The most interesting finding is the FoS of total strength analysis(i.e. NGI-ADP and MC(B) models) lower than that from effective strength analysis(i.e. MC(A) and HS model) for all the cases. This result is accordant with the conclusion from Tschuchnigg et al. (2015). Additionally, the more conservative value of FoS is achieved for the NGI-ADP model.

In section 5.5, the compliance matrices for the suction pile are obtained for different constitutive models. It can be conclude that the suction pile performance in small load stage are closed when modeled by the advanced models (i.e. HS, NGI-ADP and HP model). And the compliance matrices are asymmetry for the these models.

# 6

# Conclusions and Recommendations

The present study was focused on the compassion of four different constitutive models. The input parameters for the soil models were calibrated based on real soil data, and the calibration process was detailed explained. The numerical laboratory experiments were performed and compared with the real test data. A suction pile with the outer diameter equal to 4m and the aspect ratio equal to 3 was built in different soil models. The deformation, capacity and compliance matrix analyses are performed.

## 6.1. Conclusions

With regard to the three main objectives of this numerical study, namely:

1. Comparing the required data and calibration process among different constitutive models.
2. To analyze the soil element behavior of different constitutive models.
3. To compare the suction pile performance when using the different constitutive models.

the following could be concluded:

- The in-situ tests were needed to have an overview of the soil layers. The CAUc triaxial tests were essential for the calibration of all the constitutive models. Additionally, CAUe triaxial tests and DSS tests were recommended to include for the anisotropic soil behavior. The oedometer tests were needed for the HS and HP models. The NGI-ADP model had a relatively robust calibration process among all the models.
- The advanced constitutive models(i.e. HS, NGI-ADP and HP models) excess the MC model by including the non-linear behavior. The HS model included the stress depended stiffness. The anisotropic soil behavior was well predicted by the NGI-ADP model. The HP model could present a good fit for the stress-path.
- In all the loading cases, the suction pile displacement increased steadily with the climbing load in the MC and HS models.
- In horizontal and VHM-combining load cases, the NGI-ADP model had a remarkable stiffness reduction. Additionally, the deformation and deviatoric strain development were distinct in the HP model.
- The increment of suction pile displacement was relatively large in the HP model for vertical compression loading.

- The safety analysis was not implemented for the hypoplastic model in PLAXIS 3D yet. The MC and HS models obtained higher FoS, and a comparably low value resulted in the NGI-ADP model. There were mainly three reasons for this: Firstly, as discussed in section 4.3, the MC and HS overestimate the stiffness and strength of the soil in DSS tests. Secondly, due to the Undrained (A) analysis in the MC and HS model, the reduced shear strength is higher than that of the NGI-ADP model in the safety analysis. The last reason was the different shear strength profile(Unreduced) between the NGI-ADP model and MC(or HS) model.

Combine the above conclusions, the NGI-ADP model is an applicable model for engineering application. The calibration process is robust, and the required data are from common laboratory tests (i.e. triaxial tests and direct shear tests). When modelling the suction pile, the NGI-ADP model presents the relatively consistent result as the hardening soil model and hypoplastic model for compliance matrix. The conservative results are obtained for all capacity analyses and for most of deformation analyses. The hypoplastic model, this model was not well calibrated in this study as only the CAUc triaxial test data was included. Even though it can present a good fit for stress path for CAUc triaxial test, the soil behaviour around the suction pile could be wrongly calculated by PLAXIS 3D. The possible reason for that is different set of input parameters can predict the same CAUc triaxial tests data.

## 6.2. Recommendations

The present work mainly focused on a homogeneous clay layer and a single size of the suction pile. Therefore some issues that need to be addressed for future studies may be as follows:

- The present test data were enough for calibrate mohr-coulomb, hardening soil and NGI-ADP model. The static performance for the suction pile could be well analyzed by these models.
- It was recommended to consider a sandy layer. A different value for stiffness and strength parameters would be calibrated, and the soil behavior would change also.
- The calibration process of the hypoplastic model could be more reliable with more consistent soil data. The soil behaviour maybe better modelled by this model when using the well calibrated input parameters.
- Different sizes of suction piles and loading cases should be further investigated.
- It was recommended to model a real suction pile foundation model with different constitutive models and investigated the FEM's accuracy by comparing them with the real data.

# Reference List


Andersen, K., J.D. Murff, and M.F. Randolph (2015). Suction anchors for deepwater applications. *Rammed Earth Construction*, 5(June):1–1.

Aubeny, C. P., Han, S. W., and Murff, J. D. (2003). Inclined load capacity of suction caissons. *International Journal for Numerical and Analytical Methods in Geomechanics*, 27(14):1235–1254.

Barari, A. and Ibsen, L. B. (2011). Effect of Embedment on the Vertical Bearing Capacity of Bucket Foundations in Clay. *2011 Pan-Am CGS Geotechnical Conference*, (1999):197–198.

Barari, A. and Ibsen, L. B. (2012). Undrained response of bucket foundations to moment loading. *Applied Ocean Research*, 36:12–21.

Bransby, M. F. and Randolph, M. F. (1998). Combined loading of skirted foundations. *Geotechnique*, 48(5):637–655.

Brinch Hansen, J. (1970). A Revised and Extended Formula for Bearing Capacity. *Bulletin of the Danish Geotechnical Institute*, 28(28):5–11.

Brinkgreve R.B.J., Kumerswamy S., S. W. (2018). Material Models Manual. *Plaxis*, 1.

Budiaman, I., Soedigdo, I., and Prakoso, W. A. (2015). Analysis of Suction Piles for Mooring Floating Structure. *International Journal of Technology*, 2(April):254–263.

Cathie, D., Irvine, J., Houlsby, G., Byrne, B., Buykx, S., Dekker, M., Jansen, E., Dijkstra, O., Schuhmacher, T., and Morgan, N. (2019). Suction Installed Caisson Foundations for Offshore Wind: Design Guidelines. (February).

Duncan, J. M. and Buchignani, A. L. (1976). An Engineering Manual for Settlement Studies.

Gerolymos, N., Zafeirakos, A., and Karapiperis, K. (2015). Generalized failure envelope for caisson foundations in cohesive soil: Static and dynamic loading. *Soil Dynamics and Earthquake Engineering*, 78:154–174.

G.Gudehus (1996). A comprehensive constitutive equation for granular materials. *Soils and Foundations*, 36(1):1–12.

Gourvenec, S. and Barnett, S. (2011). Undrained failure envelope for skirted foundations under general loading. *Geotechnique*, 61(3):263–270.

Green, A. E. and Hill, R. (1951). The mathematical theory of plasticity. *The Mathematical Gazette*, 35:208.

Grimstad, G., Andresen, L., and Jostad, H. P. (2012). NGI-ADP : Anisotropic shear strength model for clay ‡. *Wiley Online Library*, 36(January 2011):483–497.

Herle, I. and Gudehus, G. (1999). Determination of parameters of a hypoplastic constitutive model from properties of grain assemblies. *Mechanics of Cohesive-Frictional Materials*, 4(5):461–486.

Herle, I. and Kolymbas, D. (2004). Hypoplasticity for soils with low friction angles. *Computers and Geotechnics*, 31(5):365–373.

Jia, N., Zhang, P., Liu, Y., and Ding, H. (2018). Bearing capacity of composite bucket foundations for offshore wind turbines in silty sand. *Ocean Engineering*, 151(May 2017):1–11.

Kay, S. and Palix, E. (2011). Caisson capacity in clay: VHM resistance envelope - Part 2: VHM envelope equation and design procedures. *Frontiers in Offshore Geotechnics II - Proceedings of the 2nd International Symposium on Frontiers in Offshore Geotechnics*, (December):741–746.

Kim, D.-J., Choo, Y. W., Kim, J.-H., Kim, S., and Kim, D.-S. (2014). Investigation of Monotonic and Cyclic Behavior of Tripod Suction Bucket Foundations for Offshore Wind Towers Using Centrifuge Modeling. *Journal of Geotechnical and Geoenvironmental Engineering*, 140(5):04014008.

Kourkoulis, R. S., Lekkakis, P. C., Gelagoti, F. M., and Kaynia, A. M. (2014). Suction caisson foundations for offshore wind turbines subjected to wave and earthquake loading: Effect of soil-foundation interface. *Geotechnique*, 64(3):171–185.

Ladd, C. and Foott, R. (1978). Stress-Deformation and Strength Characteristics. *Soil mechanics and foundation engineering*, 26(3):18–20.

Mašín, D. (2005). A hypoplastic constitutive model for clays. *International Journal for Numerical and Analytical Methods in Geomechanics*, 29(4):311–336.

Mašín, D. (2011). PLAXIS implementation of hypoplasticity. page 30.

Mašín, D. (2017). PLAXIS implementation of HYPOPLASTICITY including standalone ABAQUS umat subroutines.

Mašín, D. (2019). *Correction to: Modelling of Soil Behaviour with Hypoplasticity*.

Muduli, P. K., Das, M. R., Samui, P., and Kumar Das, S. (2013). Uplift Capacity of Suction Caisson in Clay Using Artificial Intelligence Techniques. *Marine Georesources and Geotechnology*, 31(4):375–390.

Niemunis, A. (2003). Extended hypoplasticity models for soils. *Schriftenreihe des Institutes fur Grundbau und Bodenmechanik der Ruhr-Universitat Bochum*.

Niemunis, A. and Herle, I. (1997). Hypoplastic model for cohesionless soils with elastic strain range. *Mechanics of Cohesive-Frictional Materials*, 2(4):279–299.

Obrzud, R. F. and Truty, A. (2018). The hardening soil model - a practical guidebook. 05:205.

Palix, E., Willems, T., and Kay, S. (2011). Caisson capacity in clay: VHM resistance envelope - Part 1: 3D FEM numerical study. *Frontiers in Offshore Geotechnics II - Proceedings of the 2nd International Symposium on Frontiers in Offshore Geotechnics*, (January):753–758.

Samui, P., Das, S., and Kim, D. (2011). Uplift capacity of suction caisson in clay using multivariate adaptive regression spline. *Ocean Engineering*, 38(17-18):2123–2127.

Schanz, T., Vermeer, P. A., and Bonnier, P. G. (1999). The hardening soil model: Formulation and verification. *Beyond 2000 in computational geotechnics. Ten Years of PLAXIS International. Proceedings of the international symposium, Amsterdam, March 1999.*, pages 281–296.

Smith, I. M., Griffiths, D. V., and Margetts, L. (2015). *Programming the Finite Element Method: Fifth Edition*.

Stapelfeldt, M., Bubel, J., and Grabe, J. (2015). Numerical Investigation of the Installation Process and the Bearing Capacity of Suction Bucket Foundations. *the 34th International Conference on Ocean, Offshore and Arctic Engineering*, 05(July 2018).

Sturm, H. (2017). Design Aspects of Suction Caissons for Offshore Wind Turbine Foundations. *International Conference on Soil Mechanics and Geotechnical Engineering*, 19(1997):45–63.

Surarak, C., Likitlersuang, S., Wanatowski, D., Balasubramaniam, A., Oh, E., and Guan, H. (2012). Stiffness and strength parameters for hardening soil model of soft and stiff Bangkok clays. *Soils and Foundations*, 52(4):682–697.

Taiebat, H. A. and Carter, J. P. (2000). Numerical studies of the bearing capacity of shallow foundations on cohesive soil subjected to combined loading. *Geotechnique*, 50(4):409–418.

Taiebat, H. A. and Carter, J. P. (2005). A failure surface for caisson foundations in undrained soils. *Frontiers in Offshore Geotechnics, ISFOG 2005 - Proceedings of the 1st International Symposium on Frontiers in Offshore Geotechnics*, (July 2014):289–295.

Tjelta, T. I. (2015). The suction foundation technology. *Frontiers in Offshore Geotechnics III - Proceedings of the 3rd International Symposium on Frontiers in Offshore Geotechnics, ISFOG 2015*, 6(March):85–93.

Tschuchnigg, F., Schweiger, H. F., Sloan, S. W., Lyamin, A. V., and Raissakis, I. (2015). Comparison of finite-element limit analysis and strength reduction techniques. *Geotechnique*, 65(4):249–257.

Ukritchon, B. and Boonyatee, T. (2015). Soil parameter optimization of the NGI-ADP constitutive model for Bangkok soft clay. *Geotechnical Engineering*, 46(1):28–36.

von Wolffersdorff, P. A. (1996). A hypoplastic relation for granular materials with a predefined limit state surface. *Mechanics of Cohesive-Frictional Materials*, 1(3):251–271.

Vulpe, C. (2015). Design method for the undrained capacity of skirted circular foundations under combined loading: Effect of deformable soil plug. *Geotechnique*, 65(8):669–683.

Yilmaz, S. and Tasan, H. (2019). Numerical investigations on the behaviour of offshore suction bucket foundations under cyclic axial loading. *Geotechnical Engineering foundation of the future*, 1(2014).

Yin, Z. Y., Teng, J. C., Li, Z., and Zheng, Y. Y. (2020). Modelling of suction bucket foundation in clay: From finite element analyses to macro-elements. *Ocean Engineering*, 210(September 2019):107577.

Zdravkovic, L., Potts, D. M., and Jardine, R. J. (2001). A parametric study of the pull-out capacity of bucket foundations in soft clay. *Geotechnique*, 51(1):55–67.

Zhang, P., Li, Y., Lv, Y., DIng, H., and Le, C. (2019). Bearing capacity characteristics of composite bucket foundation under torque loading. *Energies*, 12(13).

Zorzi, G., Mankar, A., Velarde, J., Sørensen, J., Arnold, P., and Kirsch, F. (2019). Reliability analysis of offshore wind turbine foundations under lateral cyclic loading. *Wind Energy Science Discussions*, (September):1–25.

# A

# Soil report

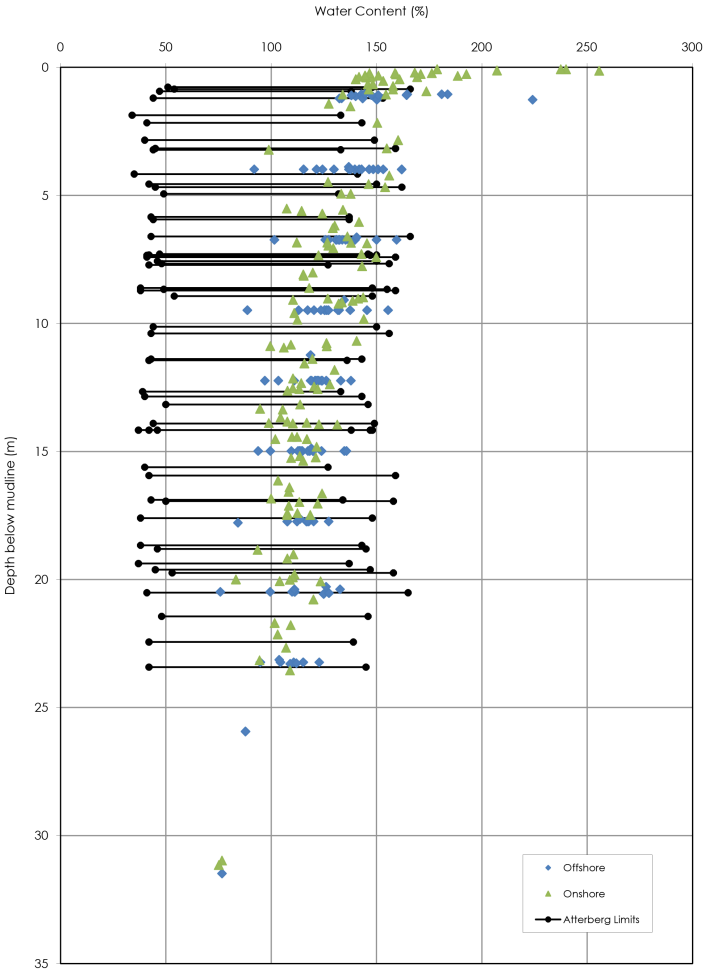


Figure A.1: Water Content and Atterberg Limits Profile vs. Depth

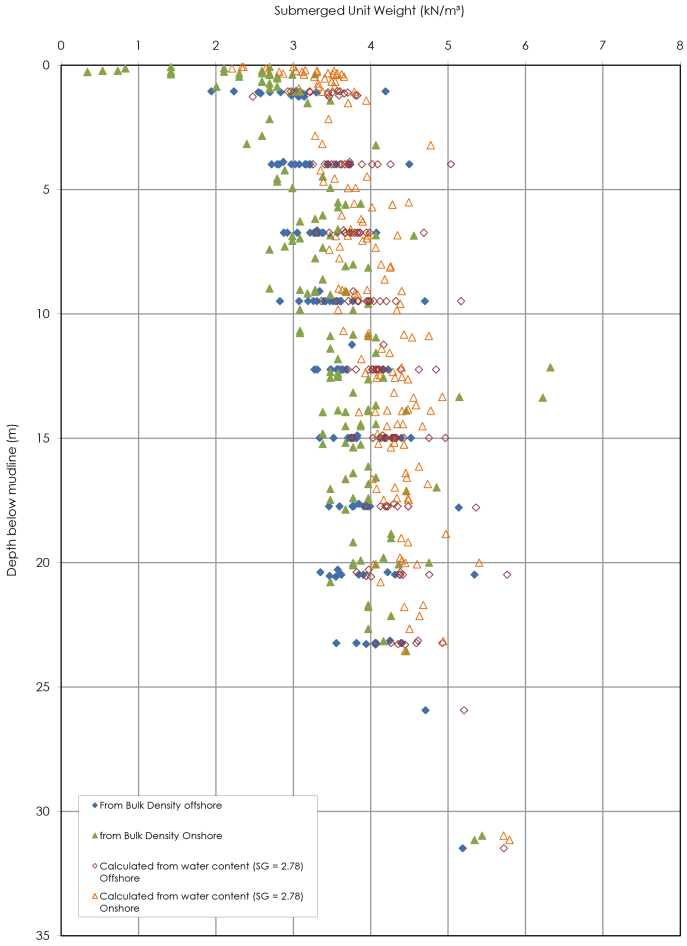


Figure A.2: Submerged Unit Weight vs. Depth

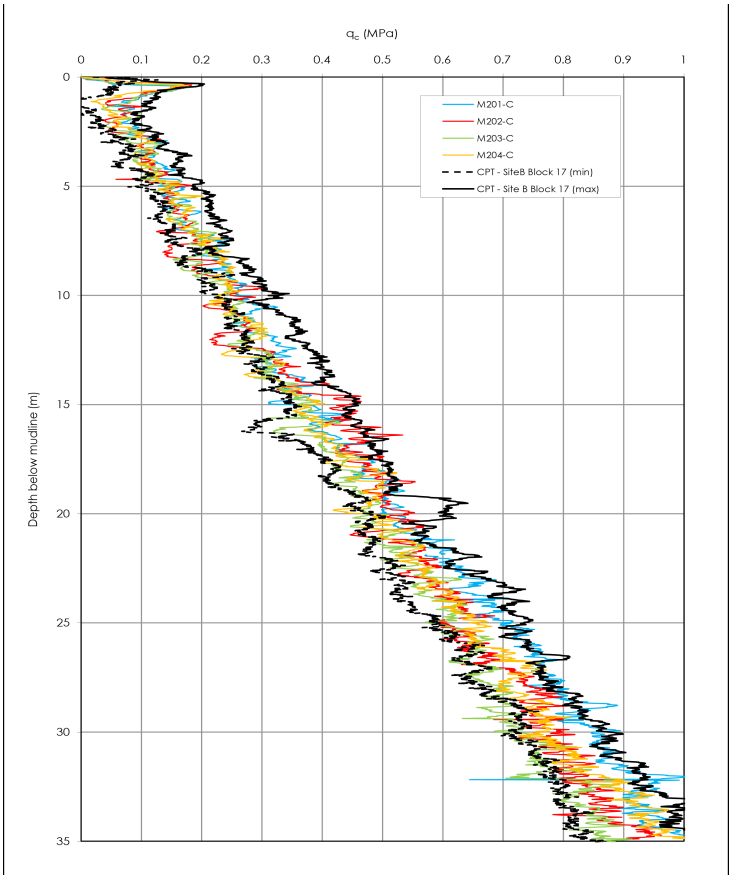


Figure A.3: qc vs. Depth Western Manifolds

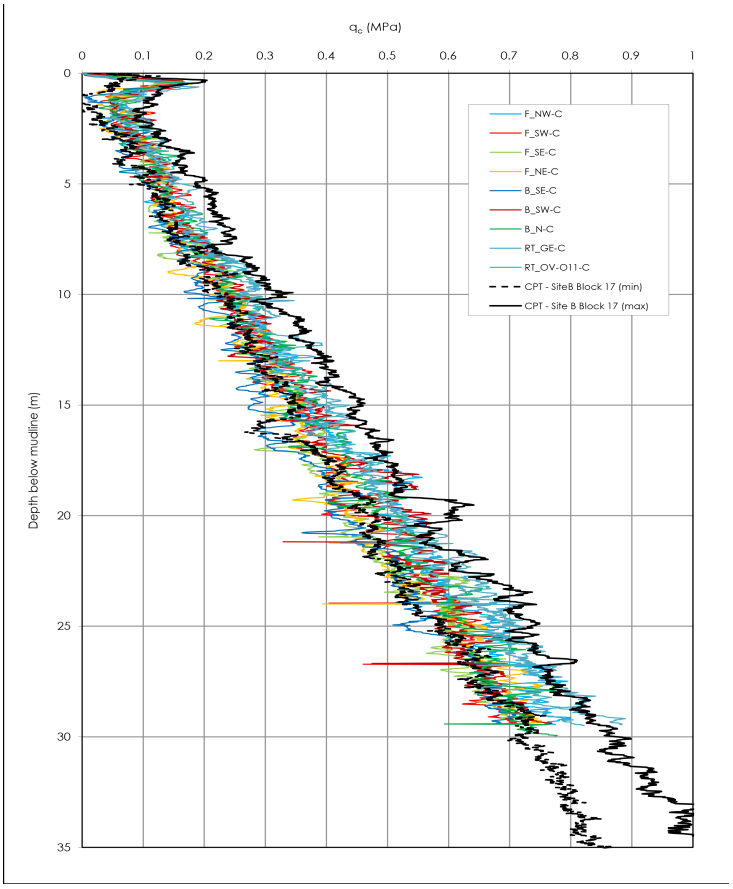


Figure A.4: qc vs. Depth FPSO/Buoys/Riser Towers

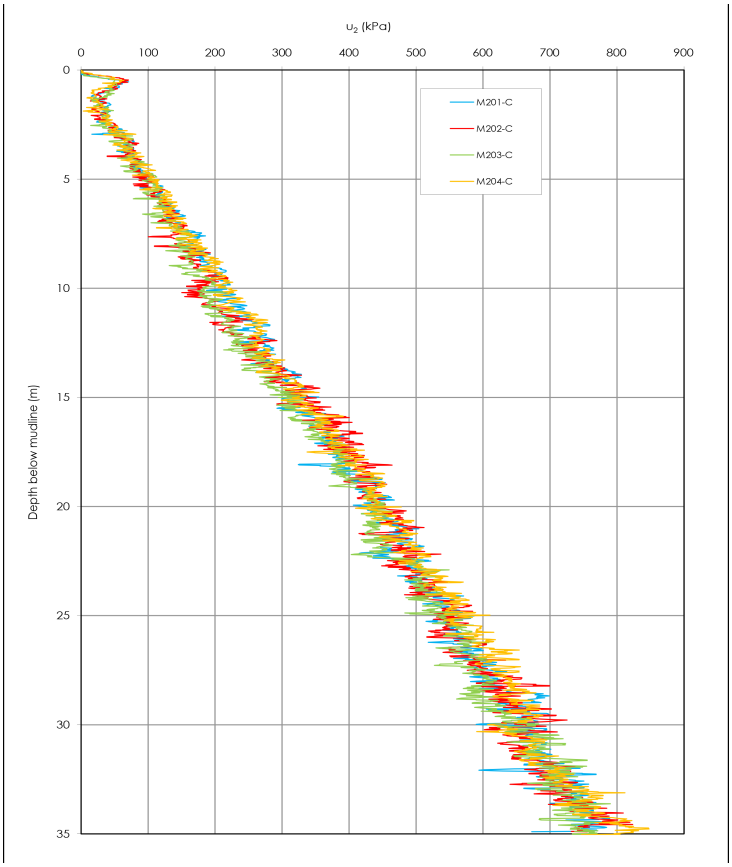


Figure A.5: Excess pore pressure vs. Depth Western Manifolds

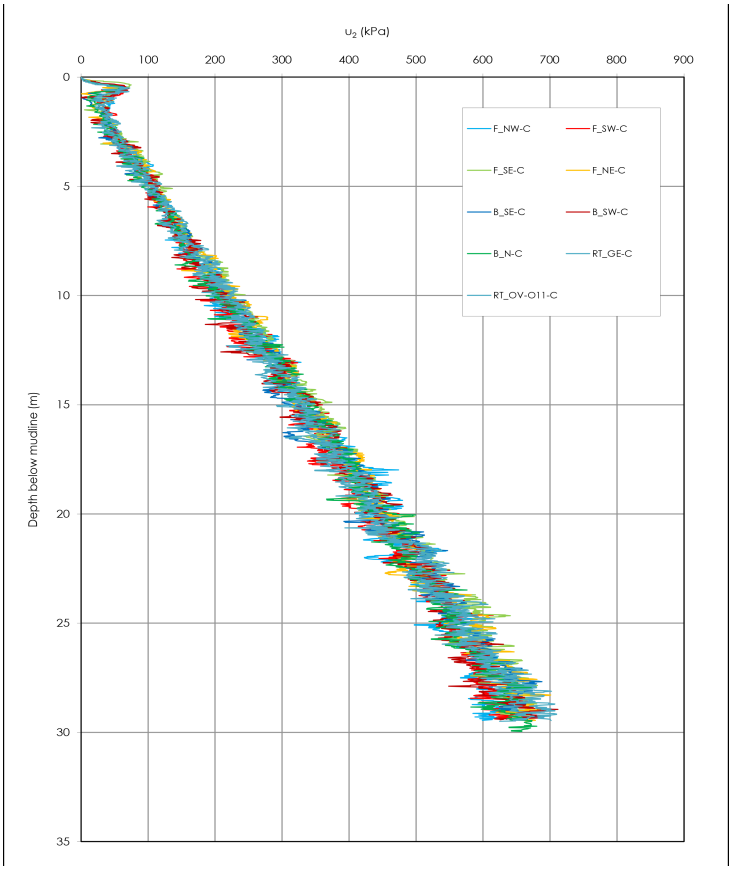


Figure A.6: Excess pore pressure vs. Depth FPSO/Buoys/Riser Towers

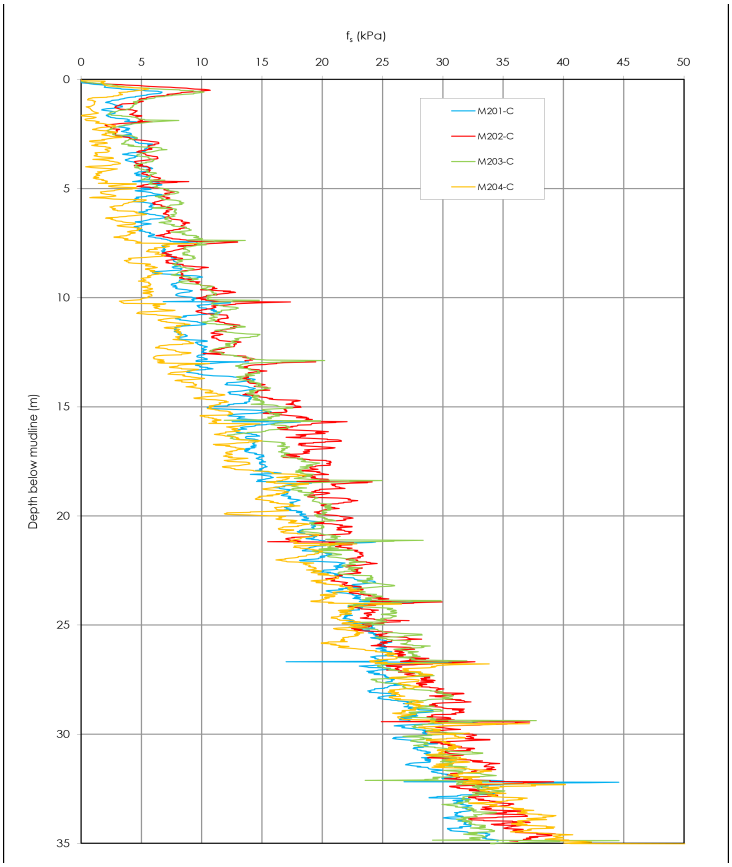


Figure A.7: CPT sleeve friction vs. Depth Western Manifolds

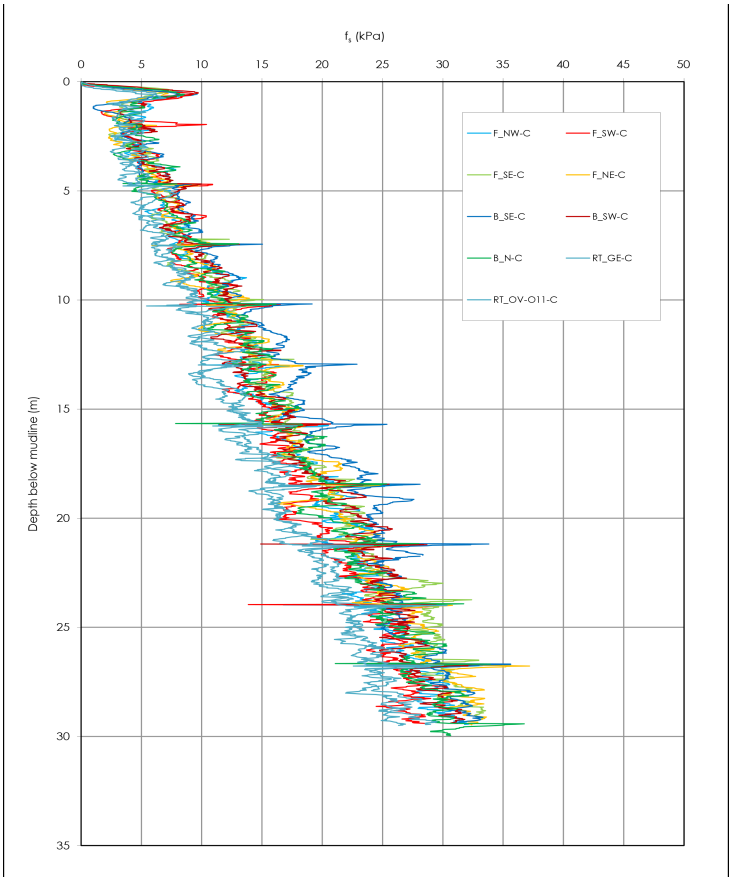


Figure A.8: CPT sleeve friction vs. Depth FPSO/Buoys/Riser Towers

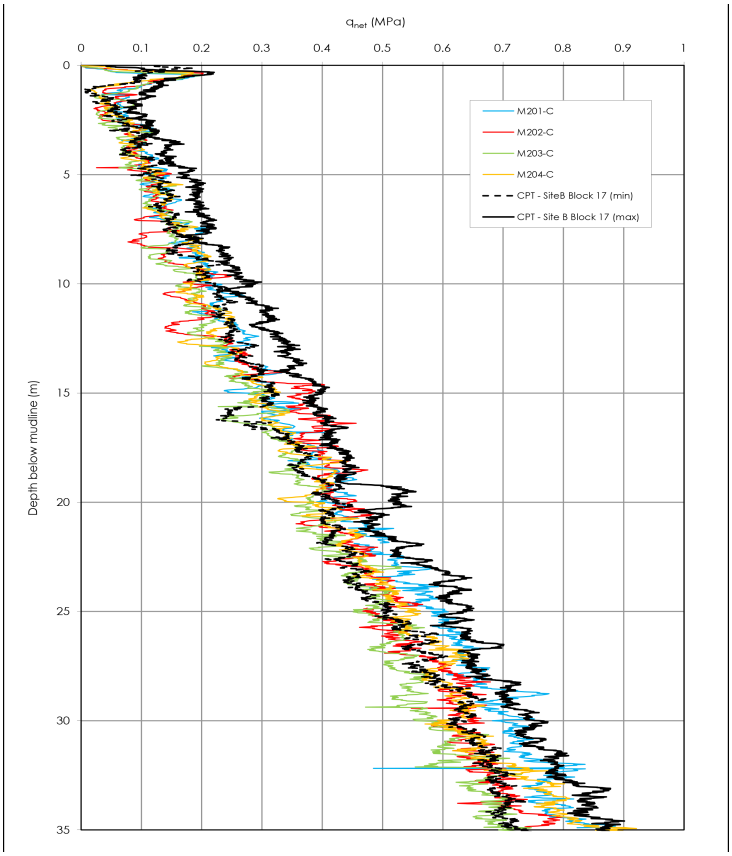


Figure A.9: $q_{net}$ vs. Depth Western Manifolds

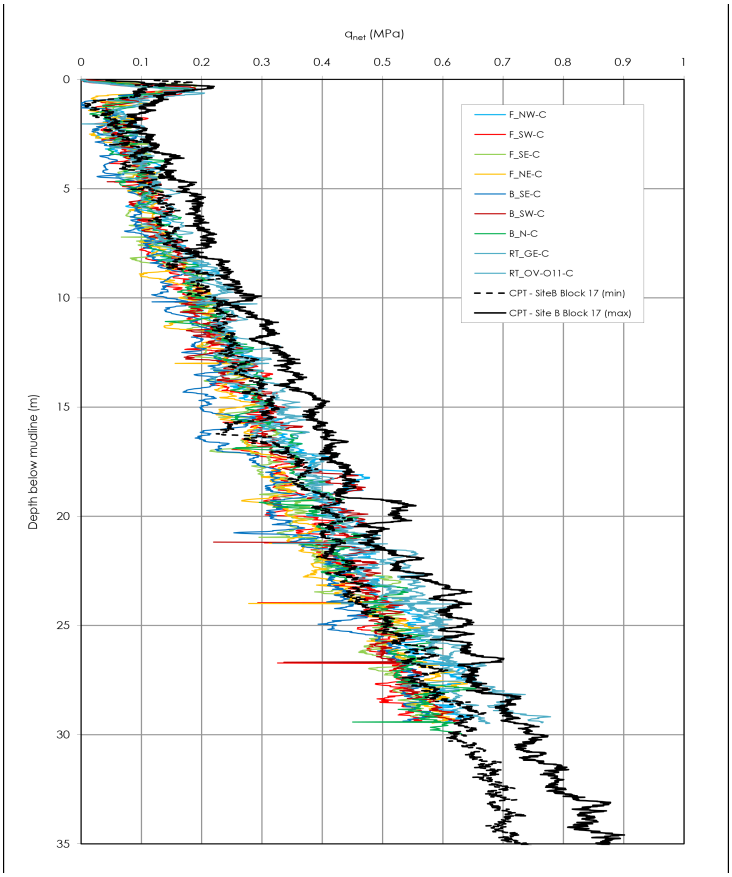


Figure A.10: $q_{net}$ vs. Depth FPSO/Buoys/Riser Towers

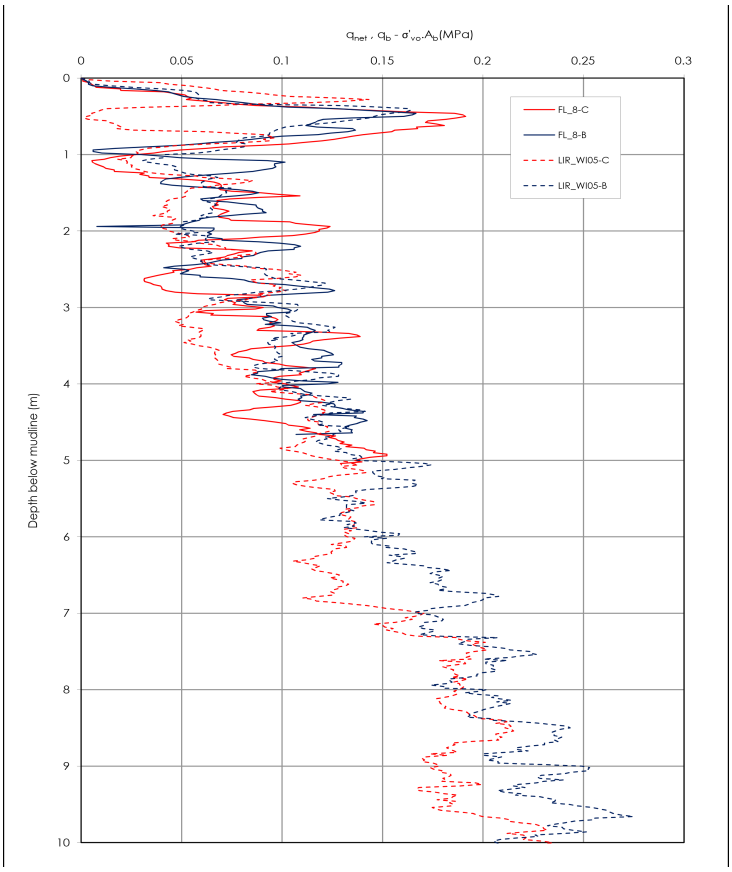


Figure A.11: Comparison of net cone resistance and corrected ball resistance vs. Depth Western Area

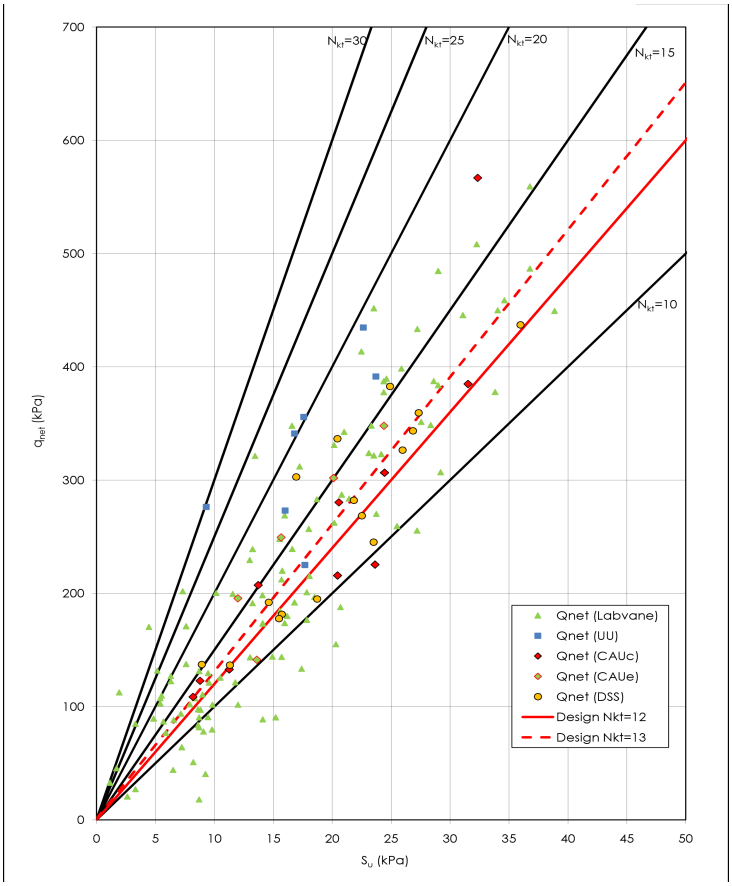


Figure A.12: $q_{net}$ vs. Undrained Shear strength Western Area

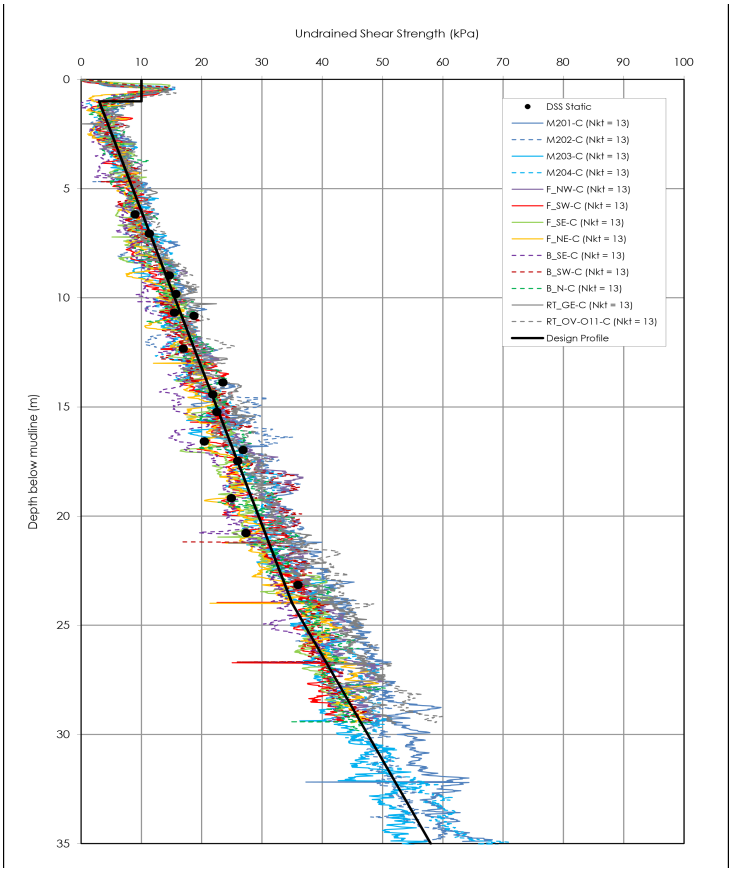


Figure A.13: Undrained Shear Strength (from DSS Tests and CPT) vs. Depth Western Area

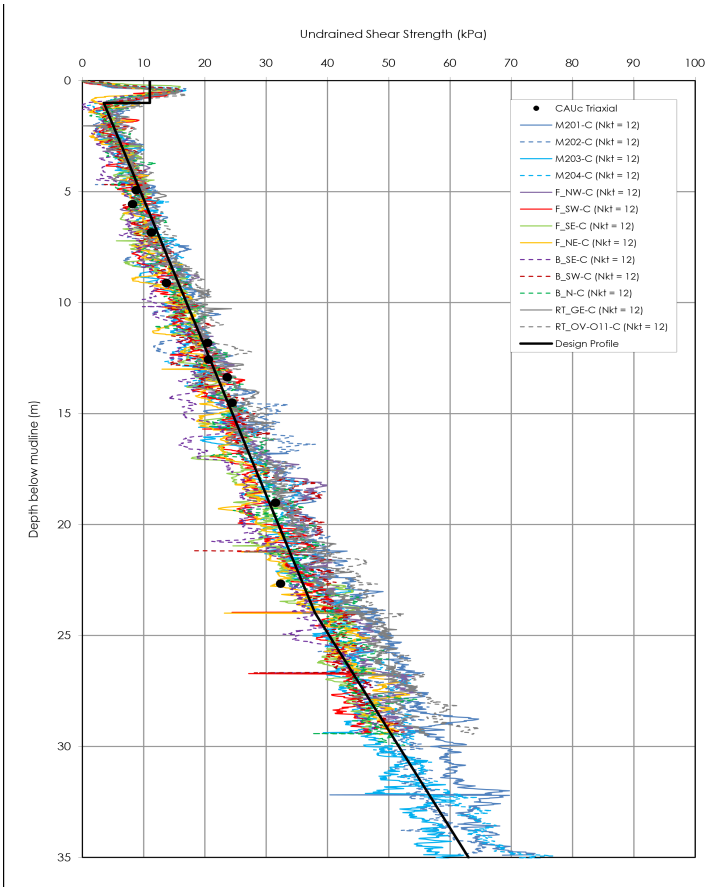


Figure A.14: Undrained Shear Strength (from CAUc Triaxial and CPT) vs. Depth Western Area

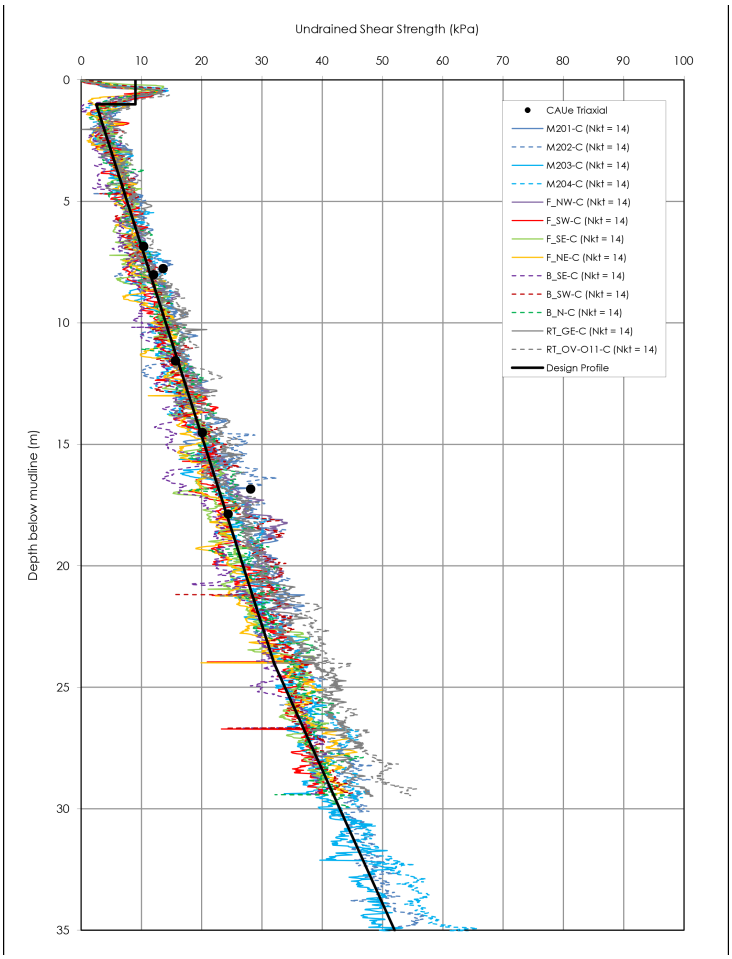


Figure A.15: Undrained Shear Strength (from CAUe Triaxial and CPT) vs. Depth Western Area

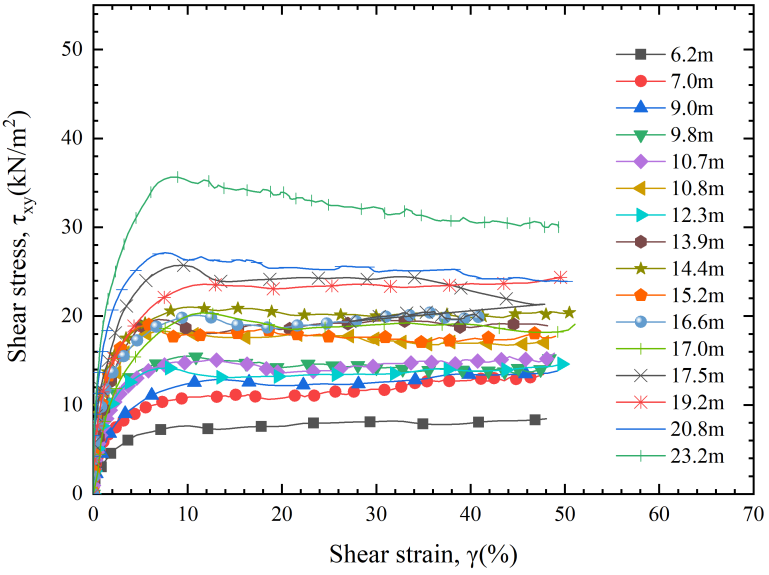


Figure A.16: Shear stress v.s. shear strain result of simple shear tests

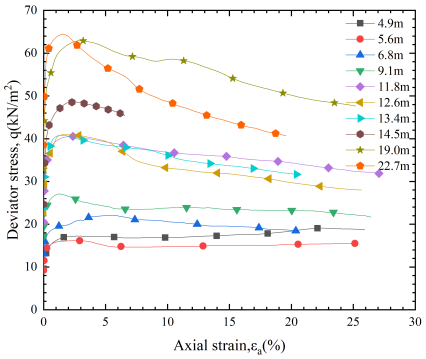


(a) Deviator stress versus axial strain

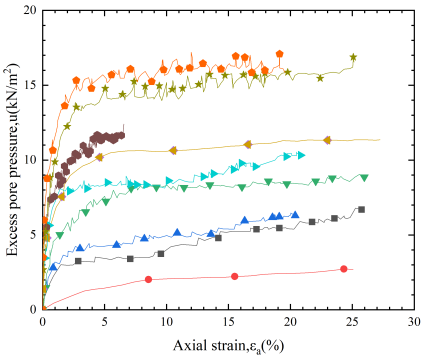


(b) Excess pore pressure versus axial strain

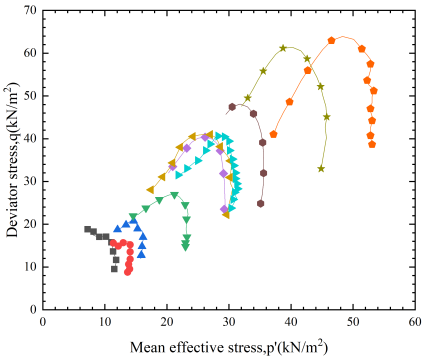


(c) Stress paths $q$ versus $p'$

Figure A.17: CAUc test results for Site A

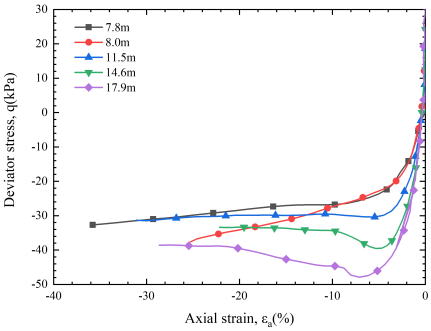


(a) Deviator stress versus axial strain

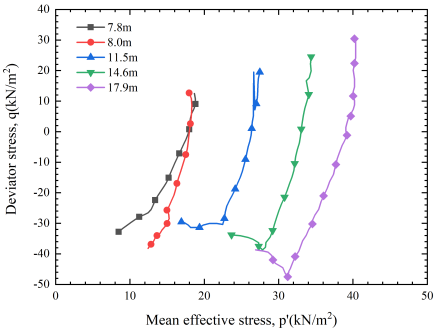


(b) Stress paths $q$ versus $p'$

Figure A.18: CAUe test results for Site A

# B

# Deformation analysis

In the output program of PLAXIS 3D, the Relative shear stress $\tau_{rel}$ was calculated as the following equation B.1. This value gives an indication of the proximity of the stress point to the failure envelope. The $\tau_{max}$ is the maximum value of shear stress, which was calculated base on the strength parameters and stress state (Brinkgreve R.B.J. (2018)). The hypoplastic model is a user-defined model in PLAXIS 3D, so the maximum shear stress was available in the output program, neither the relative shear stress. The results of relative shear stress for different constitutive models and cases were plotted in Figure B.1 to B.4.

$$\tau_{rel} = \frac{\tau_{mob}}{\tau_{\max}} \tag{B.1}$$

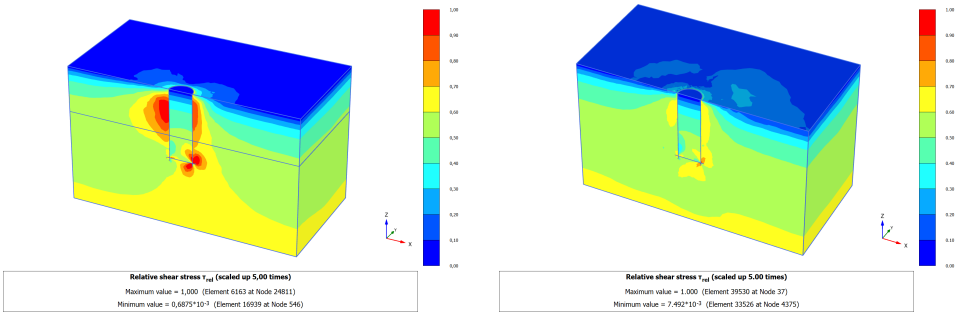


(a) Mohr-Coulomb Model (b) Hardening soil model

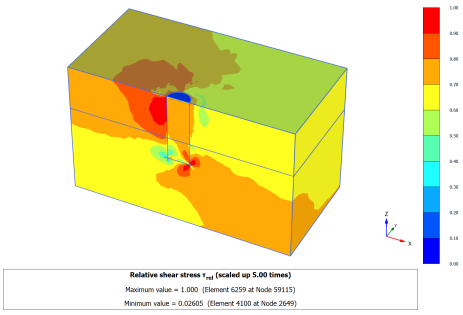


(c) NGI-ADP model

Figure B.1: Relative shear stress for horizontal load case

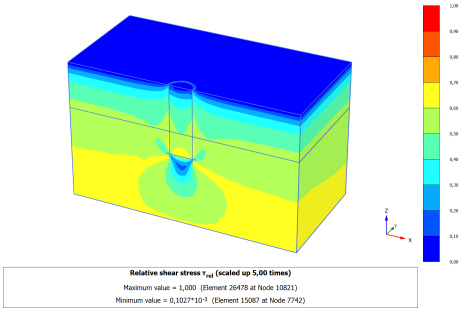


(a) Mohr-Coulomb Model

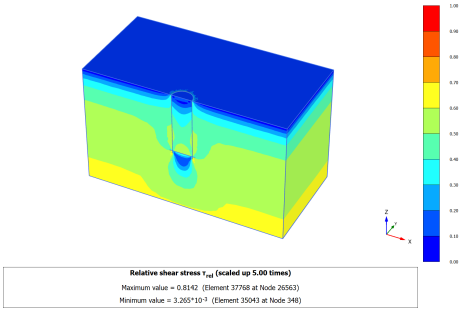


(b) Hardening soil model

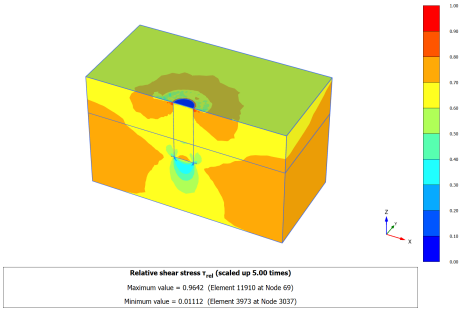


(c) NGI-ADP model

Figure B.2: Relative shear stress for vertical tension load case

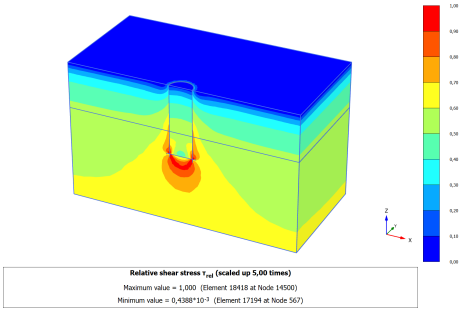


(a) Mohr-Coulomb Model

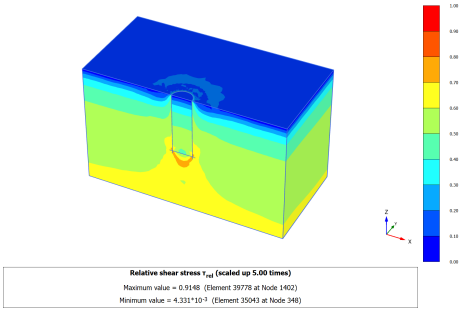


(b) Hardening soil model

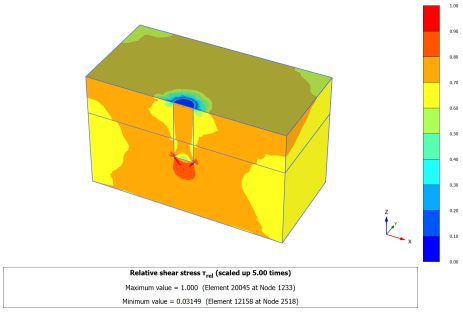


(c) NGI-ADP model

Figure B.3: Relative shear stress for vertical compression load case

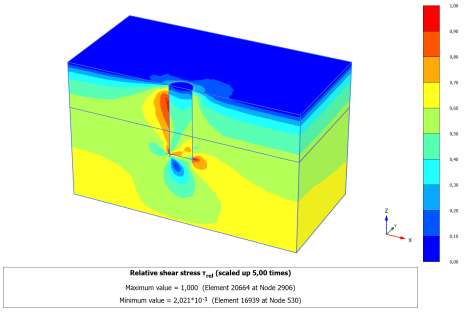


(a) Mohr-Coulomb Model

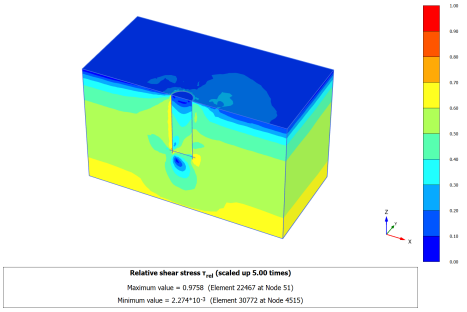


(b) Hardening soil model

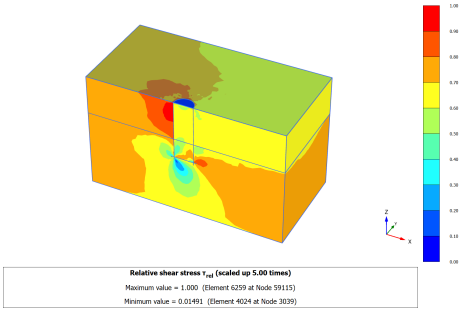


(c) NGI-ADP model

Figure B.4: Relative shear stress for VHM-combining load case

# C

# Capacity analysis

In the output program, the maximum shear stress was calculated for the whole soil domain. The strength reduction method was applied in safety analysis phase to obtain the factor of safety(Equation 5.2 and 5.3). Here the maximum shear stress was plotted for VHM loading phase and safety analysis phase ($\sum M_{sf} = 2.34$).

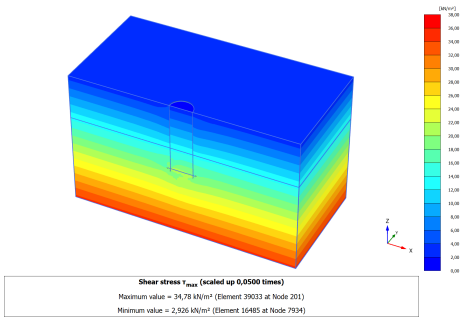


(a) Mohr-Coulomb Model

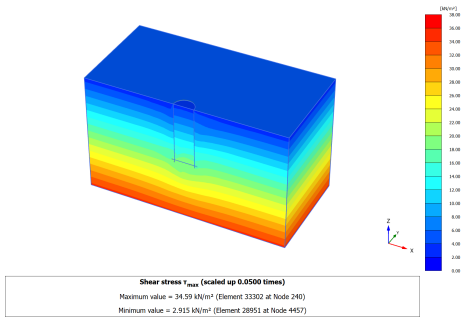


(b) Hardening soil model

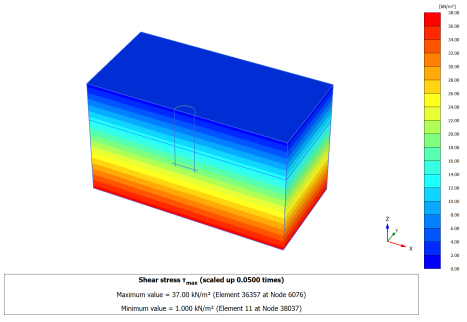


(c) NGI-ADP model

Figure C.1: Maximum shear stress for loading phase

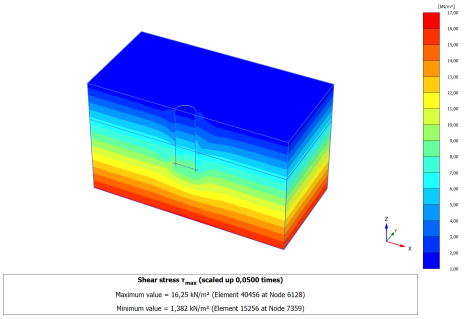


(a) Mohr-Coulomb Model

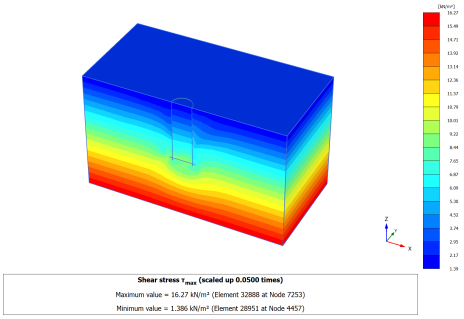


(b) Hardening soil model

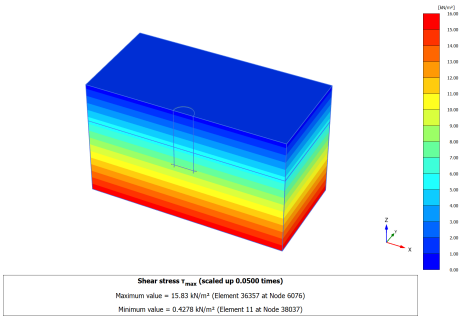


(c) NGI-ADP model

Figure C.2: Maximum shear stress for safety analysis phase ($\sum M_{sf} = 2.34$)